Exploring Structural and Optical Properties of TMDC Heterostructures Using Atomic Force Microscopy Ironing

Swaroop Kumar Palai

RÉPUBLIQUE FRANÇAISE
Liberté Égalité Fraternité

Université de Toulouse

Doctorat de l'Université de Toulouse

préparé à l'Université Toulouse III - Paul Sabatier

Étude des propriétés structurelles et optiques des hétérostructures de TMDC en utilisant le 'ironing' par microscopie à force atomique.

Thèse présentée et soutenue, le 8 octobre 2024 par

SWAROOP KUMAR PALAI

École doctorale
SDM - SCIENCES DE LA MATIERE - Toulouse

Spécialité
Physique de la Matière

Unité de recherche
LNCMI - Laboratoire National des Champs Magnétiques Intenses

Thèse dirigée par
Paulina PLOCHOCKA

Composition du jury
M. Marco FELICI, Rapporteur, Sapienza University of Rome
M. Robert KUDRAWIEC, Rapporteur, Wrocaw University of Science and Technology
M. Adnen MLAYAH, Examinateur, Université Paul Sabatier
Mme Paulina PLOCHOCKA, Directrice de thèse, CNRS

THÈSE

En vue de l'obtention du

DOCTORAT DE L'UNIVERSITÉ DE TOULOUSE

délivré par Université Paul Sabatier Toulouse III
Spécialité : Physique de la Matière

Présentée et soutenue par
Swaroop kumar PALAI

Exploring Structural and Optical Properties of TMDC Heterostructures Using Atomic Force Microscopy Ironing

---

Ecole doctorale : Science de la Matière
Unité de recherche : Laboratoire National des Champs Magnétiques Intenses
Directeurs de Thèse : Paulina PLOCHOCKA

Exploring Structural and Optical Properties of TMDC Heterostructures Using Atomic Force Microscopy Ironing.

Abstract: Recent progress in the study of two-dimensional (2D) materials, particularly transition metal dichalcogenides (TMDCs), has unveiled remarkable properties and potential applications. TMDCs, such as MoS_2 and $MoSe_2$, are noted for their unique electronic and optical characteristics, which can be finely tuned by mechanical exfoliation and precise stacking into heterostructures. Experimental and theoretical analyses have demonstrated that these indirect gap materials when exfoliated into their monolayer form, acquire a direct gap at the K point of the Brillouin zone. In this thesis, we discuss the development and optimisation of a novel fabrication technique using nail polish, which includes the processes of exfoliation, characterisation and assembly into heterostructures of TMDCs encapsulated by hexagonal boron nitride (hBN) using a nail polish stamp.

A major part of this research is dedicated to the post-fabrication technique known as atomic force microscopy (AFM) ironing. In Chapter 3, we explore the application of this method to improve the flatness and uniformity of TMDC monolayers and their heterostructures. The AFM ironing process effectively reduces surface roughness and mitigates interlayer inhomogeneity, thereby improving the optical properties of the materials. In our study, we investigate the excitonic physics in these 2D materials, employing steady-state photoluminescence (PL) spectroscopy. The results demonstrate that AFM ironing not only enhances the structural quality of the heterostructures but also significantly influences the excitonic transitions, linewidth and intensities, leading to improved photoluminescence characteristics.

In Chapter 4, the thesis introduces the development and utilization of a flake probe for magneto-transmission measurements. This novel experimental setup, synchronized with resistive coils and cryostat systems, enables the precise study of the electronic properties of the TMDC heterostructures under varying magnetic fields. These measurements provide critical insights into optical behaviour of 2D materials by doing a proof of concept on 2D phenethylammonium lead iodide (PEPI).

Through a combination of experimental techniques, including AFM characterization and optical spectroscopy, this research provides comprehensive insights into the fundamental properties and potential applications of TMDC heterostructures. The findings contribute to the broader understanding of 2D materials and pave the way for their use in advanced nanoelectronic and optoelectronic devices.

Keywords: Transition Metal diChalcogenides, Heterostructures, Interlayer Exciton, Atomic Force Microscopy, AFM Ironing, Optical Characterisation.

Étude des Propriétés Structurales et Optiques des Hétérostructures TMDC en Utilisant le 'Ironing' par Microscopie à Force Atomique.

Résumé: Les progrès récents dans l'étude des matériaux bidimensionnels (2D), en particulier les dichalcogénures de métaux de transition (TMDCs), ont révélé des propriétés remarquables et des applications potentielles. Les TMDCs, tels que le MoS_2 et le $MoSe_2$, sont connus pour leurs caractéristiques électroniques et optiques uniques, qui peuvent être finement ajustées par exfoliation mécanique et empilement précis en hétérostructures. Des analyses expérimentales et théoriques ont démontré que ces matériaux à gap indirect acquièrent un gap direct au point K de la zone de Brillouin lorsqu'ils sont exfoliés en leur forme de monocouche. Dans cette thèse, nous discutons du développement et de l'optimisation d'une technique de fabrication novatrice utilisant du vernis à ongles, comprenant les processus d'exfoliation, de caractérisation et d'assemblage en hétérostructures de TMDCs encapsulés par du nitrure de bore hexagonal (hBN) en utilisant un tampon de vernis à ongles.

Une grande partie de cette recherche est dédiée à la technique post-fabrication connue sous le nom de 'ironing' par microscopie à force atomique (AFM). Dans le Chapitre 3, nous explorons l'application de cette méthode pour améliorer l'état de surface et l'uniformité des monocouches de TMDC et de leurs hétérostructures. Le processus de AFM ironing réduit efficacement la rugosité de la surface et atténue l'hétérogénéité inter-couche, améliorant ainsi les propriétés optiques des matériaux. Dans notre étude, nous investiguons la physique des excitons dans ces matériaux 2D, en utilisant la spectroscopie de photoluminescence (PL) en régime stationnaire. Les résultats démontrent que le AFM ironing non seulement améliore la qualité structurelle des hétérostructures mais influence également de manière significative les transitions excitoniques, la largeur des raies et les intensités, conduisant à des caractéristiques de photoluminescence améliorées.

Dans le chapitre 4, cette thèse présente le développement et l'utilisation d'une sonde de magnéto- transmission dédiée à l'étude des flocons. Cet appareil expérimental novateur, synchronisé avec une bobine résistive et un système cryogénique, permet l'étude précise des propriétés électroniques des hétérostructures TMDC sous différents champs magnétiques. Ces mesures fournissent des informations cruciales sur le comportement optique des matériaux 2D en réalisant une preuve de concept sur le plomb iodure de phénéthylammonium 2D (PEPI).

Grâce à une combinaison de techniques expérimentales, incluant la caractérisation AFM et la spectroscopie optique, cette étude offre des aperçus complets sur les propriétés fondamentales et les applications potentielles des hétérostructures TMDC. Les résultats permettent une meilleure compréhension des matériaux 2D et ouvrent la voie à leur utilisation dans des dispositifs nanoélectroniques et optoélectroniques avancés.

Mots-clés: Dichalcogénures de Métaux de Transition, Hétérostructures, Microscopie à Force Atomique, Repassage AFM, Caractérisation Optique.

Acknowledgements

First of all, I would like to express my gratitude to my supervisor prof. Paulina Plochocka, for giving me this opportunity to conduct my research, for her guidance and patience during my PhD research. The scientific atmosphere under her guidance has helped me throughout my research. I would also like to thank the members of the jury prof. Marco Felici (Sapienza University of Rome), prof. Robert Kudrawiec (Wrocaw University of Science and Technology) and prof. Adnen Mlayah(CNRS-LAAS) for their valuable comments on this research.

I would like to thank my amazing team members Mateusz Dyksik, Alessandro Surrente, Michal Baranowski, Duncan Maude, Nikodem Sokolowski, Jakub Jasinski, Andrzej Nowok, Katarzyna Posmyk, Paulina Peksa, Katarzyna Zalewska, Maciej Smiertka, Agata Zielinska and Ewelina Cybula who have been there throughout this journey helped me a lot with experiments, data analysis and paper writing. I would also like to acknowledge all my amiable collaborators, Andres Castellanos-Gomez, Carmen Munuera, Sergio Puebla, Thomas Pucher, Estrella Sanchez Viso, Alina Schubert, Felix Carrascoso, Onur Cakiroglu and Alvaro Rodriguez (2D Foundry, Spain), Francessco Gucci, Armando Genco and prof. Stefano dal Conte (Polimi, Italy), Pavel Kamarov and Veronika Hegrová (Nenovision s.r.o, Czech Republic) for their excellent experimental work and enjoyable discussion. I would like to extend my gratitude to the Doctoral School especially prof. Joël Douin, for their support and guidance throughout my PhD journey. I would also like to thank my colleagues especially Tristan Thebault in the Laboratoire National des Champs Magnétiques Intenses (LNCMI-Toulouse), who were always very kind and helpful. Thanks to Cécile Laroche, Catherine Chabot, Severine Bories and Catherine Stasiulis for being extremely kind and helping me deal with French administrative work time and again. A special thanks to Nicolas Bruyant, Sylvie George, Marc Nardone, Abdelaziz Zitouni, Noé Estorges for their kind help with the probe, synchronization system and cryostat. I would also like to acknowledge, the director and deputy director of the LNCMI, Charles Simon and Florence Lecouturier.

My acknowledgements are extended to my parents and my girlfriend Apurva Das, who have always supported me in my pursuits. I would also like to thank my friends in Toulouse, Arpan Khandelwal, Haasanthi Madala, Heer Vadaliya and Parameswari Ganeshan for the nice moments we had together outside of the lab.

A huge thanks to Marie Skłodowska-Curie for awarding a 36 months scholarship, which allowed me to carry out my research in France and other countries as a PhD student.

Swaroop kumar Palai
Toulouse, June 2024.

Contents

Chapter 1

Introduction

Contents

1.1 Introduction

Following the great success of graphene[Geim 2007, Novoselov 2012], there has been a remarkable development in the field of two-dimensional (2D) materials. To date, approximately 150 such materials have been explored, and this family continues to expand. One of the unique properties of these materials is that their individual layers are weakly bonded together by van der Waals interactions, enabling them to be mechanically cleaved into single monolayers[Novoselov 2005]. Based on their chemical compositions and structural configurations, these materials can be classified as metallic like borophene (2D boron sheets), semi-metallic like silicene (2D silicon sheets), germanene (2D germanium sheets), semiconducting like the transition metal dichalcogenides (TMDCs) or insulating like hexagonal boron nitride (hBN). Another striking property of these materials is that their property can be modulated based on the number of layers[Duong 2017]. Interlayer coupling and quantum confinement effects, arising from varying the number of layers, can be used to tune the band gap and the optical and electrical characteristics of these materials. For example, black phosphorous maintains a direct band gap but this gap shifts from the mid-infrared spectrum in bulk form[Keyes 1953, Asahina 1983] to visible range for few layers[Castellanos-Gomez 2014, Tran 2014].

TMDCs have emerged as an exciting class of materials, extensively investigated for their unique electrical and optical properties. They hold promise for new physical phenomena and a wide range of applications, including

nanoelectronics[Wang 2012, Liu 2017], nanoscale sensing[Wang 2021, Ko 2016], and nanophotonics[Krasnok 2018, Xia 2014]. These materials have been known to show an indirect band gap in the near-infrared range when in bulk [Coehoorn 1987] but exhibit a direct gap in the visible range at the **K+** and **K-** points in Brillouin zone when thinned down to a monolayer [Mak 2010, Splendiani 2010].

TMDCs in general are represented by the formula MX_2, where M denotes a metal and X denotes a chalcogenide atom (such as the **Se** or **S**). The choice of the transition metal M, spans over group IV (e.g., Ti, Zr, Hf), group V (e.g., V, Nb, Ta), group VI (e.g., Mo, W), group VII (e.g., Tc), to group X (e.g., Ni). Our focus in this thesis will be specifically on the group VI TMDCs, which includes molybdenum disulfide (MoS_2), molybdenum diselenide ($MoSe_2$), molybdenum ditelluride ($MoTe_2$), tungsten disulfide (WS_2) and tungsten diselenide (WSe_2). The atoms in each layer are bonded through strong covalent bonds, whereas the layers themselves are held together by weaker van der Waals (vdW) forces. This weaker interlayer bonding facilitates the easy cleavage of the crystals into single monolayers of atomic thickness. In the following sections, we will discuss the atomic structure of TMDCs, followed by their electronic band structure and how it gradually changes with the thickness of the layers. We will also discuss the excitonic physics in both the monolayers and heterostructures of TMDCs. Towards the end of the chapter, we will focus on the formation of moiré structures originating from the stacking of two different materials and discuss the electronic hybridisation of the bands.

1.2 Crystal structure and physical properties

TMDCs have been the subject of extensive research over the past few decades. The structural properties of these materials were initially characterized by Linus Pauling in 1923 [Dickinson 1923]. A TMDC (MX_2) monolayer[1] contains three atomic planes, X-M-X, where the entire X-M-X trilayer has a typical thickness of 6-7 Å, with the transition metal covalently bonded to six chalcogen atoms. The hexagonally packed metal layer is sandwiched between two layers of chalcogen atoms. As shown in Figure 1.1(a), the layer of Mo atoms (in black) is sandwiched between the two layers of S atoms (in yellow). The interlayer distance between two individual monolayers has been determined by high-resolution transmission electron microscope (HR-TEM) to be around 6-6.5 Å for MoS_2 [Bui 2022].

TMDCs are usually found in three polymorphic forms, namely $1T$, $2H$, and $3R$. These polymorphs are represented in Figure 1.1(b). Numbers in the prefix represent the number of layers of TMDC in each unit cell, while the letters reflect the type of symmetry: T for trigonal, H for hexagonal, and R for rhombohedral. Of the three, $2H$ and $1T$ are the most commonly occurring phases[Manzeli 2017]. For example, natural MoS_2 occurs in $2H$ (also known as trigonal prismatic) phase, but it has also been found in $1T$ (also called octahedral) phase for layers usually exfoliated using intercalation[Coehoorn 1987] and these two phases are the energetically favourable

[1] Hereafter, a 'monolayer' would signify the X-M-X trilayer.

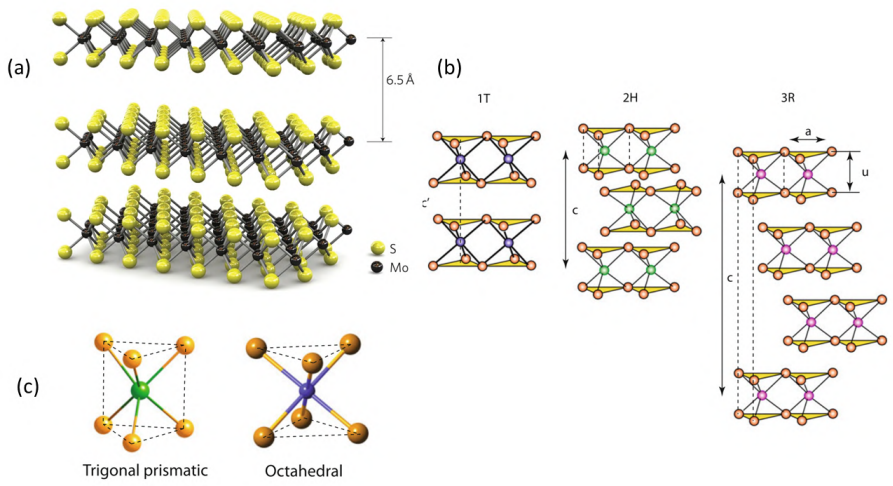

Figure 1.1: (a) A three-dimensional representation of a typical layered MoS_2 structure is shown with the metal and chalcogenide atoms represented by the black and yellow spheres respectively. Reproduced from [Radisavljevic 2011] with permission from Springer Nature. (b) The local coordination can be either trigonal prismatic or octahedral. (c) Schematics of the structural polytypes of TMDC. From left to right: 1T (tetragonal symmetry, one layer per repeat, octahedral metal coordination), 2H (hexagonal symmetry, two layers per repeat, trigonal prismatic coordination), and 3R (rhombohedral symmetry, three layers per unit cell, trigonal prismatic coordination). Reproduced from [Kolobov 2016] with permission from Springer Nature.

phases. The trigonal prismatic and octahedral arrangements are presented in Figure 1.1(c). In an octahedral arrangement, the central metal atom M is surrounded by six chalcogen atoms, located at the vertices of the octahedron. The angles between the bonds are 90 degrees whereas, in trigonal prismatic arrangement, the central metal atom is surrounded by six chalcogen atoms with bond angles other than 90 degrees and forming two parallel triangles.

In the $2H$ configuration, the two chalcogen atom planes are aligned directly above one another, whereas they are staggered in the $1T$ configuration. The group VI TMDCs belong to the $P6_3/mmc$ (D^4_{6h} in Schoenflies notation(no. 194)) crystallographic group. Upon reduction from the three-dimensional bulk to monolayer (ML) form, they maintain the trigonal prismatic coordination. The symmetry is reduced to the $P6/mmm$ (D^1_{3h}(no. 187))[Kuc 2015]. In this thesis, we investigate the heterostructures made from $MoSe_2$ and MoS_2 monolayers in their $2H$ form.

1.2.1 Reciprocal lattice and Brillouin zone of MX_2 compounds

After discussing the crystal lattice structure of the MX_2 compounds, it is imperative to discuss the reciprocal lattice, which provides an insight into the electronic properties and symmetry considerations of the material. The reciprocal lattice vectors are constructed from the direct lattice vectors and serve as a construct for

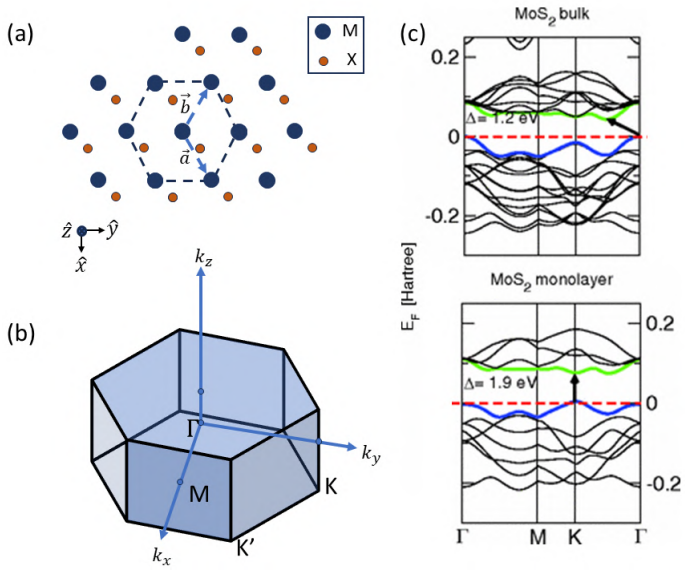

Figure 1.2: (a) In-plane lattice vectors are shown in blue arrows. Blue spheres indicate the transition metal (M) atoms and the orange spheres denote the chalcogen (X) atoms. (b) Illustration for the Brillouin zone with the symmetry points for 2H-MX_2 compounds. (c) Band structure calculations show the indirect transitions at the Γ point (in bulk) and direct transitions originating at the K-K point (in ML). Reprinted figure with permission from [Kuc 2011], Copyright (2024) by the American Physical Society.

the understanding of the evolution of electronic band structures. The Brillouin zone is defined as the Weigner Seitz cell of the reciprocal lattice and represents the fundamental region in reciprocal space.

Figure 1.2(a) illustrates the crystal lattice of the $2H$ polytype MX_2 monolayer. The lattice vectors in the direct lattice are represented as follows:

$$\vec{a} = \frac{a\sqrt{3}}{2}\hat{x} + \frac{a}{2}\hat{y}$$
$$\vec{b} = -\frac{a\sqrt{3}}{2}\hat{x} + \frac{a}{2}\hat{y}$$
$$\vec{c} = c \cdot \hat{z}$$

where a is the in-plane lattice constant defining the periodicity in the x and y directions, and c is the out-of-plane lattice constant defining the periodicity along the z-axis. Once, we established the direct lattices, the reciprocal lattice vectors are given by:

$$\mathbf{a}^* = \frac{4\pi}{a\sqrt{3}}\left(\frac{1}{2}\hat{\imath} + \frac{\sqrt{3}}{2}\hat{\jmath}\right)$$
$$\mathbf{b}^* = \frac{4\pi}{a\sqrt{3}}\left(-\frac{1}{2}\hat{\imath} + \frac{\sqrt{3}}{2}\hat{\jmath}\right)$$
$$\mathbf{c}^* = \frac{2\pi}{c}\hat{k}$$

In Figure 1.2 (b), we present the Brillouin zone which has a hexagonal symmetry. We show the centre of the Brillouin zone is known as Gamma ($\mathbf{\Gamma}$) point, where the electronic states contribute to indirect transitions in bulk crystals, as presented in the top panel of the Figure 1.2(c). The edge where two rectangular faces join is known as the **K** point, where the electronic states are involved in direct transitions in monolayers, shown in the bottom panel of Figure 1.2(c). In the next section, we will discuss the evolution of the band structure in TMDCs.

1.3 Optical properties and evolution of band structure

In this section, we will explore the fundamental aspects of the band structure of the TMDCs in $2H$ phases. When transitioning from bulk forms to monolayer (ML), the crystal symmetry is reduced, leading to significant alterations in their electronic structures. TMDC films with an even number of layers, including bulk and bilayers (BLs), maintain inversion symmetry, with the inversion center situated between the layers. In contrast, this symmetry is broken in systems with an odd number of layers, such as ML. The breaking of inversion symmetry profoundly impacts the macroscopic optical and electronic properties of TMDCs. The hexagonal lattice structure leads to the formation of valleys at the K and K' points in the Brillouin zone, which possess equal energies but different momenta. These points form two sets of three equivalent locations at the corners of the hexagonal Brillouin zone, creating valley-selective electron populations as a consequence of inversion symmetry breaking. Despite being energetically degenerate and governed by time-reversal symmetry, the K and K' valleys can be selectively manipulated for applications in valleytronics and modern nanoelectronics.

Time-reversal symmetry, which relates the K and K' valleys, ensures that for every state at momentum $\mathbf{k}$ with spin-up, there is a corresponding state at momentum $-\mathbf{k}$ with spin-down. This symmetry dictates that the K and K' valleys must exhibit opposite spin splitting, a feature crucial for understanding and leveraging spin and valley physics in TMDCs.

In both theoretical and experimental studies, MoS_2 is often treated as the prototypical material for this class of materials as indicated by Bromley *et.al.* who suggested significant similarity in the electronic structures across the family[Bromley 1972]. Furthermore, Coehoorn *et.al.* reported that the theoretical

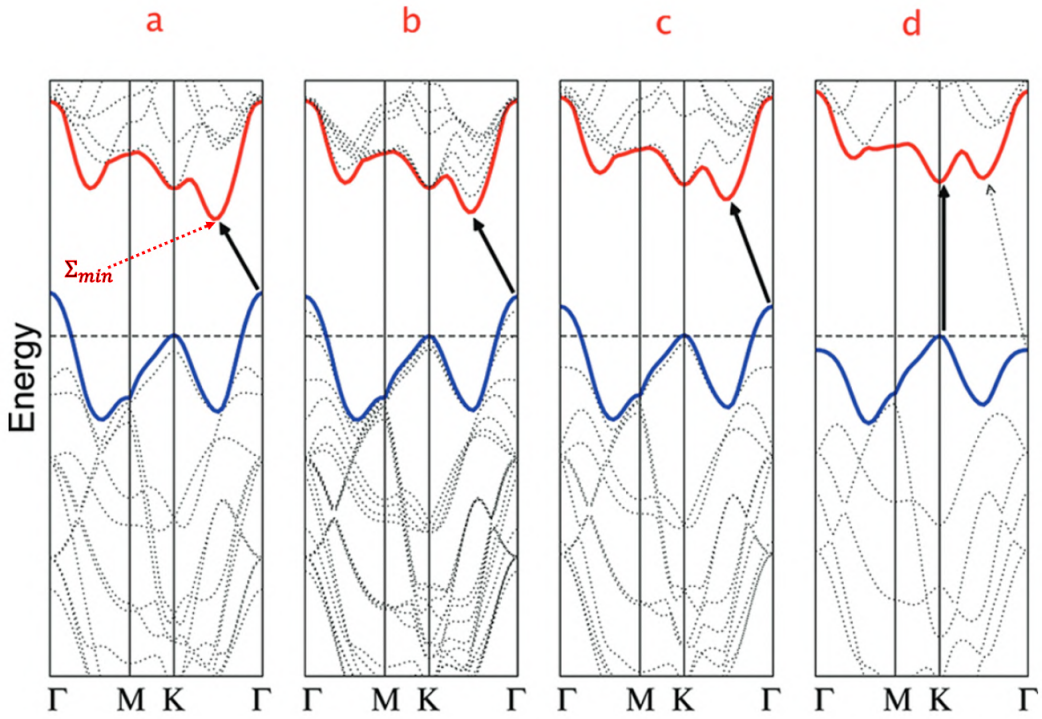

Figure 1.3: Band structures calculated for (a) bulk MoS_2, (b) quadrilayer MoS_2, (c) bilayer MoS_2 and (d) monolayer MoS_2. The solid arrows indicate the lowest energy transitions. Reprinted with permission from [Splendiani 2010], Copyright © 2010, American Chemical Society .

and experimental band structures of MoS_2, $MoSe_2$ and WSe_2 are in good agreement and display notable similarities to each other[Coehoorn 1987]. Another interesting property of these materials that we briefly touched upon in Section 1.1, is the transition from indirect to direct band gap when thinning down from bulk to monolayer[Mak 2010, Splendiani 2010]. Mak *et.al.* in 2010 reported the bulk indirect band gap for MoS_2 to be around 1.29 eV and when thinned down to monolayers, the direct band gap was found to be 1.90 eV.

Splendiani *et.al.* conducted DFT calculations to predict the electronic structure of bulk and few-layers MoS_2 of varying thicknesses[Splendiani 2010]. These calculations presented in Figure 1.3, reveal that the conduction band minima (CBM) for bulk and few layers occur in between **K** and **Γ** points(also referred to as $\mathbf{\Sigma_{min}}$ in [Cheiwchanchamnangij 2012]) of the Brillouin zone and the VBM occurs at the **Γ** point. The calculations revealed that the direct band gap at **K** is immune to the change in the thickness of the layer. In contrast, the indirect bandgap increases monotonically as the layer numbers decrease.

One of the most important outcomes of these band structure calculations is that they reveal the contribution of orbitals of different atoms which form the electronic states. In MoS_2, the electronic states participating in the indirect transition at the **Γ**

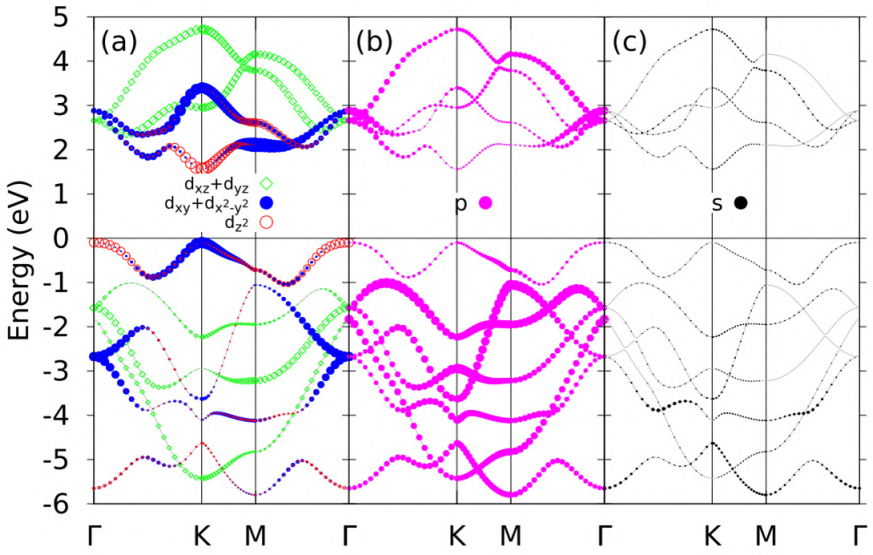

Figure 1.4: First principle(FP) calculations showing the orbital projections for monolayer MoS_2. The size of the symbol corresponds to the population in the corresponding state. (a) shows the contribution from the d-orbitals of Mo atom, blue dots for d_{xy} and $d_{x^2-y^2}$, red circles denote d_{z^2}, green open diamonds denote d_{xz} and d_{yz} (b) pink circles denote the p orbitals dominated by the S atoms (c) Black circles denote the total s orbitals. Reprinted with permission from [Liu 2013], by the American Physical Society .

point of CBM and $\mathbf{\Sigma_{min}}$ of VBM emerge from the super-position of d orbitals of Mo atom and antibonding p_z orbitals of S atom[Splendiani 2010]. A three-band tight binding(TB) model on MoS_2 (shown in Figure 1.4) revealed that the contribution of s and p orbitals is negligible and the Bloch states near the band edges are mostly the combination of d_{z^2}, d_{xy} and $d_{x^2-y^2}$ orbitals[Liu 2013] [2]. Band structure calculations supported by Angle-resolved photoemission spectroscopy (ARPES) measurements of $MoSe_2$ reveal a similar story. The hybridization of Mo $4d$ and Se $4p$ orbitals gives rise to the valence and conduction bands[Mahatha 2012]. The valence band and conduction bands of $MoSe_2$ are about 6 eV and 4 eV respectively. ARPES revealed that $MoSe_2$ has an indirect band gap of 1.10 eV and a direct gap of 1.48 eV in the monolayer limit [Mahatha 2012]. At the highest symmetry point in the Brillouin zone (Γ), the top of the valence band is dominated by a combination of Mo $4d_{z^2}$ and Se $4p_z$ orbitals[Fuhr 1999].

Because of the inversion symmetry breaking, spin-orbit coupling (SOC), which originates from the d orbitals of the heavy metal atoms, causes the valence band to split thus distinguishing spin up and down orientations in ML TMDCs[Zhu 2011, Kuc 2015]. Both these effects, inversion symmetry breaking along with strong SOC

[2] In their approximation, the $X-p$ orbitals—specifically, the p orbitals from the chalcogen atoms—were omitted from the basis set.

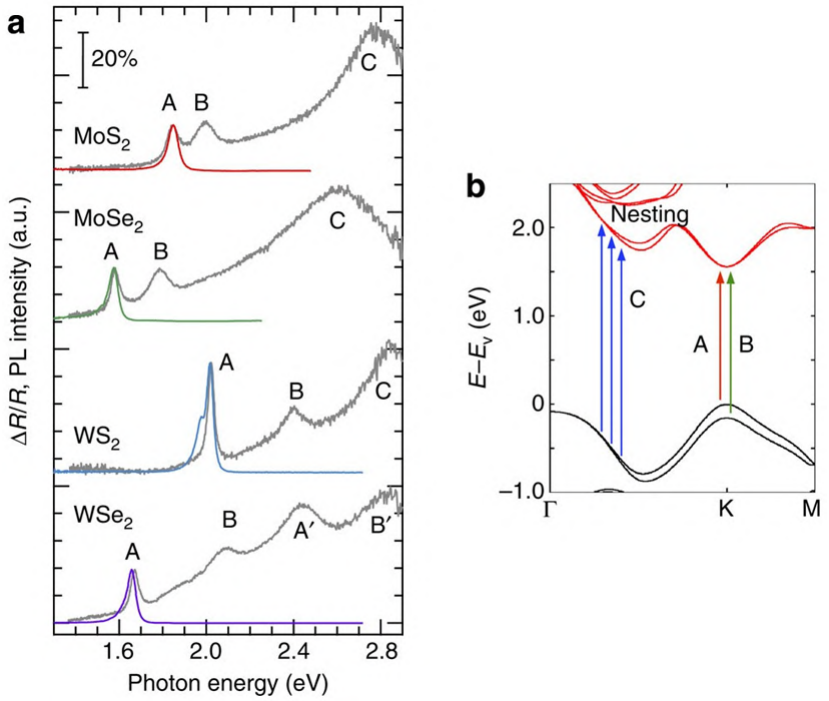

Figure 1.5: (a)PL spectra (depicted in red, green, blue, and purple) and differential reflectance spectra (shown in grey) of monolayer MX_2 flakes on quartz substrates. (b) The band structure of monolayer MoS_2 was calculated using DFT, with arrows indicating the transitions of excitons A and B. Reproduced from [Kozawa 2014]. Copyright (2024) Springer Nature.

lead to a phenomenon known as spin-valley locking[Xiao 2012]. The spin-valley locking at the valence band edge prevents the relaxation of spin and valley pseudospins, as the flip of spin or valley index alone is forbidden by the valley contrast spin splitting.

In the absorption spectra of monolayer TMDCs, an additional excitonic transition (exciton B) is observed at higher energies alongside the lowest excitonic transition (exciton A). This higher-energy transition originates from the SOC splitting of the valence band. In Figure 1.5(a), the spectra feature the A, B and C excitons on individual TMDCs. The energetic separation between the A and B excitonic transitions corresponds well with the SOC-induced splitting value in the valence band. At even higher energies, another transition (exciton C) is observed, which is associated with band nesting, as presented in Figure 1.5(b). Band-nesting regions in molybdenum and tungsten disulfide and diselenide monolayers are located midway between the Γ and Λ points[Carvalho 2013].

The VBM splitting reported in MoS_2 and $MoSe_2$ is 146 meV and 210 meV respectively[Cheiwchanchamnangij 2012, Coehoorn 1987]. The CBM at K undergoes splitting because of the SOC, although the splitting is much smaller than the

VB, of the order of 4 meV. The SOC-induced splitting in the VBM is summarised in Table 1.1 below.

	Δ_{SOC}(meV)
MoS_2	146
$MoSe_2$	183
WS_2	425
WSe_2	461

Table 1.1: Spin-orbit coupling (SOC) splitting for TMDCs based on Perdew Burke Ernzerhof(PBE) exchange functional. Adapted from [Ramasubramaniam 2012].

1.4 Excitonic Physics

The optical response of monolayer dichalcogenides is primarily influenced by excitonic effects. When a photon is absorbed, an electron transitions from the valence band to the conduction band, creating a vacancy or "hole" in the valence band. The positively charged holes (h^+) are bound to the negatively charged electrons (e^-) through Coulombic forces, forming a hydrogen-like quasiparticle called an exciton (X). There are two primary types of excitons: Frenkel and Wannier-Mott excitons. Frenkel excitons are tightly bound e^- and h^+ pairs that are typically found in the materials with high exciton binding energy and the envelope is spread to just a few unit cells as shown in Figure 1.6(a). Meanwhile, Wannier-Mott excitons are loosely bound e^- and h^+ pairs found in materials with low exciton binding energies and are spread over several hundred Angstroms, shown in Figure 1.6(b). This section explores the properties and prevalence of Wannier-Mott excitons in these materials. Initially, we will utilize the hydrogenic model to derive the energy eigenstates of excitons in bulk semiconductors, providing a theoretical framework for understanding their behaviour in semiconductors. We will extend our discussion of excitons in these systems by employing a 2D hydrogen model. Subsequently, the discussion will focus on intralayer and interlayer excitons (IX) within TMDC heterostructures.

1.4.1 Theoretical formalism and effective mass framework

blueThe e^- and h^+ are bound particles but with comparable masses and the Coulombic interaction between the e^- and h^+ is screened by the crystal medium's dielectric constant ϵ [Pelant 2012]. The excitons in semiconductors form a hydrogen-like series of energy states. The interaction between the e^- and h^+ leads to a hydrogen-like Coulombic potential:

$$U(r) = -\frac{e^2}{4\pi\varepsilon|r_e - r_h|} \tag{1.1}$$

Here, $|r_e - r_h|$ represents the separation between the electron and the hole. This is a two-body problem and the Schrödinger equations can be written as

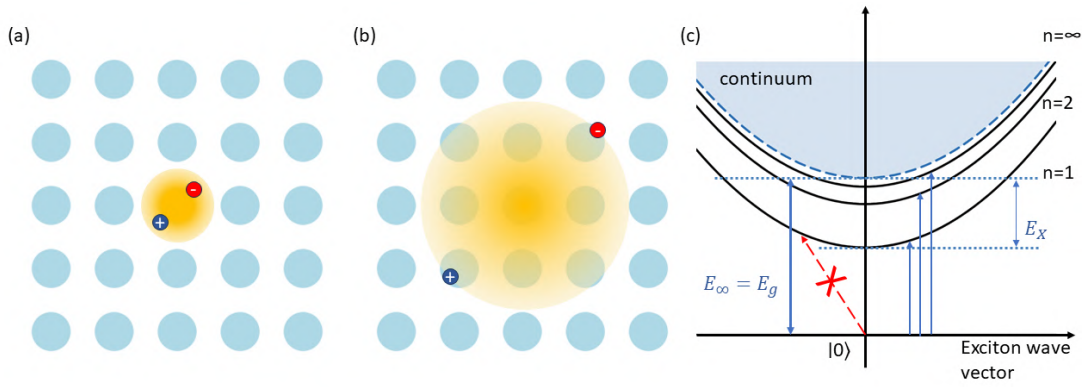

Figure 1.6: Illustration of a (a) Frenkel exciton. (b) Wannier-Mott exciton. (c) Schematic representation of the energy states of an exciton, where n=∞ corresponds to the free-particle bandgap energy.

follows[Singh 2007]:

$$\left(-\frac{\hbar^2}{2m_e^*}\nabla^2 - \frac{\hbar^2}{2m_h^*}\nabla^2 - -\frac{e^2}{4\pi\varepsilon|r_e - r_h|}\right)\psi_{ex} = E\psi_{ex} \tag{1.2}$$

where m_e^* (m_h^*) is the effective mass of the electron (hole).

The problem can be reduced from a standard two-body problem to a one-body problem by considering the following form of the Hamiltonian, which has two parts. The first part describes the motion of the center of the $e^- - h^+$ system and the other part describes the relative motion of the system.

$$H = \underbrace{\frac{\hbar^2 K^2}{2M}}_{\text{Center of mass term}} + \underbrace{\left(\frac{\hbar^2 k^2}{2\mu} - \frac{e^2}{4\pi\epsilon|r|}\right)}_{\text{Relative motion term}} \tag{1.3}$$

where,

- $\mathbf{K} = \mathbf{k}_e - \mathbf{k}_h$ wave vector of the exciton,
- $\mathbf{r} = \mathbf{r}_e - \mathbf{r}_h$
- $\mu = \frac{m_e^* m_h^*}{m_e^* + m_h^*}$ reduced exciton mass, (m_e^* and m_h^* are the effective masses of e^- and h^+ respectively.) and,
- $M = m_e^* + m_h^*$ translational mass.

The solution to the second part of the Hamiltonian in equation 1.3 is what gives rise to discrete energy states and can be solved as the usual hydrogen atom problem. This finally leads us to the energy eigenvalues in a bulk semiconductor:

$$E_n^{3D} = -\frac{\mu e^4}{2(4\pi\epsilon)^2\hbar^2}\frac{1}{n^2} = -\frac{\mu}{m_0}\frac{R_y}{\epsilon^2 n^2} = -\frac{R_y^*}{n^2} \tag{1.4}$$

where,

- $n = 1, 2, 3 \ldots$ principal quantum number,
- $R_y^* = 13.6 \text{ eV} \frac{\mu}{m_0} \frac{1}{\varepsilon^2}$ exciton Rydberg energy, (m_0 is the rest mass e^-)

The dielectric constant ϵ profoundly impacts the properties of the excitons in the semiconductor. It substantially decreases the Coulombic attraction between an electron and a hole. This attenuation in Coulombic force is particularly significant, given that the effective masses of these charge carriers are markedly reduced in comparison to the mass of a free electron. The direct consequence of this decrease in effective masses is the decrease in the R_y^* and increase in Bohr radius as:

$$r_n = \frac{\varepsilon}{\mu/m_0} a_{B_n} = \frac{\varepsilon}{\mu/m_0} n^2 a_B, \tag{1.5}$$

where a_B is the Bohr radius of the hydrogen atom corresponding to the ground state($|0\rangle$). Due to the small effective masses of the carriers and the high dielectric constant of the crystal, the exciton radii in bulk semiconductors are generally larger than in a hydrogen atom. For instance, in GaN the radius is approximately 2.8 nm, and in CdTe, it is around 10 nm[Fox 2010].

The absorption characteristics of Wannier-mott excitons are illustrated in Figure 1.6(c). The absorption process involves transitions from the ground state ($|0\rangle$) to higher energy excitonic states ($n = 1$ and beyond, such as $n = 2, 3, \ldots$). These transitions typically result in a series of excitonic absorption lines at specific energies, which are given by:

$$h\nu = E_g - \frac{E_B}{n^2}$$

Here, E_g is the bandgap energy, and E_B represents the exciton binding energy.

In bulk semiconductors, the exciton binding energy is relatively small compared to the thermal energy at room temperature (approximately 25 meV at 300 K). As a result, excitons can generally only be observed at very low temperatures.

The formalism of reduced effective mass for excitons treated like hydrogen atoms simplifies the two-body problem into a one-body problem by using the reduced effective mass μ. This allows for the application of well-known solutions from the hydrogen atom problem to calculate the energy levels, binding energy, and Bohr radius of excitons in semiconductors. This formalism is crucial for understanding the optical properties of excitons in materials and their behaviour under various conditions.

1.4.2 Excitons in 2D confinement: 2D hydrogen atom model.

In systems characterised by two-dimensional spatial confinement, excitons exhibit increased binding energies, which arise due to the stronger spatial overlap of the e^- and h^+ wavefunctions. Zaslow *et.al.* in 1967 presented the eigen energies of such confined systems to be[Zaslow 1967]:

$$E_n^{2D} = E_B^{3D} \cdot \frac{1}{\left(n - \frac{1}{2}\right)^2} \tag{1.6}$$

As we discussed in the previous Section 1.4.1, with the thinning down of the material to monolayer, there is a significant drop in the dielectric screening, which leads to a considerable increase in the exciton binding energy. As shown in Equation 1.6, the exciton binding energy in the ground state (for $n = 1$) of a 2D semiconductor is four times greater than that in a 3D counterpart, i.e. $E_1^{2D} = 4E_B^{3D}$. In atomically thin 2D systems, the exciton wave function extends beyond the material, encountering a different dielectric environment, as illustrated in Figure 1.7(a). In two-dimensional TMDCs, dielectric screening is weak because the electric field that binds the e^- and h^+ extends outside the material. This weak screening leads to enhanced Coulomb interactions[Chernikov 2014]. The increased Coulomb interaction is a critical factor contributing to the substantial enhancement of exciton binding energy observed within these 2D materials. Typically, such binding energies in 2D materials are considerably higher than those in their bulk counterparts due to the combined influences of reduced dimensionality and reduced dielectric screening effects. For example, Zhu *et al.* reported a binding energy of 0.71 eV for monolayer WS_2[Zhu 2014]. Binding energies of other materials in the family are summarised in the Table 1.2:

Material	**Binding Energy (eV)**	**Authors et al.**
Monolayer WS_2	0.71	Zhu et al. ([Zhu 2014])
Multilayered 2H-$MoTe_2$	0.30	Jung et al. ([Jung 2021])
Monolayer MoS_2	0.24	Park et al. ([Park 2018])
Monolayer WSe_2	0.24	Park et al. ([Park 2018])
Monolayer $MoSe_2$	Variable	Gupta et al. ([Gupta 2017])

Table 1.2: Exciton Binding Energies in Transition Metal Dichalcogenides (TMDCs).

The binding energies of the excitons are significantly larger than k_BT even at room temperature($T = 300$ K). For this reason, the excitonic effects dominate even at room temperature.

The binding energies calculated using equation 1.6, based on the hydrogen model are suited for representing exciton energies in an ideal 2D system. However, experimental evidence, as demonstrated by Chernikov *et al.* indicated a significant deviation from the 2D hydrogen model for monolayer WS_2 as shown in Figure 1.7(b). The plot also illustrates that the disagreement is less prominent for the 2s state but quite substantial for the ground state (1s). Despite this, higher excited states largely conform to the model's predictions [Chernikov 2014]. Additionally, GW-BSE calculations have shown that the states in the same shell but with lower angular momentum have higher energy i.e. $E_{3s} > E_{3p} > E_{3d}$ in WS_2 monolayer[Ye 2014]. This is not true for the hydrogen atom in which the same principal quantum numbers are degenerate.

In order to address these discrepancies, alternate models that incorporate inhomogeneous dielectric screening have been proposed. These include the models by Rytova[Rytova 2018] and Keldysh[Keldysh 1979], which modify the Coulomb po-

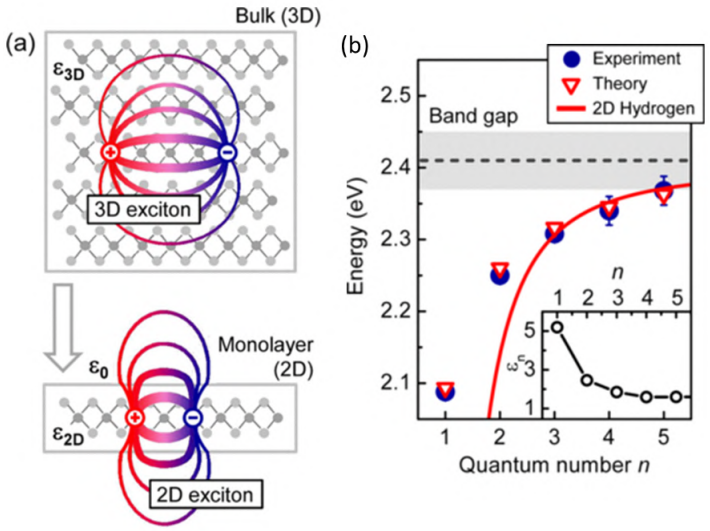

Figure 1.7: (a) Real-space depiction of electrons and holes forming excitons in three-dimensional bulk material and a quasi-two-dimensional monolayer. The variations in the dielectric environment are indicated schematically by different dielectric constants ϵ_{3D} and ϵ_{2D}, along with the vacuum permittivity ϵ_0. (b) Transition energies for exciton states as a function of the quantum number n, obtained from both experimental and theoretical data. The red curve represents the fit to the 2D hydrogen model for Wannier-Mott excitons, using data for $n = 3, 4, 5$. The gray band indicates the uncertainty in the quasiparticle band gap determined from the fitting process. The inset displays the corresponding effective dielectric constants. Reprinted figure with permission from [Chernikov 2014] Copyright (2024) by the American Physical Society.

tential to reflect the characteristics of point charges in thin layers. [Prada 2015]. The interaction potential $V_{2D}(r)$ is formulated using the modified Coulomb potential which accounts for environmental screening effects, given by the expression:

$$V_{2D}(r) = -\frac{e^2}{8\epsilon_0 \epsilon r_0}\left[H_0\left(\frac{r}{r_0}\right) - Y_0\left(\frac{r}{r_0}\right)\right]$$

where r_0 is defined as $d/(\epsilon_1 + \epsilon_2)$ and ϵ as $(\epsilon_1 + \epsilon_2)/2$. Here, d represents the thickness of the two-dimensional material, ϵ its bulk dielectric constant, and ϵ_1 and ϵ_2 the dielectric constants of the surrounding media, typically the substrate and vacuum. The parameter r_0 functions as a screening length that delineates the transition between two distinct behaviours of the potential; specifically, for $r < r_0$, the potential exhibits modified characteristics as defined by the equation. This theoretical framework aligns closely with the observed experimental data, providing a more accurate depiction of excitonic energy series.

1.5 van der Waals(vdW) heterostructures

In Section 1.3, we discussed that the TMDCs exhibit remarkable electronic and optical properties due to their layered nature and reduced dimensionality. In recent years, the assembly of isolated TMDC monolayers into precisely engineered heterostructures has opened up new areas of research for material science and nanotechnology. These intricate constructions often referred to as van der Waal(vdW) heterostructures are created by stacking layer by layer in a chosen sequence[Geim 2013]. This emerging field, supported by advancements in fabrication techniques and the foundational work with graphene, promises to evolve into a significant area of research. In this section, we explore the current landscape of vdW heterostructures and gain a deeper insight into the excitonic physics in these kinds of heterostacks. The combination of layers of different crystals results in the merging, of their properties and the creation of new artificial materials. Due to the exposure of electrons in the atomically thin 2D layers to interlayer coupling, the properties of van der Waals heterostructures are influenced not only by the individual monolayers but also by the interactions between these layers. van der Waals heterostructures hold potential for a diverse array of applications in both electronics and optoelectronics. Examples include graphene-based field-effect transistors with thin insulating hBN barriers[Britnell 2012], tunnelling diodes with negative differential conductance[Britnell 2013a], ultrathin photovoltaic devices[Bernardi 2013], photodetectors[Britnell 2013a] and light-emitting diodes[Withers 2015]. In traditional III-V, II-VI or group IV semiconductor heterostructures, the layers must have matching or a similar lattice constant to prevent strain, which can compromise the overall structural quality. This constraint significantly limits the combinations of materials that can be used effectively. In contrast, vdW heterostructures benefit from a vast array of different layered materials that can be stacked without concern for lattice mismatch. This flexibility allows for improved tailoring of the desired properties. For instance, sandwiching TMDC monolayers between hBN layers enhances their optical and electrical properties, overcoming the limitation faced by traditional epitaxial heterostrucutres[Cadiz 2017].

The heterostructures discussed in this thesis constitute the monolayers of the TMDC family. While various TMDCs possess the same crystal structure and exhibit qualitatively similar band structures, they differ in their lattice constants and have distinct absolute values of band gaps and band offsets relative to the vacuum level. The band alignment of TMDCs is shown in Figure 1.8. They give rise to a type-II band alignment in which the CBM and the VBM reside in different layers as was shown by first principle calculations[Kang 2013, Kośmider 2013, Terrones 2013]. Later this was also confirmed experimentally with the help of X-ray photoelectron spectroscopy and scanning tunneling microscopy (STM) [Chiu 2015]. Similarly, Wilson et al.[Wilson 2017] employed sub-micrometre angle-resolved photoemission spectroscopy (μ-ARPES) on $MoSe_2/WSe_2$ heterostructure to establish a type-II band alignment in the system. Due to the significantly stronger Coulomb binding energy in 2D TMDCs compared to conventional semiconductors like silicon or

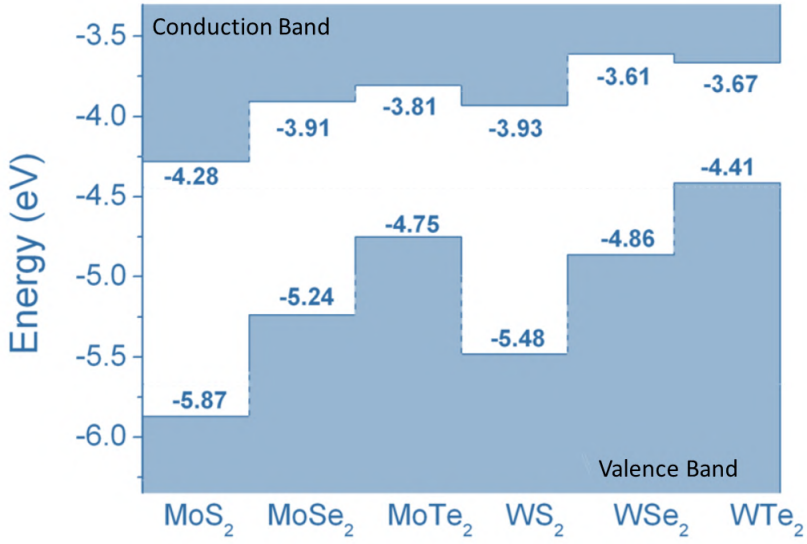

Figure 1.8: Band alignment of TMDCs calculated using Perdew-Burke-Ernzer(PBE) calculations. Reprinted from [Kang 2013], with the permission of AIP Publishing.

GaAs, interlayer excitonic states can be realized in vdW heterostructures.

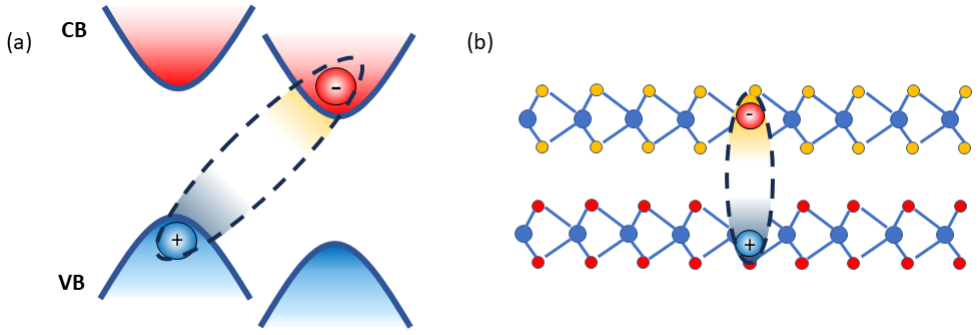

Figure 1.9: Schematics showing the interlayer exciton in (a) k-space and (b) real space with the charges localised in two different layers.

1.5.1 Interlayer excitons in type-II heterostructures

The band alignment in the heterostructures significantly affects the behaviour of excited states. It enables rapid charge transfer between layers, the creation of interlayer excitons (IX), and the maintenance of long-lasting spin and valley polarization in resident carriers. These excitons are tightly bound and highly localised in real space because of the large exciton binding energies (in hundreds of meV). As we discussed in the previous section, in a type-II band alignment of the

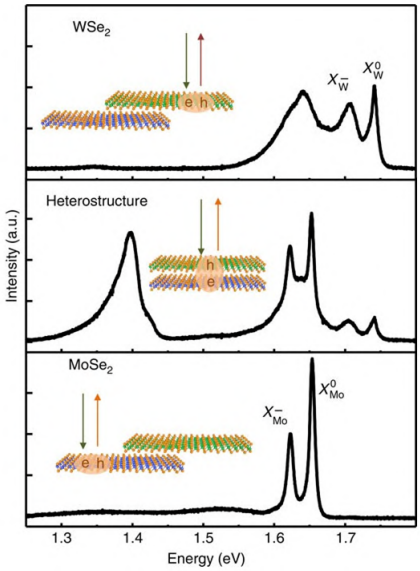

Figure 1.10: Low-temperature PL spectra of WSe_2, $MoSe_2$ monolayers and heterostructure highlighting the emergence of a low-energy IX peak at around 1.35 eV. Reproduced with permission from [Rivera 2015] copyright (2024) from Springer Nature.

heterostructure, the CBM of one layer is lower than the CBM of another layer and the VBM of the first monolayer is higher than the VBM of the other layer. The ultrafast transfer[Hong 2014, Ceballos 2014] of optically excited charge carriers results in the accumulation of e^- and h^+ in separate layers that are bound together by the Coulombic forces. This results in the formation of IX. The electrons and holes are localised in individual layers as shown in Figure 1.9. The first observation of IX was reported in a $MoSe_2$-WSe_2 system by Rivera et al. [Rivera 2015], where they noted that the lifetime of IX is an order of magnitude longer than that of intralayer excitons at 1.8 ns. In Figure 1.10, they show the emergence of a low energy spectral feature, identified as IX, confined only to the heterostructure region. Ross et al. demonstrated that the photocurrent amplitude from interlayer excitons is about 200 times smaller than that from intralayer excitons, implying that the oscillator strength of interlayer excitons is two orders of magnitude smaller than that of intralayer excitons[Ross 2017]. Using pump-probe spectroscopy, Kim et al.[Kim 2017] showed that perfectly valley-polarized holes are generated in WSe_2 within 50 fs via ultrafast charge transfer in the WSe_2/MoS_2 heterostructure[Hong 2014, Ceballos 2014]. These valley-polarized holes have a population decay lifetime exceeding 1 µs and a depolarization lifetime (or intervalley scattering lifetime) of over 40 µs at 10 K. Wilson et al. also established the binding energy of IX to be 200 meV in $MoSe_2/WSe_2$ heterostructure, which is an order of magnitude higher than that of GaAs structures[Wilson 2017].

The formation of IX in a type-II band alignment provides only a partial under-

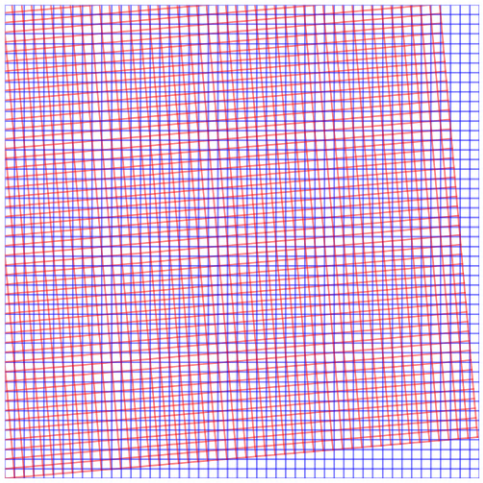

Figure 1.11: Scheme of the formation of moiré pattern from two square grids

standing of the overall picture. The electronic properties are governed by the interplay between two factors, firstly the formation of the moiré pattern and secondly the hybridisation of electronic states due to interlayer coupling[Sokołowski 2023]. These two factors are discussed in detail in the coming sections.

1.5.1.1 Formation of Moiré pattern

A moiré pattern is a phenomenon that occurs when two periodic, overlapping patterns with different periods or orientations interfere with each other, producing a new, slowly varying pattern, as illustrated in Figure 1.11. In the figure, we show two square grids with short periods but the moiré pattern formed from the interference of these two grids shows a longer periodicity. This visual effect demonstrates how slight misalignments or differences in the spacing of the grids can lead to the emergence of larger scale patterns, highlighting the moiré phenomenon's sensitivity to the relative orientations and spacing of the overlaid structures. In the context of two-dimensional TMDC layers, this effect becomes particularly significant. The moiré pattern in such heterostructures was first reported by Zhang et al. in a highly aligned MoS_2/WSe_2 heterostructure using STM[Zhang 2017a]. The periodicity of this moiré pattern can be precisely tuned, allowing for tailoring the optoelectronic properties of the resulting heterostructures. The variation in the local atomic arrangement across a moiré supercell leads to a slow-varying, and a long-period potential variation known as the moiré potential [Andersen 2021, Mak 2022, Wu 2018, Huang 2022]. The size of a single moiré supercell, a_M is given by[Ribeiro-Palau 2018]:

$$a_M = \frac{(1+\delta)a_0}{\sqrt{2(1+q)(1-cos\theta)+\delta^2}} \tag{1.7}$$

where, θ is the rotational mismatch between the layers, δ is defined as the

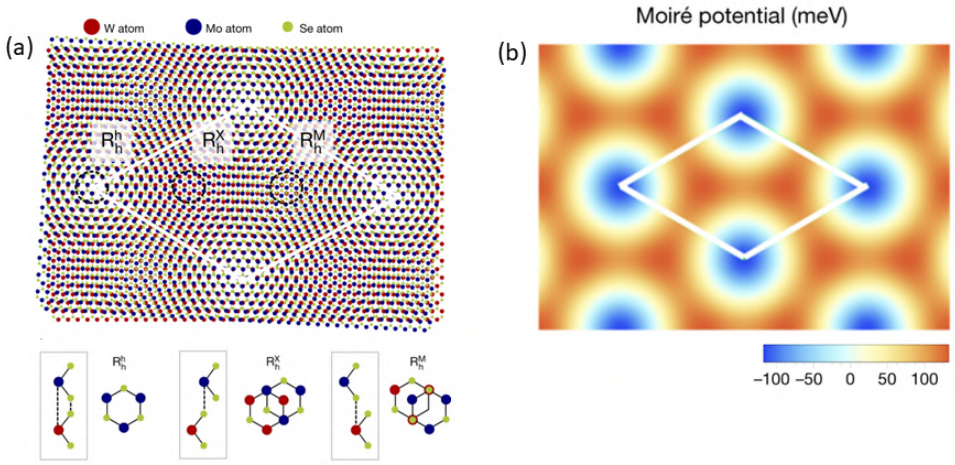

Figure 1.12: (a) Atomic alignments in a highly aligned $MoSe_2/WSe_2$ heterostructure. (b) the moiré potential for the interlayer exciton transition is illustrated, highlighting a local minimum at the R_h site. Reproduced with permission from [Tran 2019]. copyright (2024) Springer Nature.

mismatch in lattice, as$|a_0' - a_0|/a_0$; a_0 and a_0' are the lattice constants of the two constituent monolayers ($a_0 < a_0'$).

When periodic TMDC layers are stacked with a slight twist or lattice mismatch, the interference between their atomic structures generates a moiré pattern, as illustrated in Figure 1.12(a). In the context of moiré superlattices, the parallel stacking near a 0° twist angle and the antiparallel stacking near a 60° twist angle are referred to as R-type and H-type, respectively. In R-type (H-type) stacking, there are three high-symmetric points which preserve the three-fold rotational symmetry, denoted as R_h^h, R_h^X, and R_h^M (H_h^h, H_h^X, and H_h^M). Figure 1.12 (a), illustrates the high symmetric points, R_h^h, R_h^X, and R_h^M in a moiré supercell of the $MoSe_2/WSe_2$ heterostructure. These high symmetric points represent local extremas (shown in Figure 1.12(b))in the energy landscape where the excitons are confined and they impose different site-specific optical selection rules[Yu 2017a, Yu 2015]. It is important to note that these optical selection rules are set by the relative position of atoms in real space.

The extent of interlayer coupling in a heterostructure determines the depth of the moiré potential. First principle calculations have estimated the depth of the moiré potential to be 100-200 meV[Tran 2019]. Figure 1.12(b) shows that the moiré potential change continuously inside a moiré supercell. The spatial map shows the site-specific moiré potentials for the IX. This has also been confirmed experimentally by STM on CVD-grown MoS_2/WSe_2 heterostructure[Zhang 2017a]. Tran et al. reported the observation of multiple interlayer excitons (IX) in $MoSe_2/WSe_2$ heterostructures, as shown in Figure 1.13(a). The PL emission was fitted with multiple Gaussians and it revealed the multiple IX resonances spanned over 70 meV,

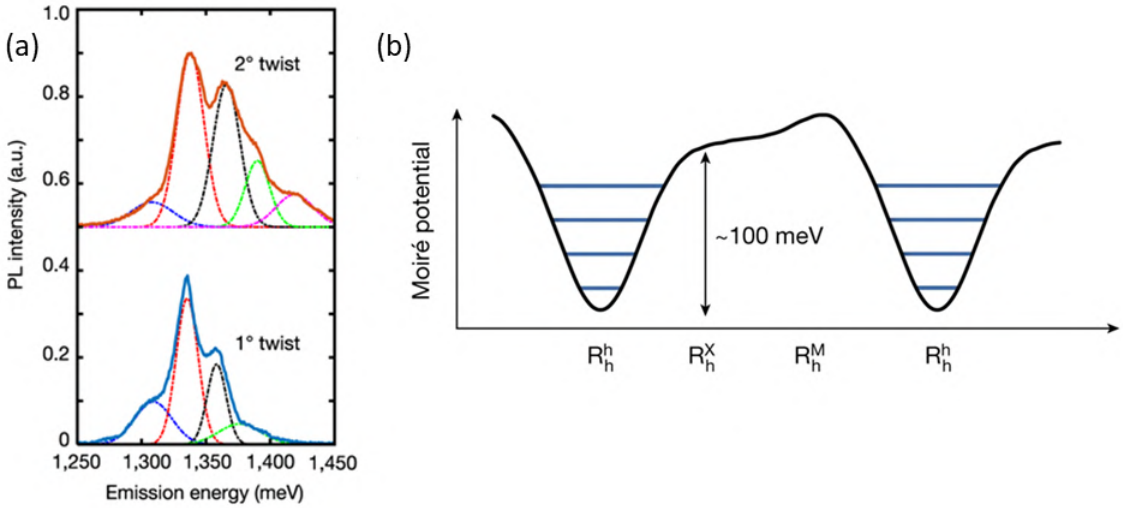

Figure 1.13: (a) PL spectra from heterostructure regions of twist angles 2°(top) and 1°(bottom) fitted with Gaussian functions. (b) Schematic showing the spatial variation of moiré potentials at different symmetric points of the supercell confining multiple excitonic resonances.Reproduced with permission from [Tran 2019], copyright (2024) Springer Nature.

which suggests that the order of the moiré potential is of the order of 100 meV. The Bohr radius of the IX is about 1 nm, in contrast to the 20 nm moiré period. Thus, the exciton can be picturized as a particle with a wavepacket moving through the moiré potential[Yu 2017a, Gillen 2018]. The movement of the centre of mass of the exciton can be explained using the following equation:

$$H = \hbar\Omega_0 + \frac{\hbar^2 k^2}{2M} + \Delta(r) \tag{1.8}$$

where $\hbar\Omega_0$ is an energy constant, $\frac{\hbar^2 k^2}{2M}$ is the kinetic energy of the centre-of-mass, $\Delta(r)$ is the exciton moiré potential energy and M is the exciton mass.

They also establish that more than one IX resonance can be confined inside a deep moiré potential as illustrated in Figure 1.13(b). It shows the variation of the moiré potential across different points inside a moiré supercell and illustrates the different confined IX resonances in these potentials.

1.5.1.2 Interlayer hybridization of electronic states

In this section, we will explore how the stacking of two different TMDC layers affects the electronic structure of these heterostructures. As the two monolayers begin to couple electronically, their band structure changes from that of isolated monolayers to that of an integrated heterostructure or bilayer. This characteristic provides a unique mechanism to tune the electronic properties of these materials through the careful selection and combination of different TMDC monolayers. Stacking distinct

TMDC layers gives us precise control to tune the electronic properties based on the choice of materials. Combining these TMDC monolayers has shown promising possibilities in tuning the electronic structure and the optical properties of the IX.

This stacking of different materials leads to what is known as hybridisation, which arises from the overlap of the atomic orbitals of individual layers. As we discussed in Section 1.3, the atomic orbitals in an individual TMDC layer are largely determined by the d orbitals of the transition metal and the p orbitals of the chalcogen atoms[Splendiani 2010, Liu 2013]. The interlayer coupling in TMDC heterostructures arises from the overlap of the atomic orbitals of the participating layers. The chalcogen atoms are located at the interface of these layers, making their orbitals specifically the p orbitals more likely to overlap when the two layers are stacked thus affecting the states around the Γ-point in the Brillouin zone. This overlap leads to significant hybridisation effects at these orbital states[Kuc 2011, Raja 2018]. Different band structure models have shown that in $MoSe_2/MoS_2$ and MoS_2/WS_2 heterostructures, the band structure is significantly affected by the interlayer hybridization [Su 2016, Hagel 2021]. This hybridization places the VBM at the Γ-point and the CBM at the K point of the Brillouin zone. Thus the IX formed is indirect in both real and k-space, it means that the e^- and h^+ occupy the different points in the Brillouin zone (i.e. e^- at K point and h^+ at Γ point). For example, Tongay et al. studied a highly aligned CVD-grown MoS_2/WS_2 heterostructure and documented the presence of both direct and indirect transitions in the PL spectrum from the heterostructure region[Tongay 2014]. They also noticed the position of the indirect peak changing rapidly with the degree of coupling (annealing time) and attributed it to the phonon-assisted indirect bandgap transition. To support this claim DFT calculations incorporating spin-orbit coupling (SOC) interactions were performed on the heterostructures, as shown in Figure 1.14(a), which were calculated at the equilibrium interlayer distance of $d = 6.23$ Å. The orbital character depends on the orbital contribution from the participating layers, i.e. the VBM and CBM values depend greatly on the interlayer coupling. Figure 1.14(b) illustrates the influence of varying interlayer distances on the VBM and CBM at high-symmetry points. The valence band maximum (VBM) at the Γ point and the conduction band minimum (CBM) at the K-Γ point arise from the hybridization between the d_{z^2} orbital of Mo or W and the p orbital of S (d_{z^2} of Mo or W and p of S), whereas the VBM (CBM) at the K-point is predominantly composed of the Mo- or W- $d_{x^2-y^2}$ and d_{xy} orbitals. Due to the distinct orbital character, the VBM and CBM energies at these high symmetry points exhibit varied responses to interlayer coupling.

For instance, altering the interlayer distance results in a 50–70 meV change at the K-point, while the VBM at Γ, involving $p - d$ orbital coupling, undergoes significant modifications. This sensitivity of the VBM at the Γ point is attributed to P_{indirect} emission, which shifts with thermal annealing due to phonon-assisted optical transitions across the Γ(VBM) → K(CBM) indirect bandgap. Conversely, the photoluminescence (PL) peak P_{hetero} at 1.95 eV is approximately 200 meV below P_{WS2}, a discrepancy lower than the accuracy of density functional theory

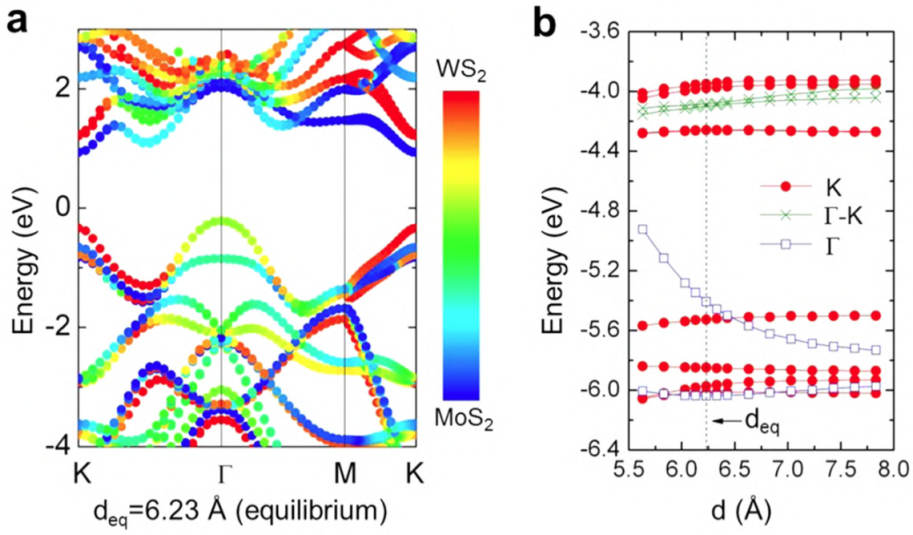

Figure 1.14: DFT calculation illustrating the transition from direct to indirect bandgap on MoS_2/WS_2 heterostructure. (b) The energy levels of the band-edge state as a function of the interlayer distance *d*. The vertical dotted lines indicate the equilibrium distance *d*. Reprinted (adapted) with permission from [Tongay 2014]. Copyright (2024) American Chemical Society.

(DFT) calculations, complicating concrete conclusions about the exact origin of P_{hetero} emission within the DFT framework.

In the case of $MoSe_2/WSe_2$ heterostructure, the CBM and VBM are located in the different layers but still at the $K-$ point of the Brillouin zone[Hagel 2021, Choi 2021]. This was also confirmed on the same heterostructure experimentally by Wilson et al. using angle-resolved photoemission spectroscopy (μ-ARPES) [Wilson 2017]. They also establish that the hybridisation strongly affects the bands at Γ point but the valence and conduction band edge remains at K points.

Chapter 2

Experimental Techniques

Contents

This chapter outlines the experimental techniques employed in this thesis. It begins with elucidating the sample fabrication method, followed by a brief introduction to the post-fabrication AFM ironing technique. Subsequent sections provide insights into the pump-probe setup utilized for conducting transient absorption spectroscopy on encapsulated monolayer hybrid heterostructures.

2.1 Fabrication of encapsulated $MoSe_2/MoS_2$ Heterostructures

As we discussed in detail in chapter 1, TMDC monolayers not only underpin a wide spectrum of applications but also offer a modular approach to material design. Research has shown that by mechanically stacking the layers of TMDCs, one can fabricate heterostructures[Britnell 2013b]. Fabricating these heterostacks has revolutionised the investigation of TMDCs allowing us to explore new paradigms in material science. This thesis and this chapter specifically describe the steps undertaken to realise such heterostructures in detail, starting from the isolation of monolayer flakes to the final heterostructure assembly.

All of the samples along with their fabrication described in this section were performed by me at the 2D-Foundry facility within the Materials Science Factory at the Instituto de Ciencia de Materiales de Madrid (ICMM-CSIC) in Madrid, Spain. The samples fabricated are the heterostacks of monolayers of $MoSe_2$ and MoS_2 sandwiched between layers of hBN. To have a better visualisation of the sample structure, the schematics are presented in Figure 2.1. It has been shown that encapsulating these stacks in hBN has provided access to their intrinsic properties[Dean 2010, Cadiz 2017, Tongay 2013]. Realising this configuration involves a two-stage fabrication process. Initially, the isolation of MoS_2 and $MoSe_2$

monolayers is performed. Subsequently, the layers of distinct materials are stacked in a predetermined sequence. Finally, the resulting structure is transferred onto the desired substrate. These steps are discussed in detail in the subsequent subsections.

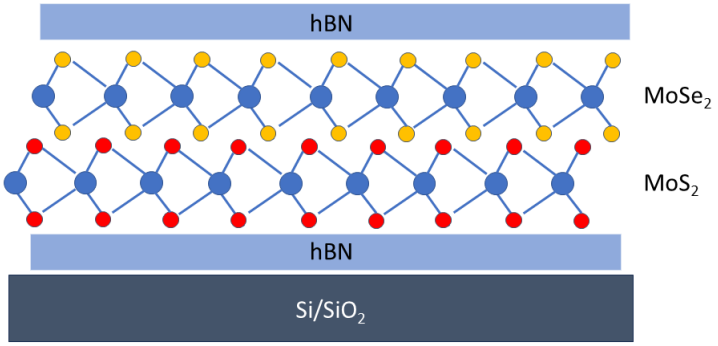

Figure 2.1: Schematics of the fabricated heterostructure.

2.1.1 Exfoliation and isolation of monolayer TMDCs

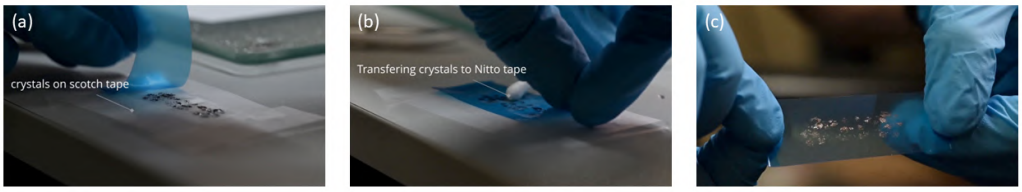

Figure 2.2: (a) The process involves transferring thicker layers of the material on the scotch tape from the crystal. (b) Nitto tape is used to exfoliate thinner layers from the scotch tape (c) Layers are thinned down after subsequent exfoliations.

Monolayers of TMDCs were exfoliated from bulk crystals of MoS_2 (Molly Hill mine, Québec, Canada) and $MoSe_2$ (HQ Graphene, Inc.) using a technique called micromechanical cleaving. In parallel, hexagonal boron nitride (hBN) crystals, procured from HQ Graphene and the National Institute for Materials Science (NIMS) in Japan, were similarly exfoliated to prepare for the subsequent encapsulation process. The initial exfoliation process starts with the use of a scotch tape, as shown in Figure 2.2(a). The scotch tape was first stuck to the bulk crystal and then removed to peel off thicker layers of the TMDCs. This step helps in the preparation of the initial layers of the material for further exfoliation. Following the initial step, blue nitto tape (from Nitto Denko Corp.) is applied to the scotch tape surface with

the thicker material and then removed to extract additional thinner layers of the material as shown in Figure 2.2(b) and (c).

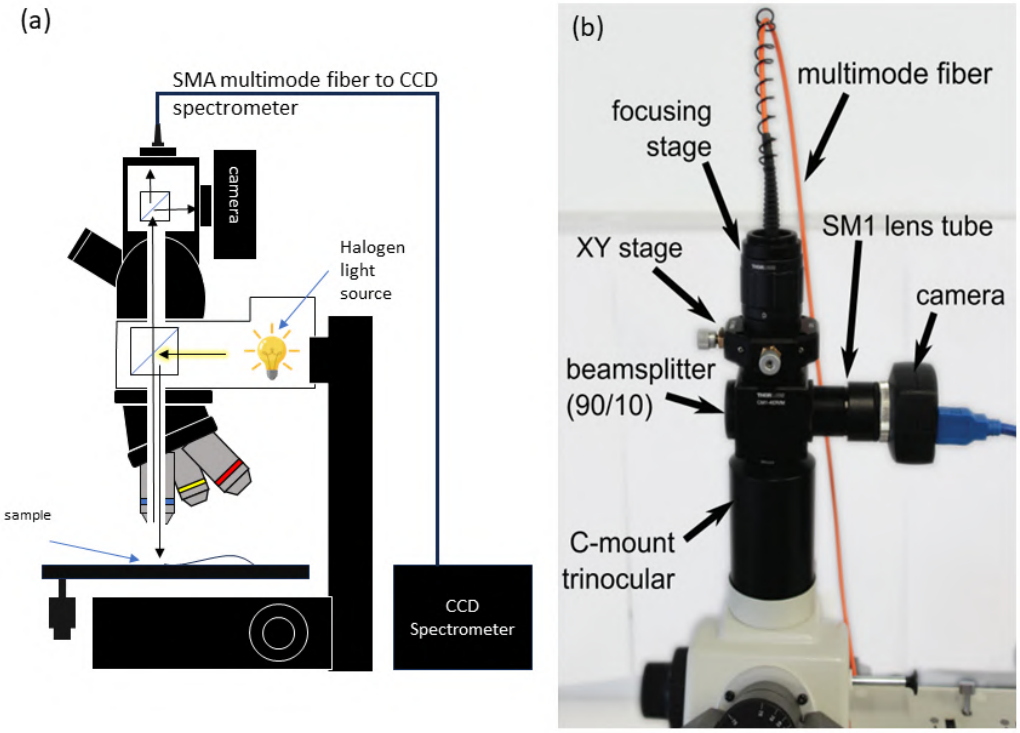

Figure 2.3: (a) Schematics showing the setup used to isolate and characterise the monolayer flakes. (b) Detailed photograph of the modified trinocular setup showing different parts of the microscope. Used with permission of IOP Publishing Ltd, from [Frisenda 2017]; permission conveyed through Copyright Clearance Center, Inc..

Throughout the process of subsequent exfoliations, the layers are observed under the microscope. Care was taken to make sure the layers were not under-exfoliated, which arises if the layers are thicker and there is not enough presence of thinner layers. It was also checked if we did not have over-exfoliation. In case of over-exfoliation, the flakes start to shatter and break into pieces. Through the optimisation, we concluded that 6-7 subsequent exfoliations are suitable for achieving the ideal count of thinner or monolayer flakes.

Once we exfoliated thinner layers on the nitto tape, to isolate the monolayers under the microscope (Motic BA310), we again transferred the material from the nitto tape to a fresh polydimethylsiloxane (PDMS) stamp. A customized trinocular setup, schematics shown in Figure 2.3(a), was employed for the exploration of monolayers of TMDCs. This modified setup (shown in Figure 2.3(b)) incorporates

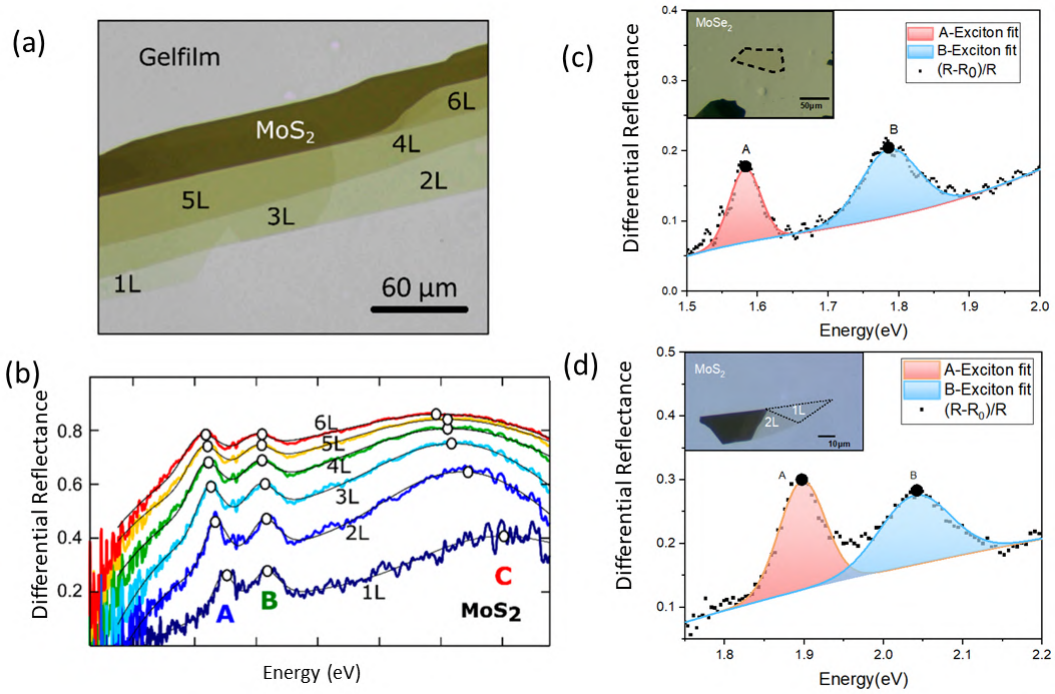

Figure 2.4: (a) Shows the optical contrast variation across the thickness of different layers of MoS_2. (b) Illustrates the shift in the excitonic resonances in the differential reflectance spectra concerning layer numbers, Reproduced with permission from [Niu 2018] published by MDPI Nanomaterials. Differential reflectance spectra of the (c) $MoSe_2$ and (d) MoS_2 flake as marked by dotted lines in the inset.

.

a 90:10 beam-splitter(BS) mounted on the C-mount to help divide the light beam into two paths, one leading to the camera and the other to a fibre-coupled charge-coupled device (CCD) spectrometer (Thorlabs CCS200/M, Newton, NJ, USA). This spectrometer facilitates the collection of reflectance data from individual flakes to determine the exact thickness of the flakes. This setup not only facilitated the isolation of monolayers based on optical contrast but also allowed me to collect in-situ reflectance data from individual flakes. Optical contrast is very helpful for the initial estimate of the flake thickness. Figure 2.4(a), shows the transmission mode optical microscopy image of an exfoliated MoS_2 flake, displaying variation in the optical contrast of different layer numbers. MoS_2 flakes appear darker under transmission light compared to the substrate, in this case, PDMS, and their darkness increases with increasing thickness. This observation aligns with the fact that PDMS film has a transmittance of approximately 95%, whereas the transmittance of a monolayer MoS_2 is less than 90% under visible light and further decreases as the layer thickness of the flake increases[Li 2014a, Castellanos-Gomez 2013]. In Figure 2.4(a) we can see the contrast gradually fades when we approach thinner and thinner layers. There is a similar strong layer-dependent transmission for other TMDCs like

$MoSe_2$, WS_2 and WSe_2.[Niu 2018]. Once we have a flake which corresponds to the optical contrast of the monolayer, we then collect the reflectance spectra from the flake. The differential reflectance spectrum was calculated as $(R - R_0)/R$ and it has a direct correlation to the wavelength-dependent absorption coefficient of the material $\alpha(\lambda)$ as[Dhakal 2014]:

$$\frac{R - R_0}{R} = \frac{4n}{{n_0}^2 - 1}\alpha(\lambda) \tag{2.1}$$

where R denotes the spectra reflected from the flake, R_0 denotes the spectra reflected from the PDMS substrate, n is the refractive index of the flake and n_0 is the refractive index of the substrate. As shown in Figure 2.4(b), the differential reflectance spectra for different layer numbers of MoS_2 show the shift of the A and B exciton resonances as the layer number changes. In Section 1.3, we briefly discussed about these excitonic transitions. The exact energies at which exciton peaks appear are dependent on the material properties, as these features are determined by the band structures of the material. In Figure 2.4(c) the exciton peaks are labelled as A, B, C as per the established naming convention of the excitons in semiconducting TMDCs in the literature [Splendiani 2010, Mak 2010, Zhao 2013]. The A exciton peak near the absorption band edge corresponds to the direct band gap transitions at the K point in the Brillouin zone[Mak 2010, Splendiani 2010]. At slightly higher energy, another prominent peak, known as the B exciton, is observed in the differential reflectance spectra of TMDCs. This peak corresponds to another direct transition at the K point namely the B exciton. The higher energy transition at the K point is attributed to the splitting of the valence band caused by the spin-orbit interaction. In multi-layer systems, the valence band splitting is driven by a combination of spin-orbit coupling and interlayer interactions. Another broad feature appears in the differential reflectance spectra higher in the energy to A and B excitons, identified as C exciton.

In Figure 2.4(c) and (d) we present the differential reflectance spectra from $MoSe_2$ and MoS_2 monolayers respectively. The sum of Gaussian peaks and broad background were used to fit the spectra and ascertain the position of the peaks. The inset in the plots shows the respective layers for which the differential reflectance measurement was conducted.

The A exciton peak red-shifts with increasing thickness across TMDCs[Niu 2018]. B exciton shows very weak dependence on the number of layers. The layer dependence of the A and B resonance from µ- reflectance and µ- transmission measurements are plotted in Figure 2.5. This dependence is primarily due to the changes in dielectric screening with the number of layers, which in turn affects the exciton binding energy[Arora 2015]. While spin-orbit splitting remains crucial, the variation in a dielectric environment with layer number significantly influences the excitonic resonance. By analyzing these transition energies from the reflectance spectra, I was able to determine the number of layers in the samples.

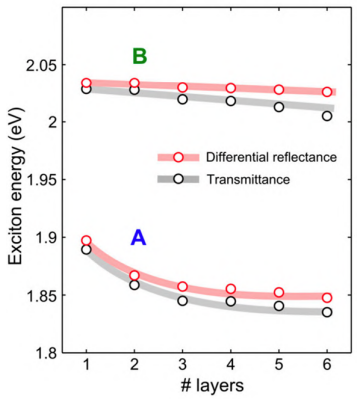

Figure 2.5: Comparison of exciton energies derived from differential reflectance and transmittance measurements on the MoS_2 flake. Reproduced with permission from [Niu 2018] published by MDPI Nanomaterials.

2.1.2 Fabrication of Heterostructures

After successfully isolating the monolayer flakes, the next step involves stacking these monolayers to create the heterostructure. To achieve this, we employ a nail polish stamp for the pickup and transfer of individual flakes. According to the schematics of the heterostructure illustrated in Figure 2.1, the process begins with the pickup of the top hBN, followed by the monolayer flakes, and then the bottom hBN. In the final step, the entire stack is transferred to the target substrate, and meticulous cleaning is performed to eliminate any residues from the nail polish. Subsequent sections provide a detailed description of these procedures.

2.1.2.1 Preparation of nail polish stamp

The fabrication of the heterostructure samples involves the use of commercially available nail polish from Revlon, Inc. [Haley 2021, Rebollo 2021]. The fabrication process starts with the preparation of a nail polish stamp. This entails placing a tiny, approximately 3 mm in diameter, circular piece of PDMS onto a glass slide. Figure 2.6(a) shows the precise placement of the PDMS disk on the glass slides with the help of tweezers. Figure 2.6(b) shows the schematics of the nail polish stamp. A carefully positioned piece of Kapton tape serves a triple role. Firstly, it ensures the secure placement of the PDMS; secondly, it furnishes a geometrically optimal hemispherical surface for the nail polish droplet; and lastly, it exhibits a capacity to endure elevated temperatures required during the fabrication process. The hemispherical surface provides exacting control for the precise pickup and drop-off of flakes. Figure 2.6(c) shows the final prepared stamp. Once the surface is prepared, a small circular droplet of nail polish, approximately 1 mm in diameter, is applied using a solder wire loop. Subsequently, the stamp is placed on a hot plate (shown in Figure 2.6(d)) set at around 50°C to eliminate any strain or fatigue in

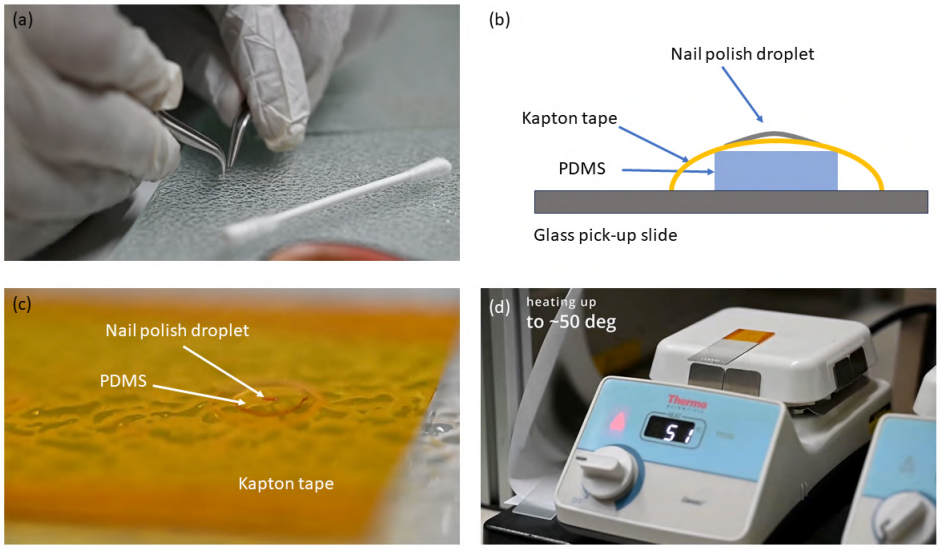

Figure 2.6: (a) It shows the isolation of the PDMS layer from the protective layerings and placing it on the glass slide. (b) A side-view schematic of the stamp used to pick up and transfer flakes (c) Photograph of the stamp with the nail polish droplet (d) The stamp is heated to about 50 °C to give better flow and release any strain in the nail polish droplet.

the droplet.

2.1.2.2 Pick-up and transfer of the flakes

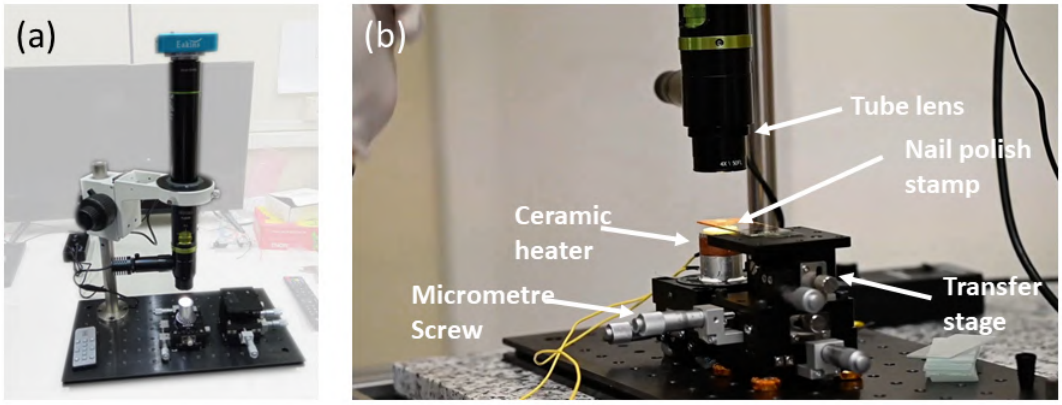

Figure 2.7: (a) Modified transfer setup used for pickup and transfer of flakes (image adapted from [Bastante 2023]). (b) Image showing different parts of the transfer stage during a transfer.

Figure 2.7(a) presents the setup used for the pick-up, transfer and fabrication of the heterostructure samples. The setup constitutes a coaxial illumination zoom lens

system (OPTEM Fusion 7:1) and the 3-axis micro-manipulator stage. Figure 2.7(b) shows the different components of the setup. Our methodology employs a transfer stage equipped with micro-manipulators in the x, y and z directions, coupled with a zoom lens camera system for precise pickup and transfer of microsized flakes onto target substrates.

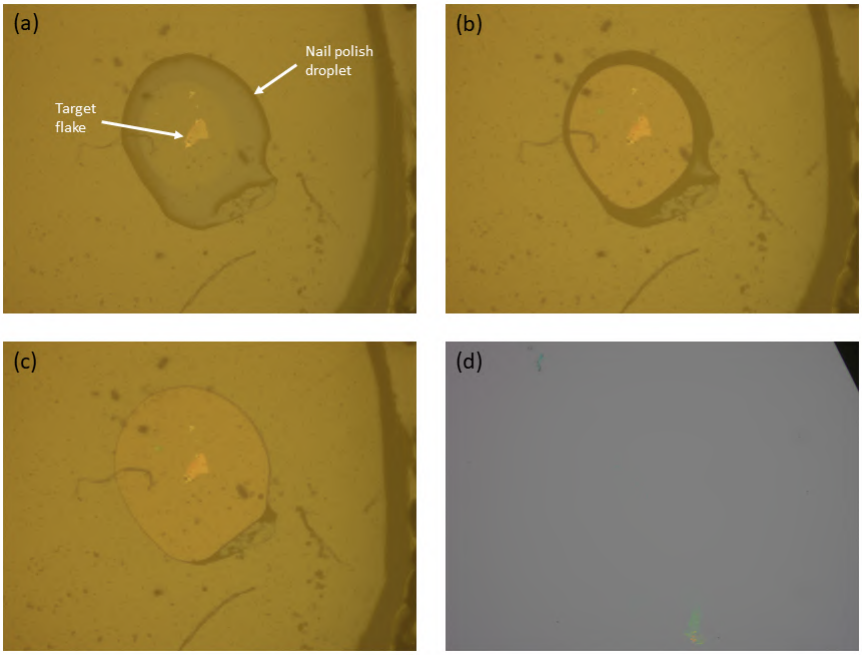

Figure 2.8: (a) Top view from the camera, shows the alignment of the nail polish droplet on the target flake. (b) The nail polish droplet comes in contact with the flake and the substrate. (c) The stamp is further moved down to get complete contact of the nail polish droplet with the substrate and the flake. (d) The flake is picked up by a fast motion of the stamp thus leading to successful pickup.

Once the nail polish stamp is prepared, the desired monolayer flakes are picked up by aligning the centre of the nail polish droplet on the flake as shown in Figure 2.8(a) and the stamp is lowered to bring the nail polish droplet into contact with the desired flake as shown in Figure 2.8(b). Once the nail polish droplet completely covers the flake, the stamp is swiftly raised or moved in the z direction with an impulse.

The heat-assisted fabrication technique necessitates intermittent heating and reheating during subsequent pickups and also in the final drop step. Initially, the Si/SiO_2 substrate is heated to 50°C, facilitated by the modified transfer stage equipped with a heating element (shown in Figure 2.9(a)). The heating element constitutes a ceramic heater of diameter 20 mm and operates at a maximum voltage of 24 V. The plot in Figure 2.9(b) shows the correlation between heating power

(measured in watts) and temperature (measured in degrees) depicted for the heater under two distinct conditions. The first condition, represented in orange, shows the temperature response when the heating power is applied directly to the heater. The second condition illustrates the temperature measured on a sample that is affixed to the heater. In this fabrication technique, the top flake is picked up first, and the sequence concludes with the pickup of the bottom flake. In our stack's material sequence, we initiate pickup with the top hBN layer (approximately 10-15 nm thick), followed by the TMDC monolayers, and conclude with the bottom hBN layer (approximately 200 nm thick). hBN offers a seamless, atomically flat surface, providing an ideal foundation for the subsequent flakes constituting the heterostructure.

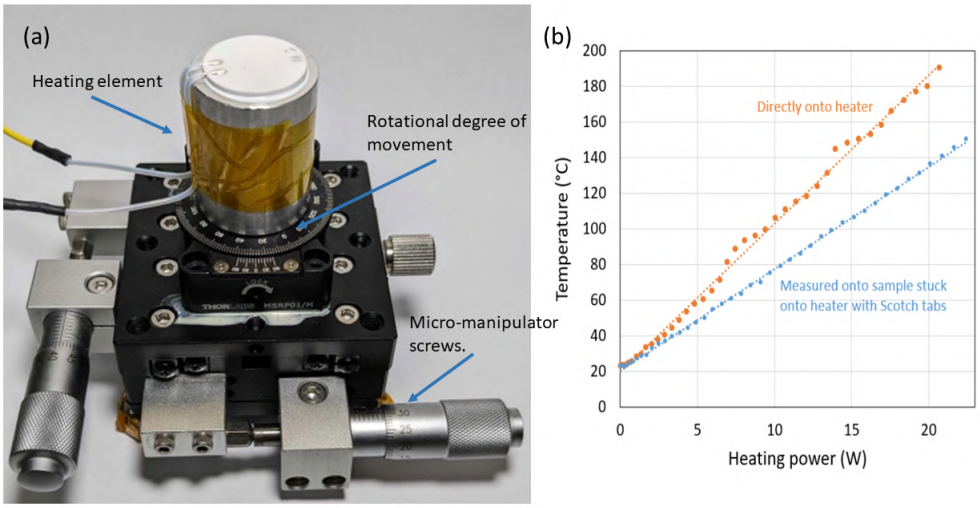

Figure 2.9: (a)The setup has an additional degree of freedom to adjust the angle between the participating flakes. The modified transfer stage is fitted with a ceramic heating stage. (b) Plot showing the temperature of the heating element vs heating power. (adapted from [Bastante 2023])

To create aligned or twisted heterostructures, the transfer setup incorporates an additional degree of freedom as shown in Figure 2.9(a), enabling precise angle adjustment between the edges of the monolayer flakes. The heterostructure is assembled sequentially picking up individual flakes in the desired order. For the fabrication of aligned (60 deg or 0 deg) heterostructures, the crystallographic edges of the monolayer flakes are aligned parallel to each other as shown in Figure 2.10(a). Distinguishing between 0 and 60-degree twist angles between the flakes is not possible during fabrication. At a 0-degree twist angle, the layers are perfectly aligned, maintaining the original symmetry and potentially leading to constructive interference of the electronic states at the K and K′ points of the Brillouin zone, whereas at 60 degrees twist, one layer's K point is aligned with the other layer's K′ point leading to large scale reconstruction of the electronic states. This has been dis-

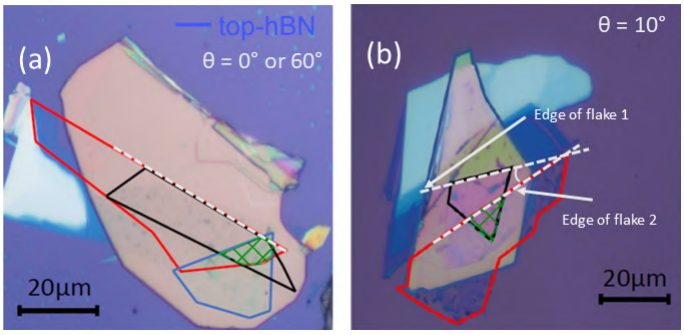

Figure 2.10: Optical micrograph of a (a) Highly aligned (c) Twisted heterostructure, fabricated by the method discussed.

cussed extensively in chapter 1. We employed second harmonic generation (SHG) spectroscopy to determine this during the optical characterisation[Sokołowski 2023].

An inherent problem surrounding the fabrication technique using nail polish is the poor visibility of the flakes during the stamping process. This issue is an ingrained aspect of the setup and should be managed as such. This problem was especially evident when creating twisted heterostructures, as observed in Figure 2.10(b). Due to the obscurity of the edges, there is a degree of uncertainty that impacts the accuracy of the twist angle determination. For instance, an attempted twist angle of 10 degrees resulted in a measured angle of only 6.4 degrees, highlighting this methodological constraint.

Following each pickup, the stamp is carefully placed on a hot plate set at 50°C for 1-2 minutes. This critical step serves the dual purpose of relieving any stress or fatigue present in the flake or droplet and promoting the smooth reflow of the nail polish.

2.1.2.3 Transferring the final heterostructure to the target substrate

In the conclusive phase of the fabrication process, the assembled hetero-stack is gently released onto the designated target substrate. The deposition process commences by carefully adjusting the substrate temperature to approximately 100°C.

The stamp is gradually retracted to ensure a controlled descent, allowing the nail polish droplet, along with the hetero-stack, to seamlessly melt onto the substrate. As you slowly move away from the substrate, the nail polish forms a tunnel-like feature as shown in Figure 2.11(a). Figure 2.11(b) and (c) provide a detailed visual depiction from a top view, showcasing the exact process of the nail polish droplet melting and enveloping the heterostructure within, the designated substrate.

To eliminate any lingering traces of nail polish, the final stack undergoes a thorough cleansing process. It is immersed in a bath comprising acetone, isopropyl alcohol (IPA), and distilled water. Subsequently, the stack is meticulously dried using a nitrogen gun to ensure a pristine finish as shown in Figure 2.11(d).

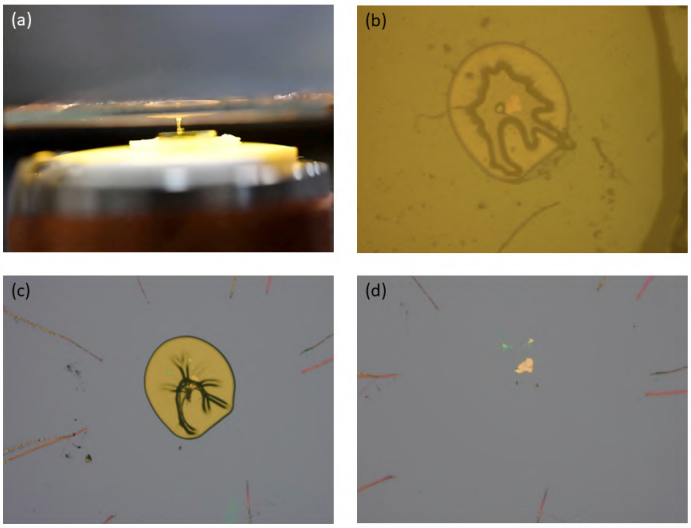

Figure 2.11: (a) Side view showing the retraction of stamp after melting the nail polish droplet onto the target substrate. (b) The top view from the camera shows the deformation of the nail polish droplet as the stamp moves away from the substrate. (c) The final blob of the nail polish contains the heterostructure inside. (d) After treating it in IPA, acetone and DI water and drying it with the nitrogen gun, we have our final heterostructure.

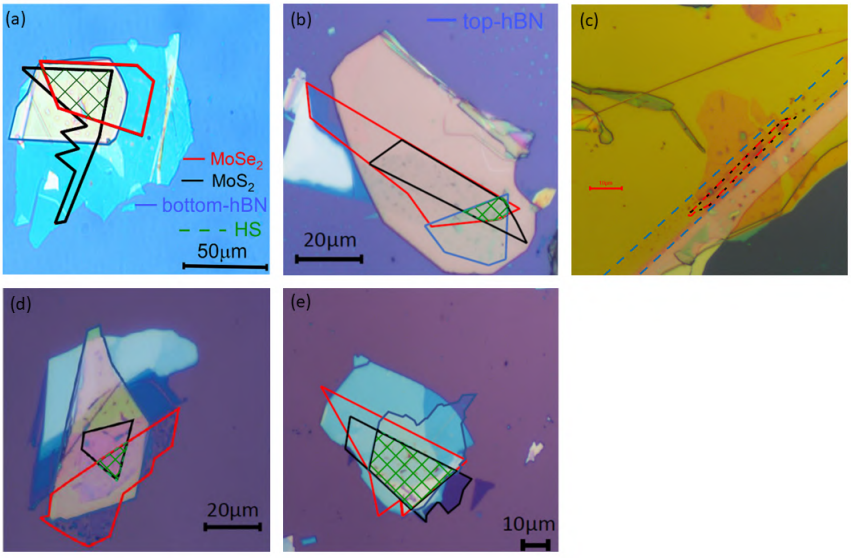

Figure 2.12: The top panel of images presents the final images of the samples fabricated using this technique (a)Sample A (b) Sample B (c) Sample C (d) Sample D (e) Sample E.

We present the final heterostructures in the Figure 2.12. In total, we successfully fabricated 5 samples. Three of which were highly aligned samples and two of the lot were fabricated with twist angles. The green mesh regions indicate the effective heterostructure regions which are encapsulated. The table 2.1 presents the different twist angles for the individual samples. These twist angles were determined using the SHG spectroscopy by our team in Toulouse.

Sample	Twist angle
Sample A	57.2
Sample B	56.3
Sample C	1.3
Sample D	53.6
Sample E	6.4

Table 2.1: Twist angles of different samples

2.2 Atomic Force Microscopy(AFM) Characterisation and Ironing

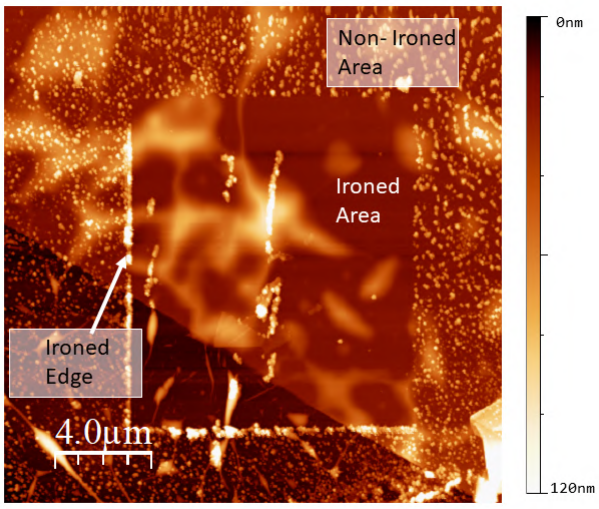

Figure 2.13: AFM Topography image highlighting the ironing edge and illustrating the contrast between the ironed and non-ironed areas.

A significant obstacle in the fabrication of these heterostructures lies in inherent challenges associated with inhomogeneity[Yu 2017b, Gasparutti 2020, Rosenberger 2018] that comes due to the fabrication method itself. The qual-

ity of interfaces between the layers becomes crucial when aiming to extract the true intrinsic properties. Despite employing various preparation techniques such as transfer in inert atmospheres[Jung 2019] and annealing[Kretinin 2014], achieving long-range homogeneity at the interface remains a challenge. In this study, we utilize AFM ironing[Rosenberger 2018, Goossens 2012, Kim 2019] as an additional step to further mitigate disorders in the heterostructure interface between the layers. The comprehensive surface characterization, including the ironing process, was conducted by me at the Materials Science Factory at the Instituto de Ciencia de Materiales de Madrid (ICMM-CSIC) in Madrid, Spain. It was done using a commercially available Atomic Force Microscopy (AFM) setup from Nanotec Inc., operating seamlessly under ambient conditions. Surface analyses were conducted in both contact and dynamic modes using the same probe. The PointProbe Plus FMR probe from Nanosensors, featuring a normal force constant and resonant frequency of 2.8 N/m and 75 kHz, respectively, was utilized for measurements. To enhance precision, the Sader method was implemented for probe calibration, as outlined by Sader et al.[Sader 1999].

The characterization process commenced with dynamic mode scanning to identify the heterostructure region, plan areas for pressure-induced modifications, and, crucially, capture the surface morphology of the structure. Following the completion of surface characterization in dynamic mode, the setup transitioned to contact mode. Here, a predetermined force for the ironing process was set, and the designated area was systematically scanned. This procedure was iterated for various forces within the same heterostructure, facilitating a direct comparison of pressure-induced effects on the optical properties of TMDC stacks.

Post-ironing experiments, the scanning mode was reverted to dynamic mode, and a large scan area was acquired to comprehensively analyze the impact of ironing on the heterostructure's morphology. The subsequent image analysis was carried out using the WSxM free software, ensuring a rigorous examination of the structural changes induced by the ironing process[Horcas 2007]. This technique, along with the subsequent effects of the ironing process, is discussed in detail in the Chapter 3 of the thesis.

2.3 Optical Characterisation Techniques

2.3.1 Steady-state µPL and µ-Reflectivity Setup

The optical characterization of the samples investigated in this thesis was performed by me in the optical laboratory located in LNCMI-Toulouse, France. The laboratory is equipped with different instruments and setups that enable us to employ a diverse range of characterization techniques. These techniques include but are not limited to, µ-PL, µ-reflectivity, photoluminescence excitation(PLE), polarisation-resolved spectroscopy, as well as temperature and power-dependent measurements.

The initial step in this involves placing the sample on the cold-finger of a closed-cycle helium flow cryostat. This cryostat is equipped with a quartz optical window,

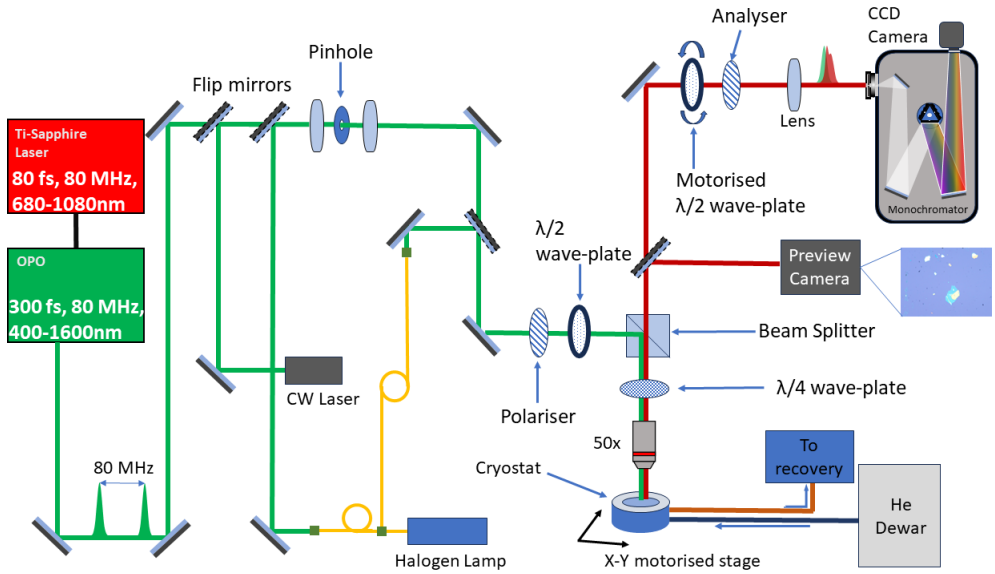

Figure 2.14: Schematics of the micro-PL and reflectivity setup. This setup includes (i) Optical Parametric Oscillator (OPO) pumped by a Ti:Sapphire laser, (ii) CW laser emitting at 532 nm or 648 nm for excitation and a monochromator and CCD in the detection. A halogen lamp was used to collect reflectivity data from the sample.

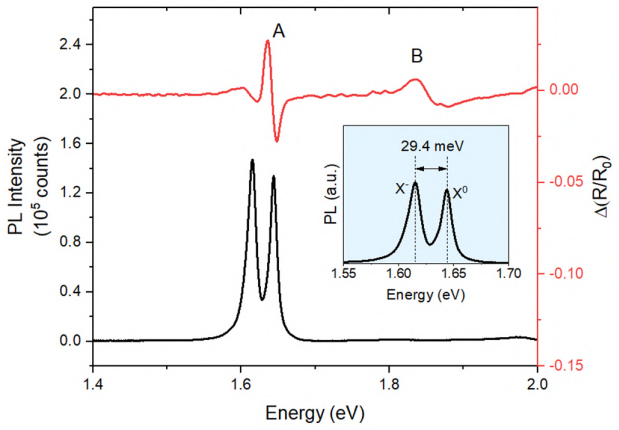

Figure 2.15: Differential reflectance(in red) and photoluminescence (PL) (in black) profiles of a single layer of $MoSe_2$. The differential reflectance identifies both A and B exciton peaks. When excited with a laser at an energy of 2.33 eV (532 nm), the PL reveals the presence of the neutral exciton (X^0) as well as the charged exciton with lower energy (X^-). However, there is no PL evidence for the B exciton. In the inset, the peaks corresponding to the excitons are displayed.

which facilitates the execution of the optical measurements. As shown in Figure 2.14, the setup features a 50x microscope objective manufactured by Mitutoyo Inc.

This objective focuses the laser beam onto the sample, resulting in a spot size with a diameter of approximately 1 µm.

For the excitation of the samples for PL measurements, a CW laser emitting at 532 nm as well as a tunable Ti: Sapphire laser employing an optical parametric oscillator (OPO) was used. The same objective was also employed to collect the emitted PL from the sample. A tungsten halogen lamp is used to collect the reflectance data from the sample.

The emitted PL is then directed to a monochromator, which is coupled with a liquid nitrogen-cooled charge-coupled device (CCD) camera. This arrangement ensures the precise and efficient recording of the emitted light spectra, allowing for further analysis of the optical properties of the samples under investigation. Figure 2.15 shows the differential reflectance spectra of $MoSe_2$ flake taken at 4 K. This shows both the excitonic A and B direct transitions. Both the transitions are manifestations of valence band splitting due to spin-orbit coupling[Coehoorn 1987]. The 203 meV split agrees well with the calculated splitting in the monolayers(180 meV) presented in [Ross 2013]. In the bottom spectra of Figure 2.15 it shows the PL collected from the same sample, showing the exciton (X^0) and trion (X^-)[Kheng 1993] peaks at 1.643 eV and 1.614 eV respectively. The X^- is characterized by a binding energy approximately equal to 30 meV[Ross 2013], which is the energy difference between X^0 and X^-.

Chapter 3

Atomic force microscopy (AFM) ironing of monolayers and heterostacks of TMDCs

Contents

In this chapter, we discuss in detail the post-fabrication technique known as AFM ironing, providing a detailed analysis. We demonstrate how this method enhances the flatness and uniformity of structures compared to the as-prepared samples. Initially, we explore the impact of ironing on the surface morphology of monolayer MoS_2 exfoliated on hBN substrate and encapsulated. Subsequently, we illustrate how this technique can effectively influences the spectral parameters of interlayer excitons in $MoSe_2/MoS_2$ heterostructures.

3.1 An introduction to AFM

Atomic force microscopy (AFM) is a widely used technique used to study the surface of the materials at nanoscale resolution. It allows us to obtain detailed information about the surface topography, mechanical properties and even electrical properties. The main principle behind the working of the AFM is, it measures the forces between

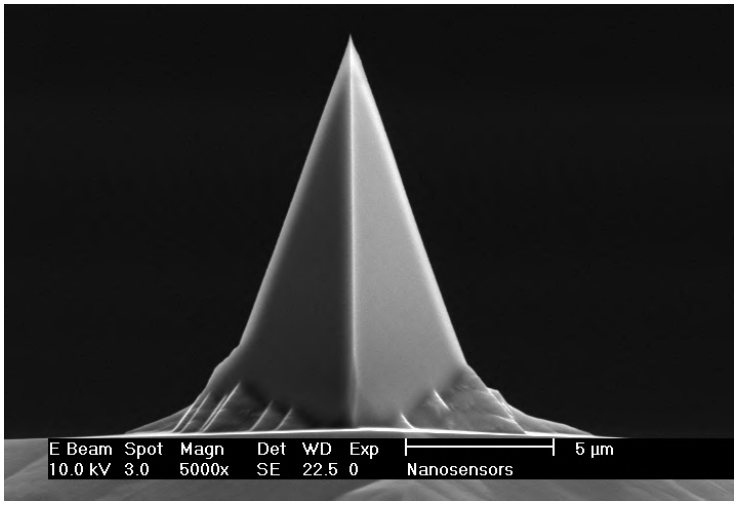

Figure 3.1: SEM image of the PPP FMR AFM tip used for our measurements(adapted from the www.nanosensors.com).

a sharp probe at its tip (whose size is < 10 nm) and the sample surface at a very short distance (0.2-10 nm sample-probe separation). The flexible cantilever on which the probe is supported acts as a sensitive spring. When the AFM tip comes in the vicinity of the surface, it records the small forces between them. The amount of force recorded by the AFM depends on the stiffness of the cantilever (called the force constant) and the distance between the probe and the sample surface. This relation is stated by the Hooke's law [Timoshenko 1959] :

$$F = -k \cdot x \tag{3.1}$$

where F is the force between the probe-sample surface, k is the force constant and x is the cantilever deflection. We used a Point Probe®Plus (PPP) Force Modulation Mode - Reflex Coating (FMR) AFM probe from NanoSensors for our measurements. This probe has a nominal force constant value of 2.8 N/m. Figure 3.1 shows the scanning electron microscope (SEM) image of the probe tip. AFM tips are generally made from Silicon Nitride (Si_3N_4) or Silicon (Si). The probe we use is made from highly doped silicon to dissipate static charge.

3.1.1 Instrumentation behind AFM

To understand the fundamental working principle of Atomic Force Microscopy (AFM), it is essential to examine the instrumentation involved in its operation. Figure 3.2 presents a detailed schematic of the AFM setup, highlighting the key components and their arrangements. The probe's motion across the sample's surface is controlled using a feedback loop and piezoelectric sensors. The deflection of the probe cantilever is monitored by beam bounce method. A semiconductor diode laser is directed towards the back of the cantilever. This laser beam reflects off the cantilever and onto a special sensor called a position-sensitive photodiode detector.

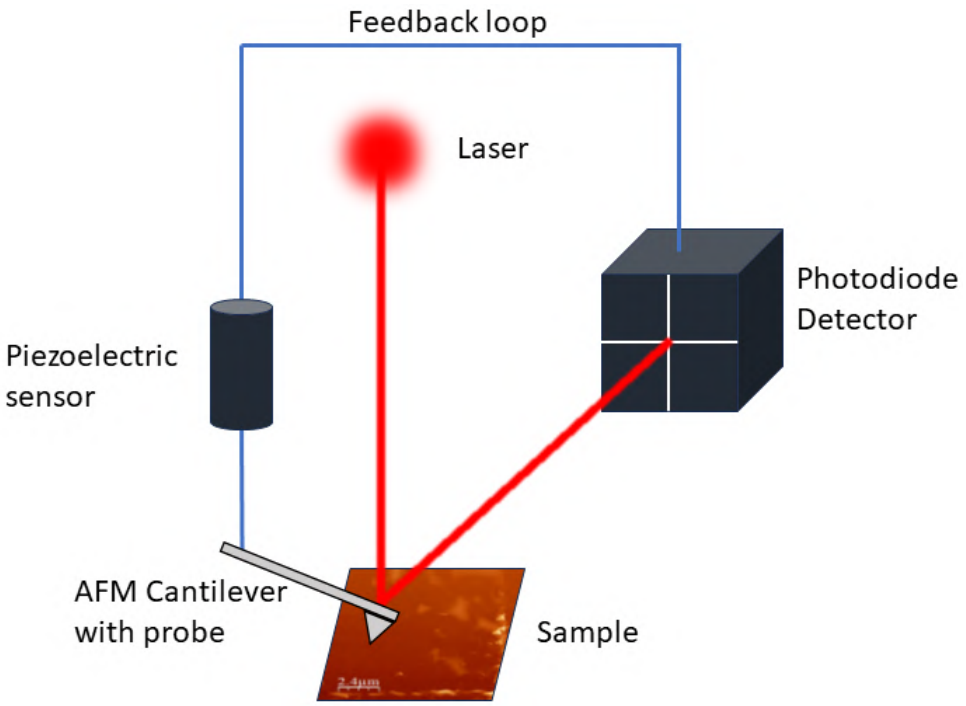

Figure 3.2: Schematics of an AFM instrument showing the "beam bounce" method which uses a photodiode.

As shown in the Figure 3.2, the tip of the cantilever moves across the sample's surface, which causes the cantilever to bend slightly. This bending is picked up by the photodiode detector, which measures how much the cantilever moves. By tracking these movements, the detector creates a map that shows the surface's topography. It's like tracing the ups and downs of a landscape, but on a nanometer scale. This map gives us a detailed picture of the surface morphology. The piezoelectric sensor allows the probe tip (in some AFM setups, the sample can also move) to move in a specific direction based on the feedback and user-inputted parameters such as set point.

3.1.2 Types of imaging methods

As the tip raster-scans the sample surface, the interaction between the AFM tip and the surface arises from various forces. The force of interaction at a short operational distance is the van der Waal (vdW) force. At long-range, capillary, electrostatic and magnetic interactions become significantly governed by Pauli's exclusion principle [Howland 1996, Kinney 1996]. These regimes of different interatomic forces are plotted in Figure 3.3. In the contact mode, the tip experiences a net repulsive vdW force. As the tip moves away as in non-contact mode, it experiences an attractive vdW force. In general, the interaction energy can be described by the Lennard-Jones potential given by:

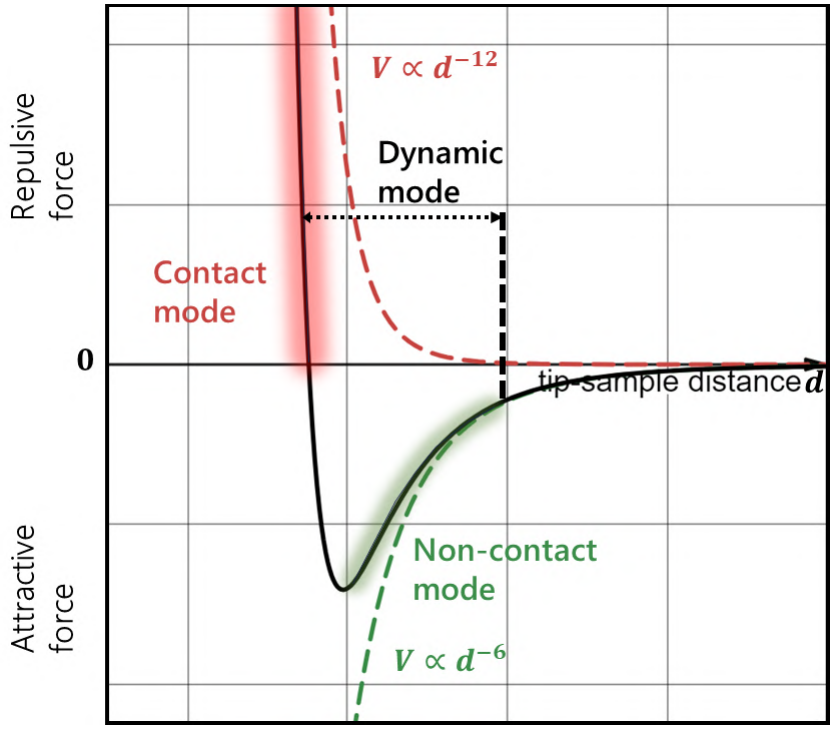

Figure 3.3: Plot of force vs the probe sample separation.

$$V = 4\epsilon \left[\left(\frac{\sigma}{r}\right)^{12} - \left(\frac{\sigma}{r}\right)^{6} \right] \tag{3.2}$$

where ϵ is the potential well depth and σ is the hard sphere radius. σ represents the effective diameter of the particles in the context of the potential, specifically referring to the tip and the surface. In other words, it is the distance at which the repulsive force becomes very strong approximating the behaviour of the hard spheres that cannot overlap. The potential exhibits an attractive tail at larger r but becomes strongly repulsive at shorter distances. In the attractive regime, it reaches a minimum value at about 1.22 σ and in the repulsive regime, it passes through 0 at $r = \sigma$.

Based on the different interaction regimes of this potential, there are three primary imaging modes in AFM:

3.1.2.1 Contact-mode AFM

In contact mode AFM (also referred as repulsive mode), the probe is in direct contact with the sample surface, at a distance of less than a few armstrongs, denoted by the red region in Figure 3.3. This causes the cantilever to bend in response to the topography change due to the repulsive forces. The cantilever maintains constant deflection by adjusting the tip-sample force with the help of a feedback loop. The total force exerted by the tip on the surface is the sum of the cantilever force and

the capillary force, balanced by the repulsive force in contact mode. The magnitude of this total force ranges from 10^{-8} to 10^{-6} N [Howland 1996]. This mode offers advantages such as fast scanning capabilities and suitability for rough samples. However, its reliance on repulsive forces may pose risks of damaging soft samples. Although imaging in liquids can alleviate this concern, it may introduce additional challenges.

3.1.2.2 Dynamic mode AFM (intermittent contact)

In dynamic mode, the cantilever oscillates at its resonant frequency, lightly tapping the sample surface during scanning. However, the probe tip oscillates at a much larger amplitude, typically in the range 20 - 200 nm. The interaction with the sample surface alters the resonance frequency, amplitude and phase angle of the oscillating cantilever. This mode allows for high-resolution imaging of delicate or loosely held samples, making it particularly suitable for biological samples. Nonetheless, operating in liquids can be more complex, and scan speeds tend to be slower compared to contact mode.

3.1.2.3 Non-contact mode AFM

In non-contact AFM, a stiff cantilever vibrates near its resonant frequency, typically between 100 to 400 kHz, with the tip-sample spacing on the order of tens to hundreds of angstroms (as illustrated by the green shade in Figure 3.3). The resonance frequency and amplitude of the oscillating probe decrease as it approaches the sample surface due to interactions mediated by the van der Waals and other long-range forces. These forces act between the probe tip and the sample surface contributing to the overall measurement. These forces are relatively small (approximately 10^{-12} N) compared to the repulsive forces in contact mode. This approach offers the advantage of extremely low force exertion on the sample, leading to a prolonged probe lifetime. However, it generally yields lower-resolution images, and contaminant layers on the surface may interfere with oscillation. Additionally, optimal imaging conditions often require ultra-high vacuum environments.

3.2 Force spectroscopy and force measurement

As discussed in Chapter 2, we employed AFM in both dynamic and contact modes to study the surface morphology of the prepared samples and also to improve the surface homogeneity. In this section, we will discuss in detail the force spectroscopy and understand how to calculate the force and pressure the tip creates at the point of contact on the sample.

In this mode, the operation involves pushing the cantilever probe into the sample and subsequently retracting it. Throughout the process, two key parameters, the height of the z-piezo (z_S) and the deflection (u_C in volts), of the cantilever are continuously monitored and recorded. For example, Figure 3.4 shows an ideal

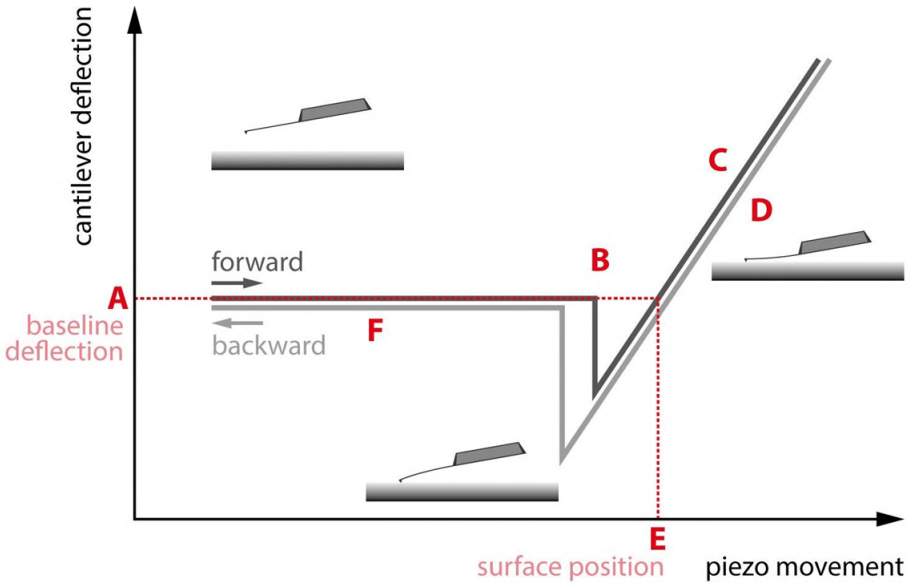

Figure 3.4: Plot of force vs the probe sample separation. (image credits- Nanosurf AG)

dependence of piezo movement vs cantilever deflection plot of an AFM probe. This curve has distinct regions each representing specific stages of the interaction process.

Initially, in region A, the cantilever is positioned above the sample surface indicating the starting point of the approach. As the probe starts to gradually move closer to the surface, it enters region B, where the attractive forces come into play and the initial contact with the sample is established. This contact initiation is typically influenced by various factors such as the capillary forces. Following the contact, the curve transitions into region C, characterised by a sloped region that signifies the interaction forces between the tip and the sample. Here the cantilever applies pressure on the sample surface, pushing into it until a pre-determined deflection or force set-point is reached. After reaching the set-point the withdrawal of the tip from the sample begins, marking the onset of region D. During the withdrawal phase in region E, a notable phenomenon known as sticking may occur, where the tip adheres to the sample surface. This adherence results in a significant adhesive dip in the curve, indicating strong interactions between the tip and the sample. Finally, as the withdrawal continues, the tip eventually disengages from the surface, leading to the complete withdrawal denoted by region F. This observed hysteresis between the approach and the withdrawal curves further emphasizes the non-linear relationship between the tip's motion towards and away from the sample, offering additional information about the sample's surface characteristics such as adhesion, roughness and mechanical properties.

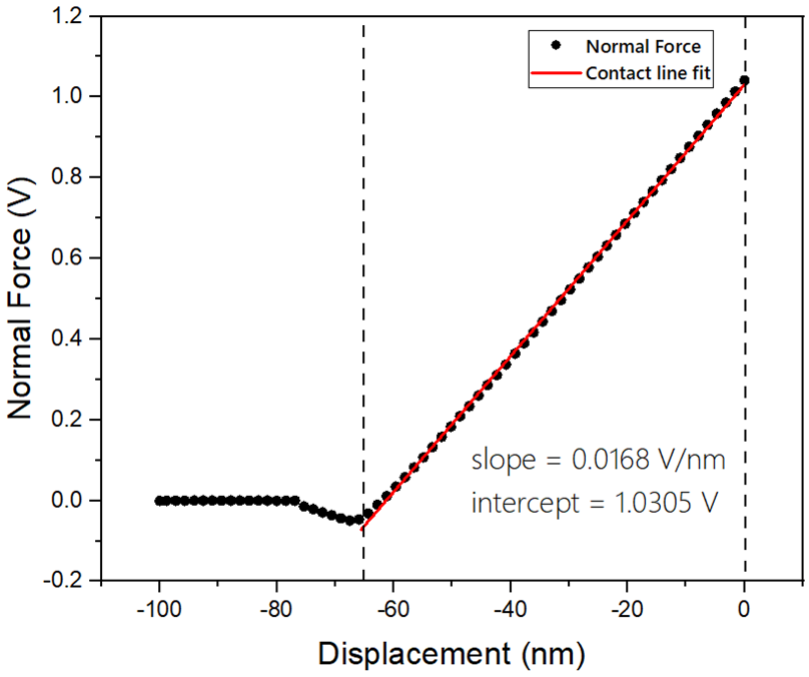

Figure 3.5: Exemplary force-displacement plot (only approach plot has been shown) of the AFM probe used for our measurements.

3.2.1 Calculation of the force from F-z curve

The F-z data thus obtained from the AFM force spectroscopy measurement includes the z-piezo height z_S and the cantilever deflection u_C, typically measured in volts (V). Since the cantilever is treated as a linear spring load system, it is feasible to convert the cantilever deflection u_C into an equivalent force.

As shown in Figure 3.5, this graph primarily reflects the cantilever's deflection behaviour relative to the z-piezo's movement. The linear relationship can be used to determine a material constant of the cantilever called the sensitivity denoted by s and given by:

$$s = -\frac{1}{slope} = -\frac{\Delta z_S}{\Delta u_C} \tag{3.3}$$

where, $[s] = \frac{nm}{V}$, Δz_S and Δu_C are changes in z-piezo height and change in cantilever deflection respectively. Once this constant is known, we can easily convert the cantilever deflection u_C into a corresponding length value as,

$$z_C = s u_C \tag{3.4}$$

In the linear-elastic bending range of the cantilever, Hooke's law applies, relating the deflection z_C to the applied force F through the cantilever's spring constant k:

$$F = -k \cdot z_C$$

For example, in Figure 3.4, we show the F-z curve of the AFM probe which was primarily used to conduct our measurements. Once we have corrected the offset, we fit the linear dependence of the z-piezo or the displacement (in nm) and Normal force (in V). This gives us the sensitivity of the cantilever (the slope) as 0.0167 V/nm and a cantilever deflection (the intercept) of 1.0305 V. To estimate the cantilever's spring constant, k, either, one can use the value provided on the vendor's datasheet or this can also be calculated by vibrating it in the resonance frequency. We used the value of 2.8 N/m provided in the datasheet for this probe for our purpose. This yielded a value of force (F)$\sim$ 171.6 nN.

3.2.2 Calculation of pressure generated by the AFM tip

To get a rough estimation of the applied pressure, we used the Hertz model[Johnson 1987]. The tip-sample system is conceptualised as a sphere-plane scenario, wherein the contact radius (ρ) between a sphere and a plane is precisely defined by the following equation,

$$\rho = \left(\frac{3FR}{4E^*}\right)^{\frac{1}{3}} \tag{3.5}$$

where F is the applied force, R is the tip radius and E^* is the effective elastic modulus given by,

$$\frac{1}{E^*} = \frac{1}{E_{tip}} + \frac{1}{E_{sample}} \tag{3.6}$$

The mean contact pressure P exerted on the sample by the tip was determined as,

$$P = \frac{1}{\pi}\left(\frac{4E^*}{3}\right)^{\frac{2}{3}}\left(\frac{F}{R^2}\right)^{\frac{1}{3}} \tag{3.7}$$

E_{tip} is 150 GPa for the silicon cantilever. The elastic modulus of the sample was approximated as the elastic moduli value found for the atomically thin hBN, i.e. 850 GPa [Falin 2017]. The primary source of uncertainty stems from the tip radius (R). While nominal values are typically below 10 nm, they tend to increase during scanning in contact mode. For pressure estimation purposes, a value of 20 nm has been employed. With these parameters, the applied pressures within the force range of 5 nN to 400 nN varied between 2.2 GPa and 9.8 GPa.

3.3 AFM ironing of MoS_2 monolayer

To understand the effect of AFM ironing on surface morphology, we began with a monolayer of MoS_2 exfoliated on an hBN substrate (170 nm thick, as determined by AFM). Only a portion of the monolayer was capped with thin hBN (9 nm thick), as shown in Figure 3.6. The sample comprises two distinct regions: the capped region, covered with hexagonal boron nitride (hBN), and the uncapped

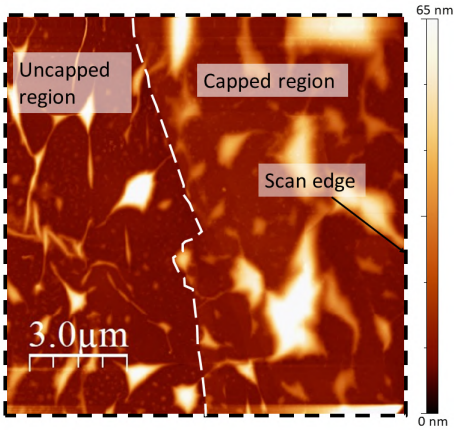

Figure 3.6: AFM topography scan of the prepared MoS_2 sample. The blue dashed line separates the capped and uncapped regions of the sample. The edge of the planned scan area is shown in the dynamic scan image.

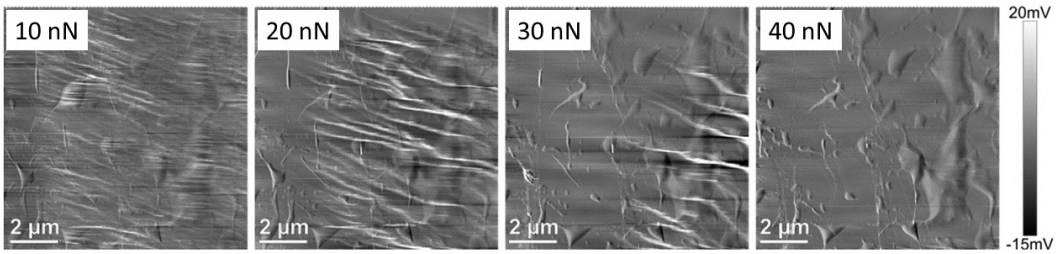

Figure 3.7: Lateral force images obtained during the ironing process in contact mode reveal a distinct trail left by displaced surface adsorbates at low forces. This trail is prominently visible in friction images but diminishes noticeably for forces exceeding 30nN.

region, which remains as an uncovered MoS_2 monolayer. The blue dashed line shows the edge of the top hBN, which separates the capped and uncapped region of the sample. In Figure 3.6, we can already notice a large number of bubbles and wrinkles, which are the result of the stamping during the fabrication process [Gasparutti 2020, Rosenberger 2018, Chen 2021]. The AFM ironing was planned on the area shown in Figure 3.6 on an area of 10 µm by 10 µm in contact mode in steps of ∼10 nN from 5 nN to 400 nN. Dynamic AFM scan was conducted on an area of 12 µm by 12 µm after each contact mode scan to verify the effect of scanning in contact mode, which will be discussed in the following sections.

3.3.1 Identification of ironing force regimes and surface alterations

As we discussed in the previous section, we performed the ironing in a 10 µm by 10 µm area of the MoS_2 sample. During the ironing process, we identified three distinct force regimes by examining their impact on surface structures and roughness. The

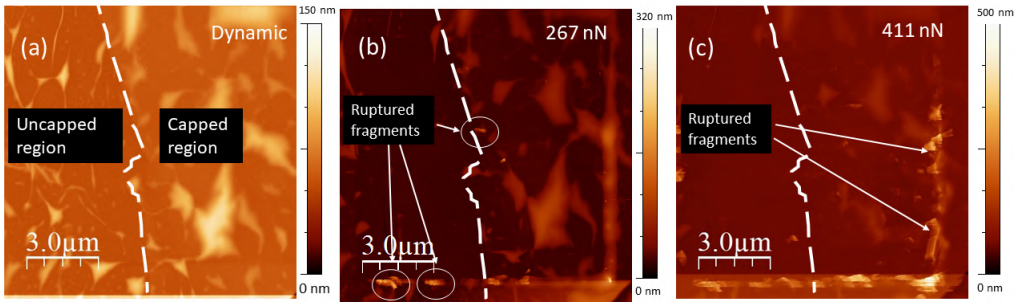

Figure 3.8: (a) Shows the initial dynamic scan which unravels the bubbles and wrinkles present. (b) Shows a scan at $\sim$ 267 nN, which starts showing pieces of ruptured pieces of flakes on the edges. (c) Shows the final scan at $\sim$ 411 nN with ruptured surface features and damaged top layer.

friction images in Figure 3.7(a-b) reveal that in the low force regime, typically under 20 nN, debris and surface adsorbates accumulate initially, forming ripple-like patterns parallel to the scan direction. These patterns result from the clustering of surface debris and adsorbates. As we moved higher up the force, we observed that these patterns started to diminish when forces exceeded 30 nN, as can be seen in Figure 3.7(c-d), denoted as the high force regime.

Moving even higher in the force, denoted as the 'intense' force regime (beyond 200 nN) on the same area as shown in Figure 3.8(a), the AFM tip starts to damage the top layer as shown in Figure 3.8(b). In Figure 3.8(c), scanned at about 411 nN of ironing force, we can see that the top layers' ruptured fragments start accumulating on the edge of the scan area. From Figure 3.8(c), it can be concluded that the damage was not only to the bubbles but also to the entirety of the top layers, thereby damaging the heterostructure. These observations allowed us to estimate the threshold for the magnitude of the ironing force and are in agreement with previous studies [Kim 2019].

3.3.2 Effects and implications of ironing on surface and bubbles

To better understand the impact of ironing forces on surface characteristics, we examined the scan area in detail. At low forces, specifically under 30 nN, surface features such as bubbles and wrinkles appeared largely unchanged in terms of numbers, shape, and size. This is evident when comparing the AFM dynamic scans in Figure 3.9(a, b). It is only when the applied force is higher than 30 nN that there is a noticeable change in these defects, as indicated in Figure 3.9(c). As one would expect this effect is more pronounced on uncapped regions of MoS_2 where the absence of a protective hBN layer allows for easier removal of such defects. This aligns with previous research, suggesting that the hBN layer marginally raises the critical force necessary to displace underlying bubbles using an AFM tip [Gasparutti 2020, Chen 2021, Kim 2019]. Notably, bubbles exceeding 1 µm in diameter show minimal to no change, even at forces within the µN range [Kim 2019].

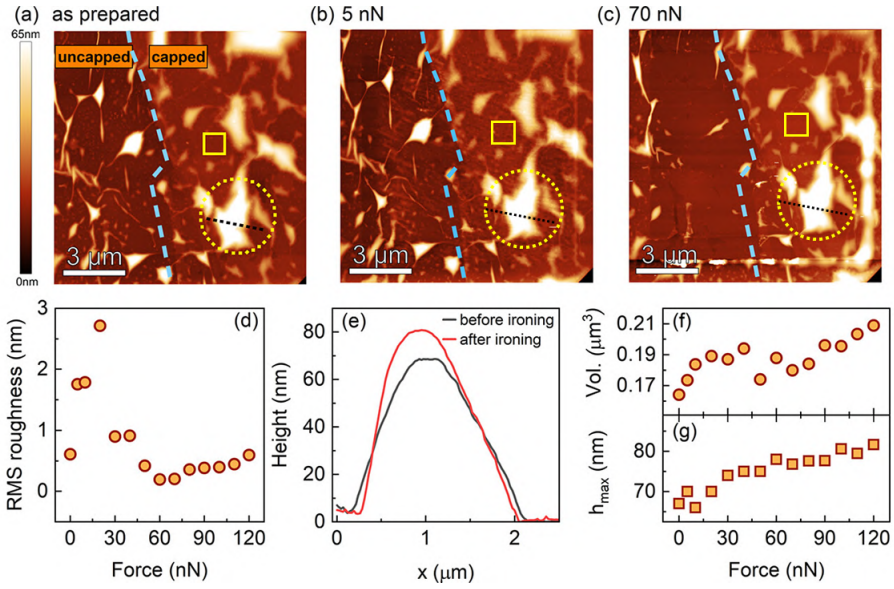

Figure 3.9: (a-c)Shows AFM images before and after ironing with different forces. Panel (d) displays the change in root mean squared (RMS) surface roughness with ironing forces (inside the $1\mu m^2$ yellow square). (e) Shows a bubble's (inside the yellow circle) height profile before and after ironing. Panels (f) and (g) show bubble volume and height as the ironing force varies.

The clustering phenomenon, discussed previously in section 3.3.1, contributes to an increase in surface roughness, as shown in Figure 3.9(d). Although AFM ironing did not eliminate the larger bubbles, their shape and size underwent significant change. This is illustrated in Figure 3.9(e), which compares the profiles of a particular bubble before and after the AFM ironing procedure, highlighting notable shape transformation. Furthermore, the changes in height and volume of the bubbles in response to varying ironing forces are quantitatively presented in Figures 3.9(f) and (g). We notice that when the bubbles on the capped heterostack are subjected to ironing, their height and volume increase noticeably. This phenomenon occurs because the smaller bubbles are displaced and merged with the larger ones during the process. As a result, any minor irregularities and corrugations at the interface between the layers especially in the space between the bubbles are flattened out.

To further substantiate the observed trend in the changing volume and height of the bubbles, indicating that this change was not an isolated incident, we conducted a study examining alterations in other bubbles of substantial sizes nearby. As shown in Figure 3.10, our findings were corroborated by the trends exhibited by these additional bubbles. This flattening action improves the overall contact between the layers particularly in the areas where the smallest bubbles have been removed.

To substantiate these observations, we have conducted an examination of three different $MoS_2/MoSe_2$ heterostructures. These structures comprise monolayers of MoS_2 and $MoSe_2$ sandwiched between the hBN layers. The structural parameters

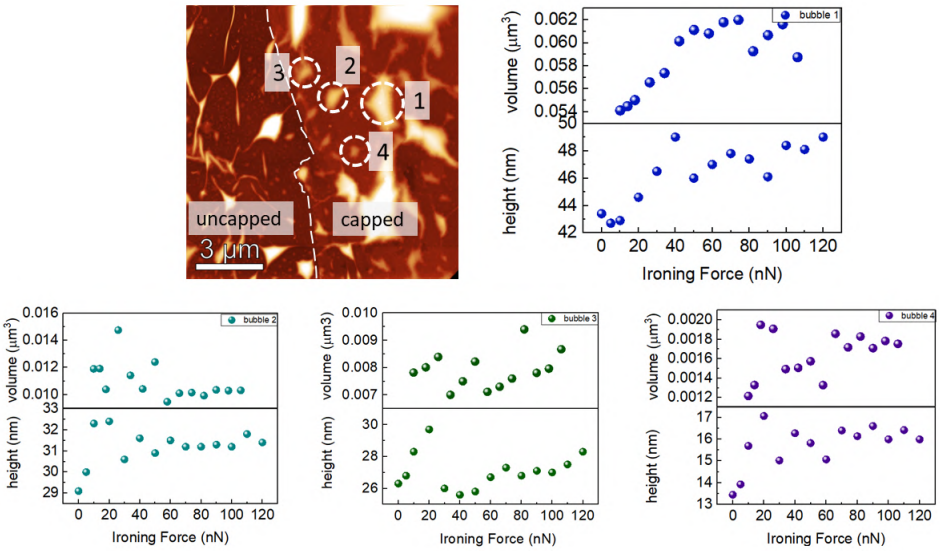

Figure 3.10: The AFM topography image depicts both capped (protected) and uncapped (unprotected) regions. Through height and volume analysis of the selected bubbles highlighted within the circles, formed specifically in the capped regions, a distinctive trend emerged.

are presented in Table 2.1 of Chapter 2. As we will see in the upcoming section 3.4, this is crucial for the performance of heterostructures, as improved layer contact directly correlates with enhanced optical and electronic properties. This improvement is akin to the enhanced transport characteristics observed in the previous studies[Kim 2019].

3.4 AFM ironing of $MoS_2/MoSe_2$ heterstructures

This section focuses on the heterostructures shown in Figure 3.11, henceforth referred to as Sample A (a), Sample B (b), and Sample C (c). Each sample features an encapsulated heterostructure region, highlighted by a black dashed line, which serves as our primary area of interest. As was discussed in Chapter 1, a heterostructure is formed by stacking two or more layers of different two-dimensional (2D) materials, which in our case is $MoSe_2$ and MoS_2, resulting in unique electronic and optical properties due to the interaction between the layers. The monolayers of $MoSe_2$ and MoS_2 are denoted by green and red solid lines, respectively. The samples and subsequent analysis of the optical response have been discussed and categorised based on their stacking orientation.

As presented in Table 3.1, samples A and B are fabricated with near 60^0 twist (H-type) stacking, whereas sample C is fabricated with near 0^0 twist (R-type) stacking. To reintroduce the samples, Table 3.1 details the twist angles and the corresponding ironing forces employed for each sample.

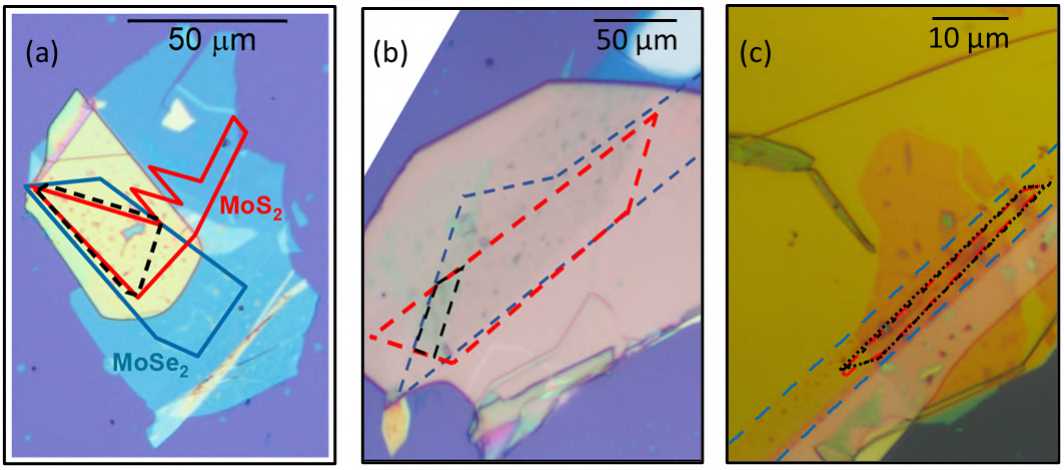

Figure 3.11: (a) Sample A (b) Sample B (c) Sample C. The red and blue outline denotes the MoS_2 and $MoSe_2$ monolayers respectively. The black dashed line represents the heterostructure region.

Sample	Twist angle	Ironing Forces
Sample A	57.2 (H-type)	30, 60, 80 nN
Sample B	56.3 (H-type)	70 nN
Sample C	1.3 (R-Type)	10, 100 nN

Table 3.1: Samples, their twist angles, and corresponding ironing forces.

3.4.1 AFM ironing of sample A and B (H-type)

3.4.1.1 Ironing process and surface modifications

The ironing process was conducted to improve the surface uniformity and quality of the heterostructures. By applying controlled forces with an AFM tip, we aimed to achieve a flatter and more homogeneous interface. This section details the AFM ironing experiments on samples A and B, both of which feature H-type stacking and describe the resultant surface modifications.

Figure 3.12 presents the AFM topography scans of sample A, highlighting three square-shaped areas ironed with pressing forces of 30, 60, and 80 nN, applied using an AFM tip in contact mode. Similarly, as shown in Figure 3.13(a), an ironing force of 70 nN was employed on sample B. The selected area spans a region half-capped with top hBN. These ironing forces generated an estimated pressure of approximately 4–6 GPa, calculated using Equation 3.7 presented in Section 3.2.2.

Consistent with our previous observations of the MoS_2 monolayer discussed in Section 3.3, the area scanned in contact mode on samples A and B, demonstrates the removal of surface debris and adsorbates. The debris accumulates at the edge of the scanned area, as shown in Figure 3.13(b-c). The ironing process significantly enhances the flatness of the heterostructure, as evidenced by the close-up views of

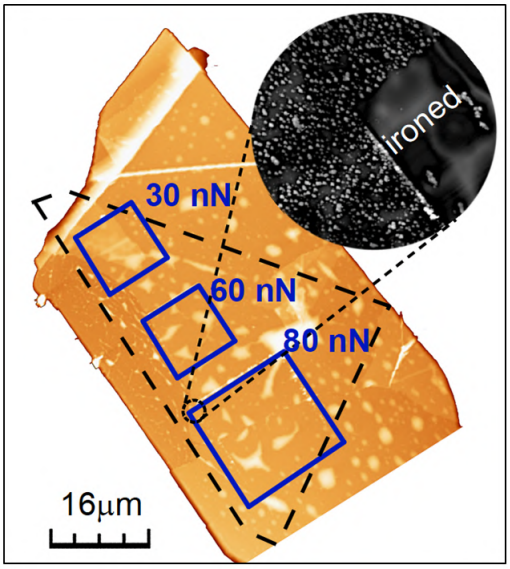

Figure 3.12: Topographic AFM scan in dynamic mode of sample A showcases regions subjected to varying ironing forces, with a close-up view of the ironed area (80 nN) provided in the inset.

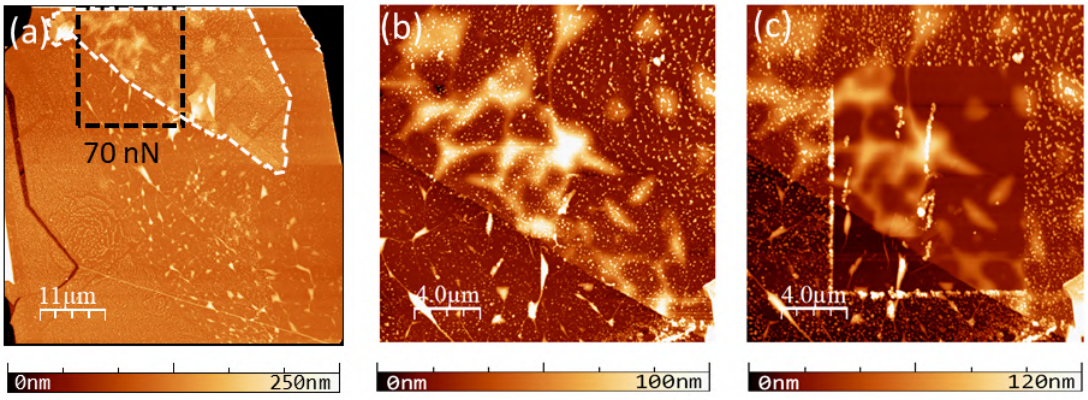

Figure 3.13: (a) Illustrates the AFM topography of the selected heterostructure area before contact mode scanning. The white dashed line denotes the top hBN layer. (b,c) Shows the region pre and post-ironing, highlighting debris accumulation at the edges under a scanning force of 70 nN.

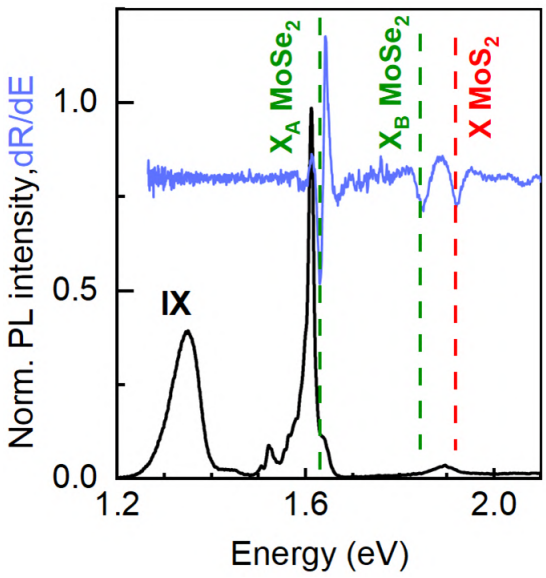

Figure 3.14: Photoluminescence (in black) and reflectance spectra (in grey) acquired at 4.5 K from the heterostructure region are shown, highlighting interlayer (IX) and intralayer exciton resonances, as indicated.

the ironed areas in the insets of Figures 3.12 and Figure 3.13(b-c). In the following section, we will examine the implications of ironing on the optical behaviour of the sample at low temperatures.

3.4.1.2 Photoluminescence intensity and lineshape alterations

The heterostructure regions on samples A and B are shown in Figures 3.11(a) and 3.11(b), with the areas indicated by black dashed lines. Both $MoSe_2$ and MoS_2 constituents exhibit distinct optical responses within this region. Figure 3.14 shows a typical low-temperature (T=4.5 K) photoluminescence (PL) spectrum obtained from this heterostructure region. Within this spectrum, distinct features associated with $MoSe_2$ and MoS_2 intralayer excitons are observable at approximately 1.62 eV and 1.9 eV, respectively[Shree 2018, Cadiz 2017]. These transitions are also evident in the reflectance spectrum of the heterostructure (as shown by the grey spectra in Figure 3.14), alongside an additional feature corresponding to the $MoSe_2$ B-exciton transition[Ross 2013]. Additionally, a notable PL peak, exclusively observed in the heterostructure region, corresponds to the interlayer exciton (IX)[Baranowski 2017, Zhang 2018, Mouri 2017, Surrente 2018].

The spectra analysis was conducted using integration techniques. Various parameters, including the emission energy (x at y_{max}), linewidth (full-width at half-maximum), and integrated intensity (area under the curve), were derived from the integration of the IX spectra. An exemplary IX spectrum is presented in Figure 3.15. This figure illustrates the parameters obtained through integration, which were subsequently utilized in the spectral analysis.

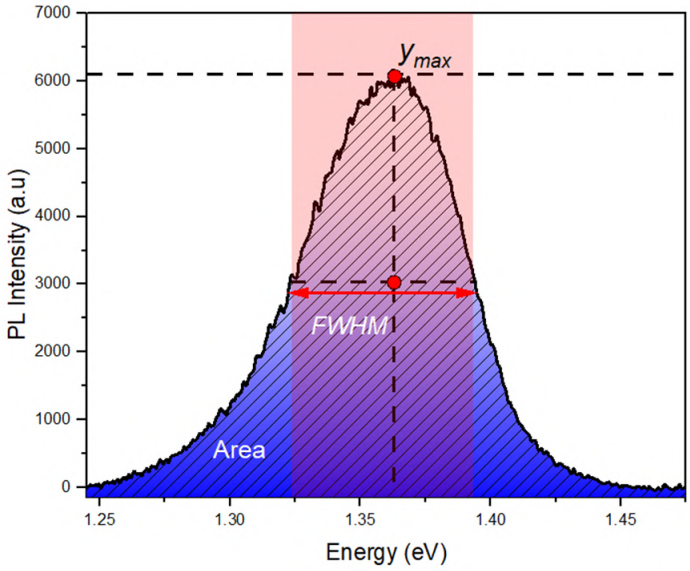

Figure 3.15: Representative interlayer exciton spectra. Spectral analysis was performed using integration. Parameters like the maximum intensity (y_{max}), full-width at half-maximum (FWHM), and area under the curve are calculated from the operation.

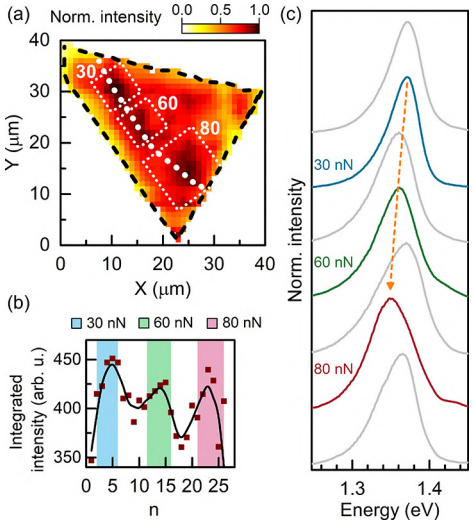

Figure 3.16: (a) The PL intensity map for the IX reveals higher intensity hotspots within the ironed regions.(b) The evolution of PL intensity along the cross-section is illustrated by the white dashed line. A distinct enhancement of PL intensity is evident in the ironed part, as indicated by the shaded area. (c) Representative PL spectra along the cross-section demonstrate the change in PL lineshape within the ironed part. Grey spectra correspond to the non-ironed region along the cross-section direction. Reused from [Palai 2023] with permission

The spatial distribution of the integrated intensity of the IX photoluminescence (PL) within the heterostructure area of sample A is presented in Figure 3.16(a). Notably, within the ironed regions demarcated by white squares, there is an enhancement in PL intensity compared to the non-ironed sections of the heterostructure. This enhancement becomes particularly pronounced when examining a cross-section across all three ironed regions along the white dotted line, as depicted in Figure 3.16(b). The integrated PL intensity demonstrates local maxima within the ironed regions (shaded areas), whereas between these regions, the intensity of the peak decreases.

In addition to the enhanced intensity, there are observable shifts and spectral broadening of the interlayer transition with increasing ironing force. Furthermore, the lineshape of the PL spectra changes. As can be seen in the plot of Figure 3.16(c), spectra from non-ironed sections exhibit a low-energy tail, whereas, in the ironed sections, the lineshape becomes more symmetric with increasing ironing force. For the highest forces applied, a new feature emerges on the high-energy side, as demonstrated by the representative spectra in Figure 3.17 (e) (presented by the red and black spectra) taken along the cross-section are displayed.

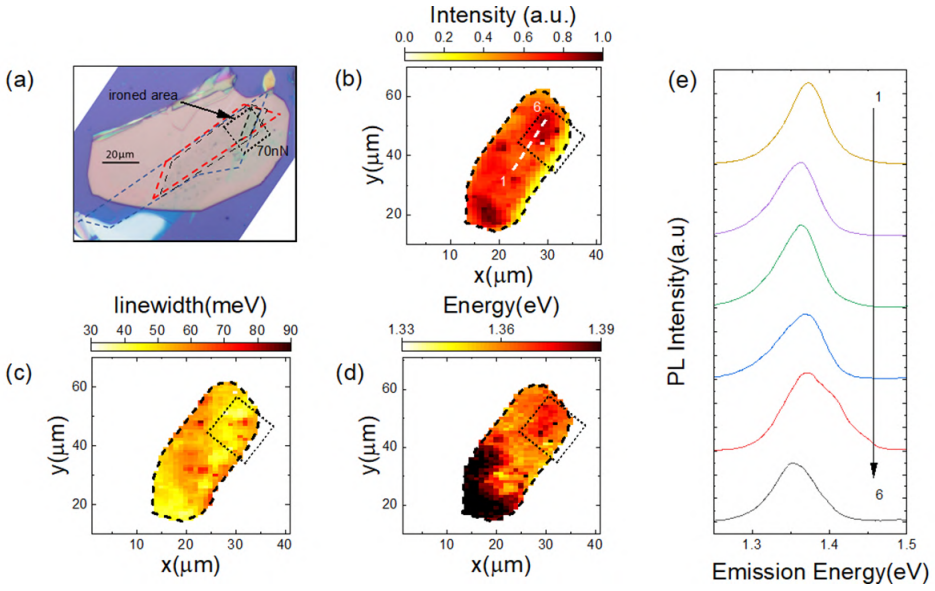

Figure 3.17: (a) Microscope image of sample B demarcating the ironing region with black dashed line. Heatmaps showing the distribution of (b) integrated intensity (c)linewidth (d) peak energy of the IX emission from the heterostructure area. (e) The spectral stack shows how the spectra shape changes along the white dashed line in (b).

Similarly, to understand the effect of ironing on the optical properties of sample B, we conducted low-temperature (4K) photoluminescence (PL) mapping of the sample. The emission spectra were integrated in the IX energy range of 1.25 to 1.45 eV as presented in Figure 3.17, offering insights into various emission parameters

associated with the IX, post-ironing. Figure 3.17(a) shows the microscope image of the sample denoting the area where the ironing was conducted at F=70 nN of force. Figure 3.17(b-d), shows how different emission parameters vary across the sample. Upon examining these maps, we realised the sample was spatially inhomogeneous in the non-ironed regions as well as in ironed regions due to the presence of large-sized bubbles on this sample particularly. This inhomogeneous distribution significantly complicates the analysis. In the next section, we present a statistical analysis of the spectral parameters of the IX spectra observed in samples A and B.

3.4.1.3 Statistical analysis of the photoluminescence spectra

To validate these observations made in the previous section 3.4.1.2 and gain deeper insights into the evolution of IX characteristics, we conducted a statistical analysis of the PL spectrum measured at various spots on the heterostructure of both samples A and B. The histograms presented in Figure 3.18(a-i) illustrate the distribution of the PL peak energy, linewidth, and intensity for different forces utilized during the ironing process. Notably, ironing induces a redshift in the IX transition, as can be seen in Figure 3.18(a,b,c). This redshift appears to be roughly proportional to the applied ironing force, with a coefficient of -286 ± 225 μeV/nN derived from the fit in the Figure 3.19(a).

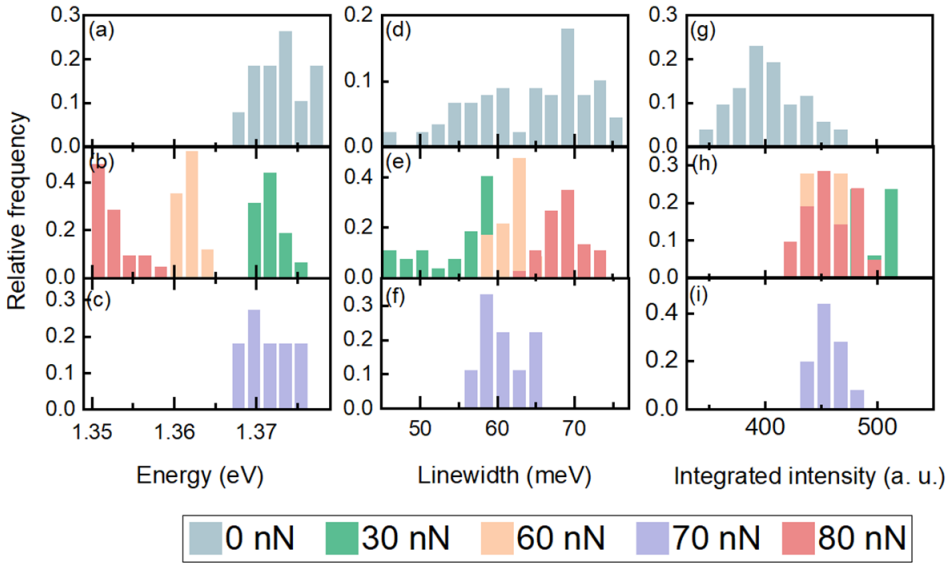

Figure 3.18: Histograms showing the distribution of (a-c)PL energy, (d-f)line width, and (g-i)intensity for both non-ironed and ironed regions within the heterostructure of sample A (30, 60 and 80 nN) and sample B (70 nN).

In Figure 3.18(d-f), the distribution of the linewidth of the IX spectra is presented. Notably, the average broadening of the emission line increases with a coefficient of 0.26 ± 0.07 μeV/nN, as shown in Figure 3.19(b). The error bars in the plots represent the variability in the spectral parameters derived from the mea-

surements taken at different points on the sample. This uncertainty arises mostly from the sample inhomogeneity. However, the distribution narrows post-ironing, as evidenced by the histograms in Figure 3.18(d-f).

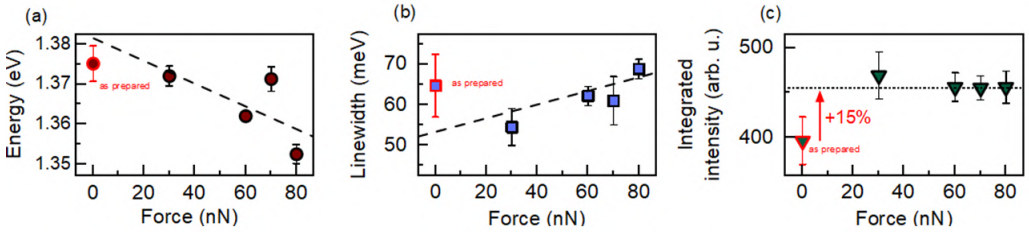

Figure 3.19: The plots illustrate the average values of IX (a)transition energy, (b) line width, and (c) PL intensity plotted against the ironing force. The dashed lines indicate the linear fits in (a-b).

The histograms of the integrated intensity, shown in Figure 3.18(g-i), reveal that the PL intensity in the ironed regions shows an average increase of about 15% compared to non-ironed areas (as shown in Figure 3.19(c)). These outcomes are consistent with the notion of more intimate contact between the layers within the heterostructures, stemming from the reduced density of bubbles following the AFM treatment. Further insights into the underlying physics of these observations are discussed in detail in Section 3.4.3.

3.4.2 Ironing process and surface modification of sample C (R-Type)

In this section, we employed AFM ironing to examine a heterostructure, focusing specifically on areas subjected to ironing forces of 10 nN and 100 nN, similar to the approach used in the previous section. Figure 3.20(a) captures the areas (in a white dashed square) scanned after applying these forces, where we observed an accumulation of debris along the edge. A closer look revealed a clear distinction between the two areas based on the applied force. The region subjected to the higher force of 100 nN was distinctly visible, in contrast to the less visible area where only 10 nN was applied.

Further insights were gained from the phase contrast scan shown in Figure 3.20 (b), where we take a look at the phase contrast scan of the same area. A phase contrast for the 100 nN scan area was visible. No such phase shift was observed in the area ironed with 10 nN. Within the heterostructure area, we identified a specific area marked by a white dashed line in Figure 3.20(b), which exhibited a phase contrast. The underlying reasons for this contrast and the specific factors contributing to the change in phase in this particular area remain unknown.

3.4.2.1 Statistical analysis of photoluminescence spectra

To understand the effect of ironing on the optical response of the heterostructure (illustrated in Figure 3.21(a)), we captured the photoluminescence (PL) map at

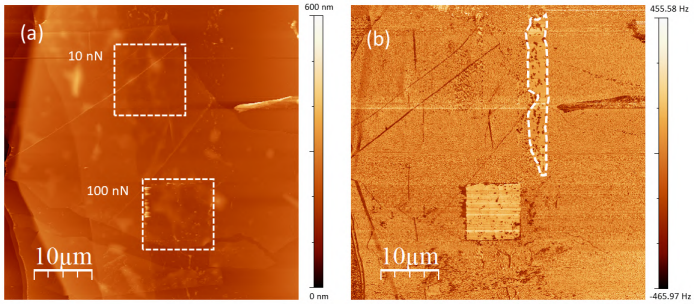

Figure 3.20: (a) AFM topography image showing the scan areas with 10 nN and 100 nN. (b) AFM phase scan showing the change in the phase of the tip of the surface of the sample.

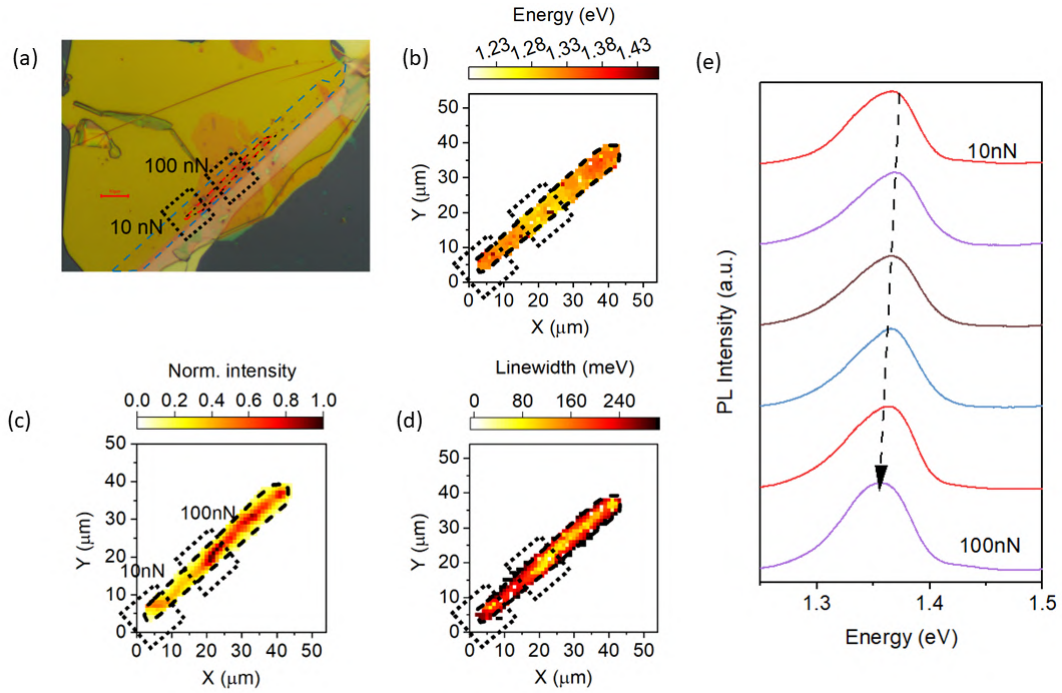

Figure 3.21: (a) A micrograph of sample C, (b) energy, normalized intensity maps of (c) intensity, (d) line width, and (e) Photoluminescence (PL) spectrum obtained from the sample .

4K, as shown in Figure 3.21(c). Here, we integrated the spectra in the IX energy range (1.25-1.45 eV). We observed an increased intensity at the spot of the 100 nN scanned area, which was accompanied by changes in the linewidth and energy of the IX emission peak in this area as shown in Figure 3.21(c-e).

Further insights emerged from a statistical analysis of the spectra collected from the areas scanned with 10 nN and 100 nN forces. As shown in Figure 3.22(a), the histogram shows the distribution of the IX peak energy in different scanned areas

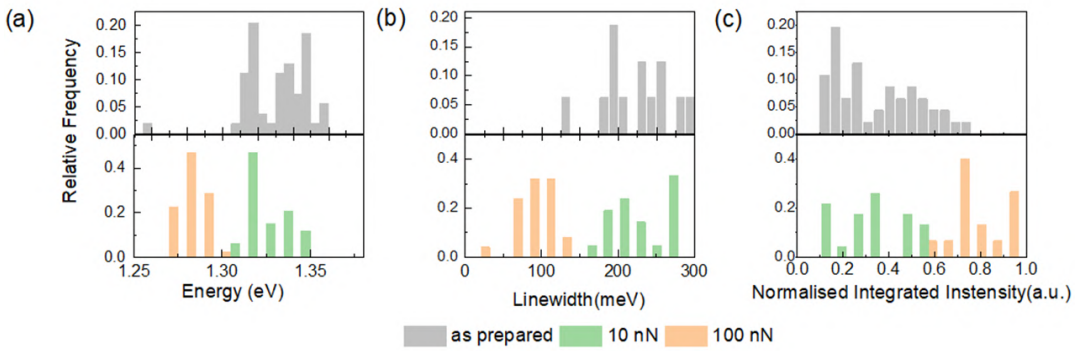

Figure 3.22: (a-c) Histograms showing the statistical distribution of PL energy, linewidth and normalised integrated intensity as prepared(on top) versus ironed (in the bottom panel).

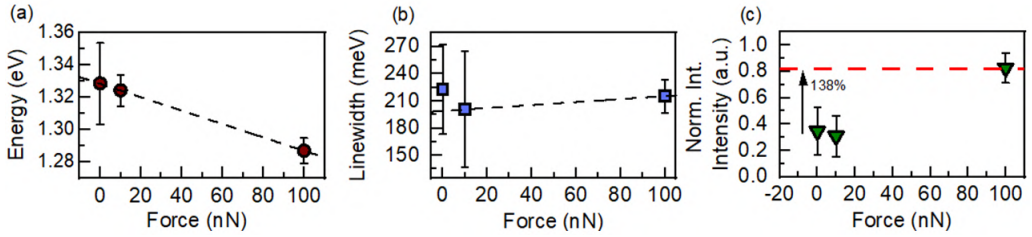

Figure 3.23: Mean values of IX (a)energy, (b)linewidth and (c) normalised integrated intensity. Notably, the fitting procedure in panels (a) and (b) excludes the 0 nN data point, corresponding to the as-prepared heterostructure, as it is beyond our control.

compared to the non-ironed or as-prepared areas. There was a noticeable red shift in the peak energy from the histograms, and in Figure 3.23(a), this shift is quantified with a coefficient of 420 µeV/nN. Similar to the previous samples A and B, the error bars originate from the spot-to-spot inhomogeneity the sample possesses to our experiment and analysis.

The standard deviation of the peak energy decreased in the ironed regions, indicating narrower distributions, as shown in Figure 3.23(a). Similarly, we observed a decreased standard deviation for the linewidth and a reduction in the linewidth itself compared to the as-prepared sample area, as illustrated in the histogram plot in Figure 3.22(b) and the plot in Figure 3.23(b), with a shift coefficient of 0.166 meV/nN. Moreover, there was a significant increase (about 138%) in the intensity of the IX peak, as evidenced by the histograms in Figure 3.22(c) and Figure 3.23(c).

In addition to these findings, our in-depth analysis concludes that the 10 nN ironing force has minimal impact. This was evident in both the AFM topography and phase scans and is further substantiated by the optical data in the histograms in Figure 3.22 and the corresponding plots in Figure 3.23.

3.4.3 Insights from the ironing of the three samples

3.4.3.1 Surface roughness modifications

In our study, we observed a noticeable decrease in the surface RMS roughness of the ironed areas, as depicted in Figure 3.24(a). This reduction in roughness, coupled with a lower density of bubbles and wrinkles, has a substantial impact on the uniformity of optical properties.

Furthermore, the increase in RMS in the 10 nN scan area (refer Figure 3.24(a)) aligns with the heightened RMS observed in our previous observation of the MoS_2 monolayer under low regime forces, as discussed in Section 3.3. This finding emphasizes the crucial role of minimizing interface roughness in achieving more consistent and uniform optical spectra across the heterostructure.

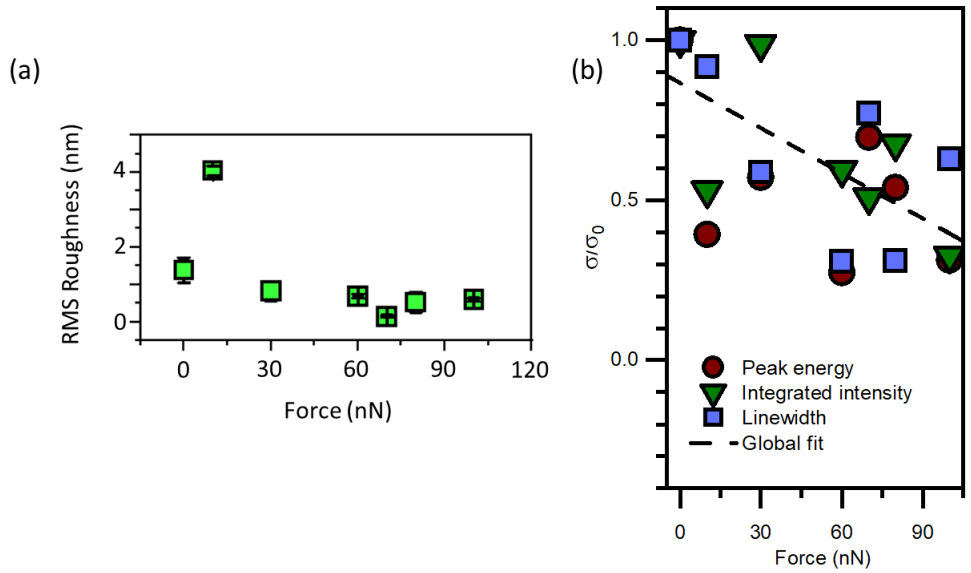

Figure 3.24: (a) Plot shows the change in RMS value averaged over a $1nm^2$ area within the ironed area. (b) Plot shows the standard deviation (σ) of the IX transition energy, line width, and PL intensity normalized to the standard deviation measured on non-ironed areas (σ_0) as a function of the ironing force derived from the three different samples discussed. The dashed line represents the global linear fit of the relative standard deviation of all parameters.

3.4.3.2 Modulating optical properties

As we discussed in Sections 3.4.1.3 and 3.4.2.1, the ironing process is not just limited to surface modifications but also has strong implications on the optical properties of these heterostructures. Most importantly, after the ironing process, there is a significant decrease in the standard deviation of these spectral parameters (i.e. IX energy, linewidth, and intensity) as shown in Figure 3.24(b). This decrease, representing a more uniform distribution, correlates with the reduced roughness and

defect density. This plot highlights how the standard deviation of these parameters in the ironed areas, normalized to their values in non-ironed areas (σ_0), varies as a function of the applied ironing forces. This process results in a pronounced narrowing in the distribution of IX energy, linewidth, and intensity—quantified as a 50% decrease in the ratio σ/σ_0, as plotted in Figure 3.24(b). In a $MoS_2/MoSe_2$ heterostructure, the IX transition is a strongly hybridized, momentum-indirect exciton[Su 2016, Sokołowski 2023]. The ground exciton transition is between $K-\Gamma$ points, as reported in [Su 2016]. It is expected that the $K-\Gamma$ transition oscillator strength results from the interplay of the layer distance depending on the Γ states' hybridisation and e^- and h^+ separation. The IX's indirect nature and the added spatial separation of e^- and h^+ result in an oscillator strength that is too weak to be detected in the reflective contrast (RC) spectra. This momentum-indirect dark state can be observed in the PL spectra due to its high occupation as the lowest energy state[Sokołowski 2023]. The indirect nature further adds difficulty in establishing a direct correlation and making the quantitative analysis of the impact of interlayer distance on the optical properties.

The observed alterations in the spectral properties of IX emission following ironing, align with the enhancement of moiré effects, as suggested by previous studies [Tran 2019, Wu 2018, Yu 2017a]. For a detailed discussion on moiré effects, the reader is referred to Section 1.5.1.1. It is worth noting that the implications of the ironing procedure extend beyond mere proximity enhancement. It is conceivable that this procedure also mitigates local strain fluctuations, thereby augmenting the moiré effect. This enhancement arises from the improved proximity of the layers and the resultant flattening.

The redshift observed in the IX transition post-ironing is attributed to the increased binding energy of IXs and/or band hybridization, facilitated by a reduction in interlayer distance [Brem 2020]. Additionally, the improved layer proximity, coupled with local flattening, deepens the moiré trapping potential, further contributing to the redshift of the IX[Tran 2019, Wu 2018, Yu 2017a]. The reduced interlayer distance leads to an increased overlap of the e^- and hole h^+ wavefunctions, which are spatially separated into distinct layers. This enhanced wavefunction overlap results in a higher oscillator strength of the IXs, accounting for the observed 15% (on H-type) and 138% (on R-type) increase in intensity compared to non-ironed (and 10 nN) scan areas, as presented in Figure 3.19(c) and Figure 3.23(c) respectively.

The heightened moiré effect also explains the increase in the broadening of the IX PL spectrum with the increasing ironing force. At the same time, a narrower line width distribution is observed as shown in the histograms in Figure 3.18(d-f) and Figure 3.23(b). This suggests that the increased broadening is not linked to disorder, but rather stems from the evolution of the intrinsic IX properties.

To quantitatively describe the lineshape evolution, we analyze the change in the difference (δE) between the maximum of the PL peak ($E_{\max}$) and the center-of-mass (C.O.M) energy by introducing a Difference function (δE), defined as,

$$\delta E = E_{\max} - \frac{\sum E \cdot I(E)}{\sum I(E)} \tag{3.8}$$

where, E denotes the energy and $I(E)$ denotes the intensity at the given emission energy(E). δE represents the distribution of PL intensity with respect to the peak energy. This is exemplified by the alteration in IX PL lineshape upon ironing, as presented by the spectra in Figure 3.25(a). The spectra are collected from the ironed (80 nN) and non-ironed (0 nN) areas of the same heterostructure. This figure presents the δE calculated from the E_{max} and C.O.M of the spectra from the integration. The calculated δE is -1.2 meV for the 80 nN scanned area and 18.4 meV in the 0 nN area. We see that in non-ironed regions, the PL spectrum displays a typical low-energy tail, indicative of structural disorderliness in semiconductors. Whereas, in ironed areas, the PL spectrum becomes more symmetric or occasionally presents a high-energy shoulder. The histogram distribution of δE over areas scanned with different forces is presented in Figure 3.25(b). A positive δE signifies a low-energy spectral tail, while negative δE indicates the presence of a high-energy shoulder. In non-ironed regions, the δE distribution is centered around ∼15 meV (refer to Figure 3.25(b)). With ironing, δE decreases and approaches 0 meV, and for higher forces, it becomes negative (as shown in Figure 3.25(b)), confirming that the center-of-mass is larger than the peak energy, which in turn confirms the peak asymmetry.

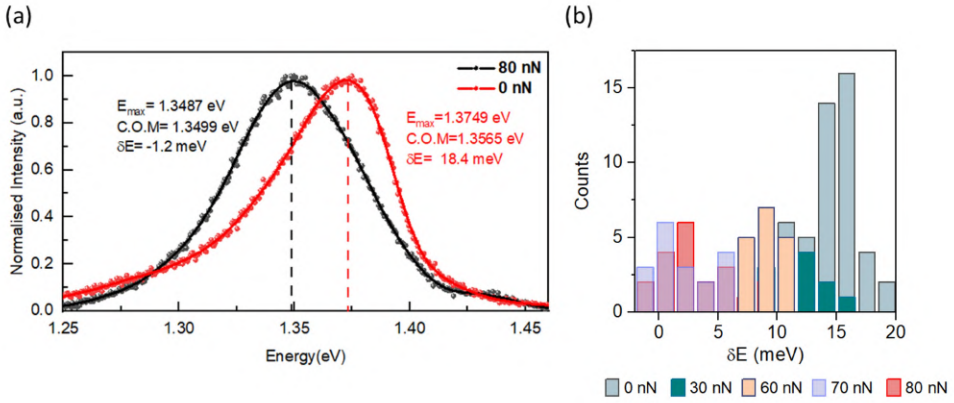

Figure 3.25: (a)The exemplary spectra are from 80 nN (black) and non-ironed (red) areas. The parameters are calculated by integration. (b)The evolution of the difference δE between the maximum of the PL peak and the PL center of mass (C.O.M) is plotted as a function of ironing force. A positive δE signifies a spectral tail on the low-energy side, while a negative δE indicates a high-energy tail.

This alteration is attributed to the heightened coupling between monolayers constituting the heterostructure post-ironing, as schematically depicted in Figure 3.26. Following ironing, the potential landscape becomes more uniform (as evidenced by reduced variation of full-width half-maximum), and increased layer coupling deepens

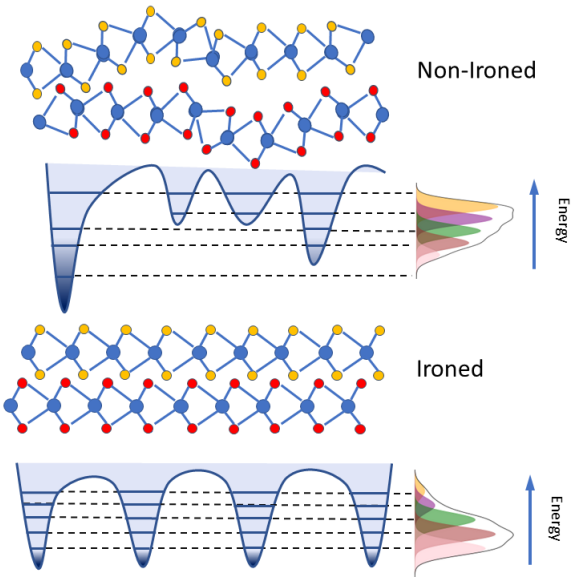

Figure 3.26: A schematic representation of the changes in the moiré potential and photoluminescence (PL) spectra during the ironing process. The closer proximity of the layers in the flattened structure amplifies the moiré potential, making it more uniform and, on average, deeper, thus allowing it to accommodate more states.

the moiré potential. This facilitates the binding of high-energy states, contributing to the emission on the high-energy side of the PL peak[Tran 2019, Wu 2018]. This discussion addresses the apparent contradiction of an improved spatial uniformity of the line width observed alongside a consistent (or slightly increasing) average value of line width that does not diminish after ironing.

Chapter 4

Magneto-Transmission measurements

Contents

This chapter begins by exploring the nuances of the magneto-optical measurements and then presents a concise review of the technical specifications of the various magneto-optical setups used by different research groups and highlights their major shortcomings. Following this, we discuss the design, development and instrumentation of the 'flake probe' I developed. We then examine the pulse magnetic field generation at the LNCMI-Toulouse facility. Finally, it includes a discussion of the magneto-transmission measurements conducted on $(PEA)_2PbI_4$, a two-dimensional perovskite flake, serving as a proof of concept.

4.1 Magneto-optical measurements

Magneto-optical measurements have emerged as a crucial tool in the exploration of the electronic and optical properties of 2D semiconductors, particularly TMDCs. These materials with their unique valley degrees of freedom and significant SOC, present a rich playground for studying fundamental physical phenomena and developing next-generation optoelectronics. Having established the concepts of spin-orbit coupling (SOC), the significance of the K and K' valleys and the role of time-reversal symmetry in Section 1.3, we can now discuss the motivations behind the magneto-optical measurements on these materials.

The study of valley pseudospin in TMDCs is particularly compelling. One of the most profound ways to achieve control over valley pseudospin is through the application of magnetic fields. The interaction between the magnetic field and the orbital magnetic moments of the electrons in the valleys can lift the degeneracy between the K and K' valleys, a phenomenon known as the valley Zeeman effect. This magnetic tuning of valley pseudospin has been demonstrated in various TMDCs, providing a pathway to control valley polarisation and coherence. Aivazian et al. showed that applying an out-of-plane magnetic field to monolayer WSe_2 leads to valley Zeeman splitting, allowing for magnetic control of the valley pseudospin[Aivazian 2015]. Similarly, Li et al. conducted valley-resolved magneto-photoluminescence on monolayer $MoSe_2$ and showed the lifting of the valley degeneracy through the opposite energy shifts induced in the excitonic transitions in the two valleys by the magnetic field. [Li 2014b].

Although conducting micro-optical measurements in high-magnetic fields is not straightforward experimentally, there have been significant developments in the direction[Li 2014b, Zhang 2017b, Stier 2016]. Given that the size of the TMDC crystals is typically on the order of a few tens of micrometres, performing micro-optical measurements under extreme magnetic fields presents a significant challenge. We will now discuss the various magneto-optical setups that have been used by various groups and cite the limitations I had to mitigate while developing this new flake probe for the purpose.

4.1.1 Review about magneto-optical setups

In this section, we will briefly discuss the various setups used to conduct magneto-optical studies on TMDCs. For instance, Zhang et al. made use of a fibre-based probe to conduct measurements at a magnetic field of 31 T to study the brightening of the dark excitons in CVD-grown monolayer WSe_2[Zhang 2017b]. The unit was designed to be loaded into a coil of 24 mm bore diameter. The setup, shown in Figure 4.1 was used to conduct micro photoluminescence (PL) measurement in the Voigt[1] geometry.

Similarly, to study TMDCs in high magnetic fields, Stier et al. made use of a micro transmission probe setup to show the influence of dielectric environment on the size of the exciton in WSe_2[Stier 2016]. They exfoliated WSe_2 monolayers onto single-mode optical fibres to perform polarised low-temperature magneto-absorption studies at 65 T. The optical transmission probe setup in Faraday[2] configuration, used in these experiments is schematically illustrated in Figure 4.2(a). White light from an Xe lamp is transmitted through a single-mode fibre into the WSe_2 flake and collimated using a graded index (GRIN) lens. A circular polarizer allows for $\sigma\pm$ selective analysis of the transmitted intensity in magnetic fields. The light is retro-reflected, and collected via a large-core optical fiber. All optical elements are

[1] In Voigt configuration, the magnetic field $\vec{B}$ is applied perpendicular to the direction of the light propagation vector $\vec{k}$.

[2] In Faraday configuration, the magnetic field $\vec{B}$ is parallel to the light propagation vector $\vec{k}$.

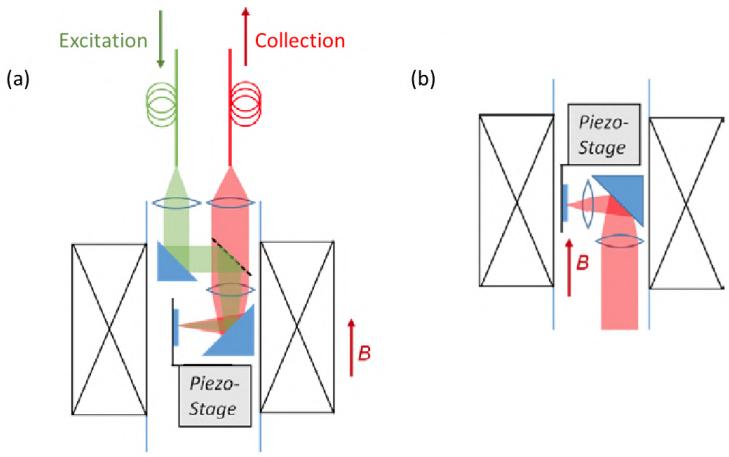

Figure 4.1: Schematics of the fibre-based probe used by Zhang et al. Design of probe heads for (a) fibre-based optics measurements and (b) free-space optics measurements in the Voigt geometry. Reproduced with permission from Springer Nature,[Zhang 2017b].

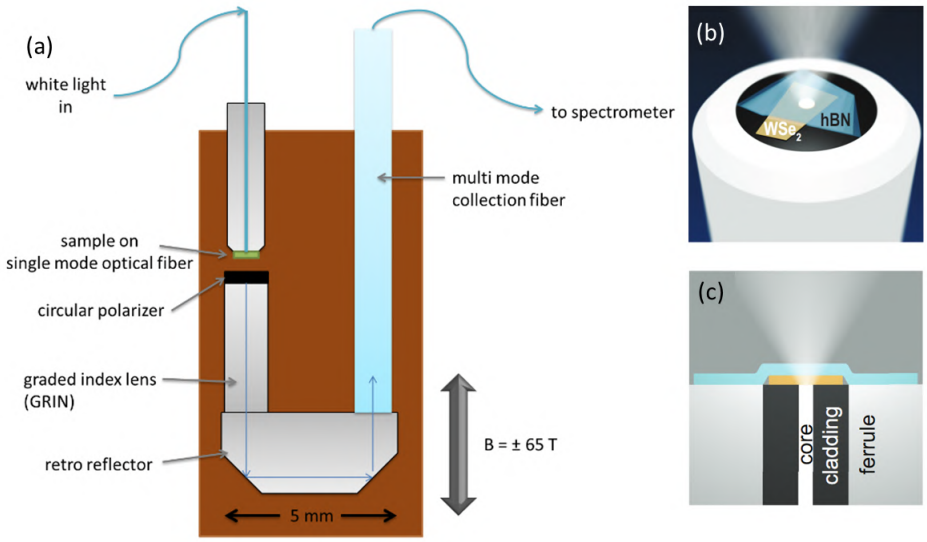

Figure 4.2: (a) Schematic of the optical transmission setup used. (b,c) Experimental schematic: An exfoliated monolayer WSe_2 crystal is transferred and aligned over the 3.5 µm diameter silica core of a single-mode optical fibre. Adapted with permission from [Stier 2016] Copyright 2024. American Chemical Society.

mounted in a custom Vespel probe, enabling experiments at temperatures as low as 1.5 K within a vacuum jacket.

In a setup developed by Babinski et al., a superconducting magnet is employed to generate magnetic fields up to 17 T, with a bore radius of 32 mm, for studying the magneto-reflectance properties of materials in the Faraday configuration. The

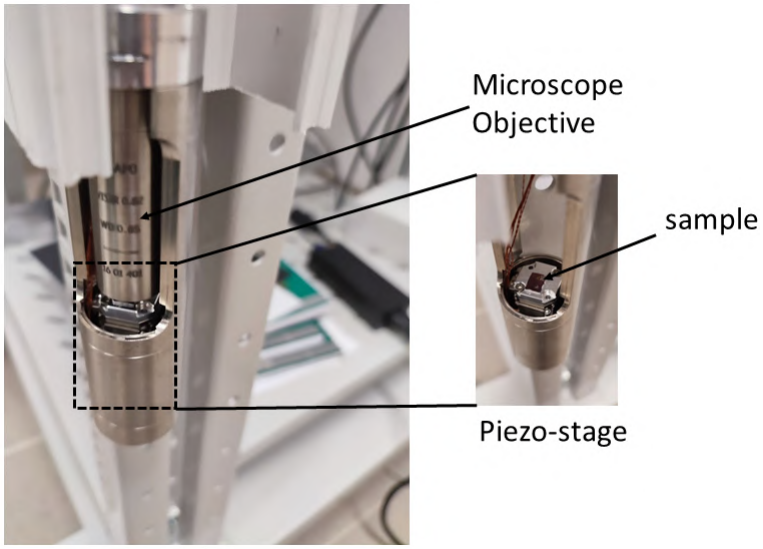

Figure 4.3: Image showing the microscope objective aligned on the sample on piezo stage in the experimental setup developed by Babinski et al.

sample is mounted on a piezo stage to allow precise control of sample movement, and a microscopic objective is used to focus on the sample. Figure 4.3 illustrates the design utilized by the team, showing the alignment of the microscopic objective on the piezo stage. This setup is then lowered into the center of the magnetic coil for measurements.

In the discussion of the three configurations, we will examine the various design parameters and limitations of each design. We will also outline how we overcame these challenges to develop a flake probe capable of operating in high magnetic fields up to 70 T. It is essential to first consider the design and setup employed by Zhang et al. for studying CVD-grown WSe_2 in high magnetic fields. They utilized a coil with a bore diameter of 24 mm for measurements conducted at 31 T. The larger bore diameter allowed them to incorporate a lens system to focus on the sample and a piezo stage into the probe within the cryostat.

In contrast, to achieve magnetic fields up to 70 T in the pulsed field, our setup is constrained to a bore diameter of 13 mm, with the helium cryostat accommodating a probe of 7.2 mm in diameter. The limited operational diameter significantly constrains our ability to position an objective within the cryostat for conducting measurements. In a primary workaround to this problem, one can employ cryogenic objectives from Attocube (⌀12-28 mm) (as employed by Babinski et. al, Figure 4.3) but, the utilization of objectives in pulsed magnetic fields presents substantial challenges due to the introduction of vibrations, which adversely affect the precision and reliability of the measurements. In Figure 4.4, I present the different pulsed and static magnetic fields along with the bore diameters of these magnetic field setups. The plot shows that as the magnetic field strength increases, particularly beyond 60 T, the bore diameter becomes significantly smaller. This reduction in

bore diameter presents a physical limitation, as it becomes challenging to fit even the smallest microscopic objectives within the available space. The trend observed in the plot underscores the inverse relationship between achievable field strength and bore diameter, highlighting the constraints faced when designing high-field magnetic setups.

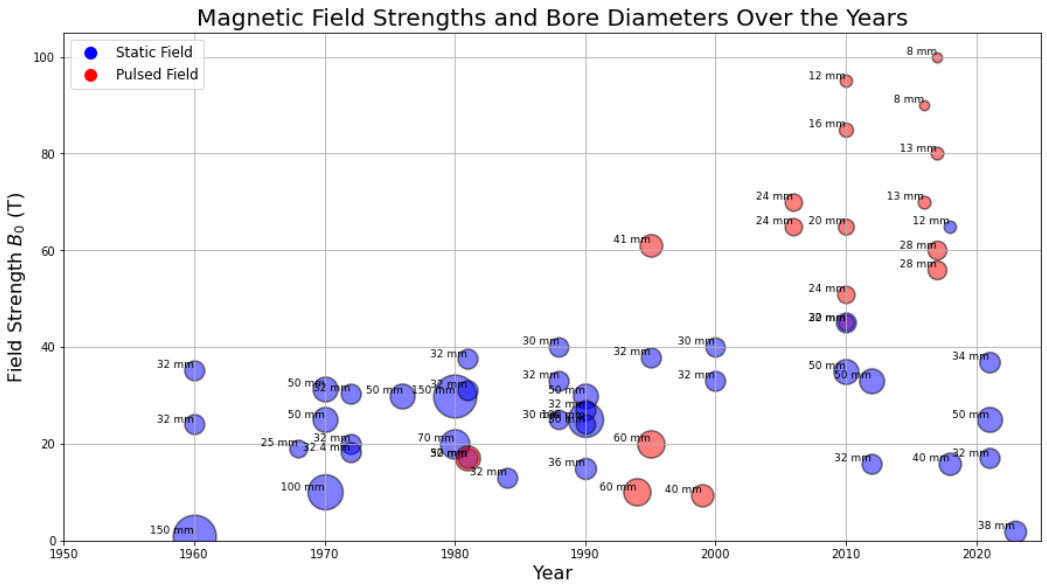

Figure 4.4: This plot illustrates the different magnetic field strengths generated by various high magnetic field setups with different bore diameters over the years. Data taken from [Herlach 1995].

Stier et al.'s design enables measurements on microscopic samples, such as TMDC flakes, with dimensions spanning a few tens of micrometres. This was accomplished by transferring the flakes onto a monomode fibre, a technique which will also be integral to our probe design. However, their approach revealed several inefficiencies and incorporated high-cost components. Firstly, they utilize a retroreflector, which is a costly piece of equipment. Secondly, while the design incorporates a collimation lens on the injection side using an expensive GRIN lens, the collimated beam is not subsequently focused on the collection fibre, leading to potential intensity loss. Additionally, the transmission of non-collimated light through the polarizer introduces partial polarization of the signal, reducing the efficiency of the polarizers and introducing angular dependency to the beam. By addressing these design shortcomings, we can develop a more cost-effective flake probe with improved signal quality for micro-sized flakes. The design considerations and optimizations of the flake probe will be discussed in detail in the following sections.

4.2 Magneto-transmission setup in our facility

The setup I developed in-house with the assistance of Andrzej Nowok and the

instrumentation team, successfully addresses the issues we pointed out in the last Section 4. The schematics of the setup is presented in Figure 4.5. It constitutes three important sections, namely, the free space excitation and detection, the flake probe and the resistive coil for the generation of pulsed magnetic fields.

To excite the sample on a small fibre core of 10 µm, a special arrangement is put in place. As shown in Figure 4.5, a white light source is collimated using an off-axis parabolic mirror (Thorlabs inc.) and targeted at a super achromatic microscopic objective with a numerical aperture of 0.1 NA, to match with the numerical aperture of the 10 µm core fibre. This minimizes the loss of intensity due to over-filling[3] the injection fibre. The fibre then transmits the coupled incident light through the sample flake at the end of the fibre, at the probe tip.

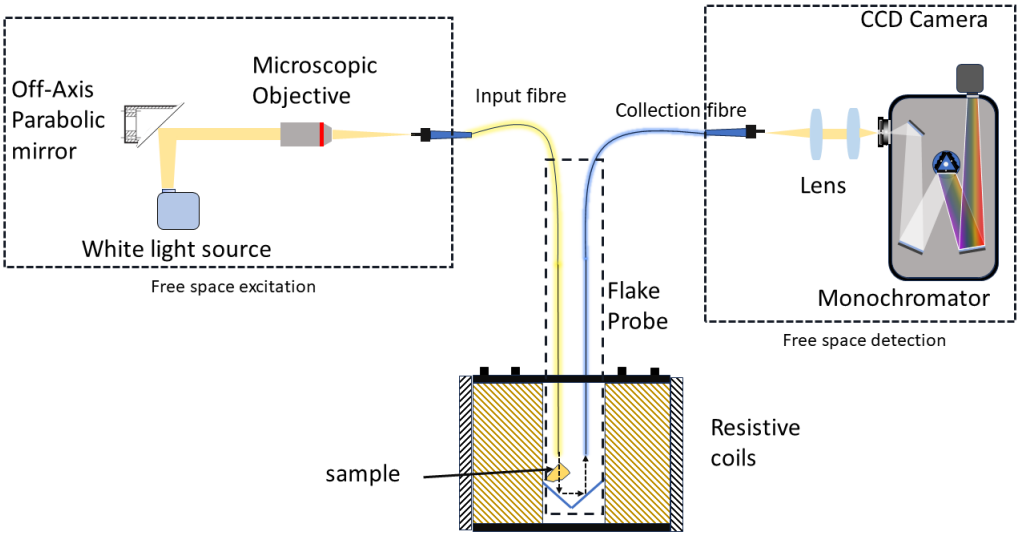

Figure 4.5: Experimental setup showing the injection part and the detection part of the flake probe.

The flake probe is then carefully placed inside the helium cryostat where the probe tip sits precisely at the center of the magnetic field within the bore of the resistive coil. A separate collection fibre collects the transmitted signal from the sample to the monochromator. Two lenses are used before the monochromator, one to collimate the signal and the other to focus the signal on the monochromator. In the following sections, we will discuss the design and optimisation of the flake probe and the technicalities of the resistive coil used for the magnetic field generation.

4.2.1 Design of our flake probe

The flake probe discussed in this subsection was designed, built and optimised by me, in-house at LNCMI Toulouse with the help of Sylvie George, Nicolas Bruyant

[3]Overfilling in single-mode fibres can lead to higher insertion loss due to light entering the cladding and inefficient coupling.

and Noé Estorges from the instrumentation team and Andrzej Nowok. This probe, like others in the facility, has two main parts besides the body. The probe body houses the carbon fibre tubing and provides structural support to the optical fibres inside the probe. The other parts are the probe head and the probe tip as shown in Figure 4.6. These two parts will be discussed in detail in the following subsections.

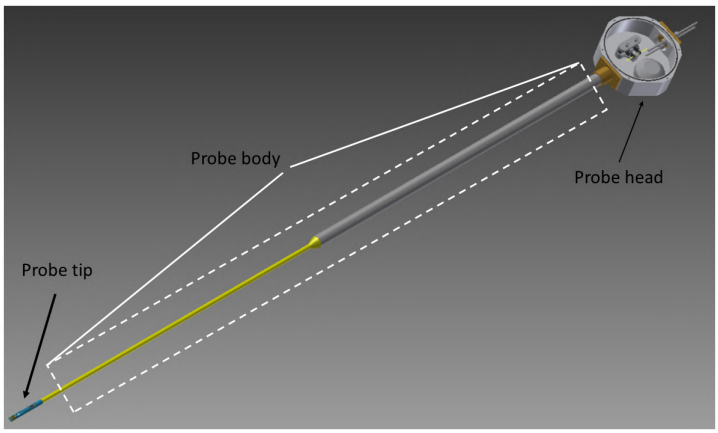

Figure 4.6: A computer-aided design(CAD) of the flake probe showing the probe head and the probe tip part.(Image courtesy- Sylvie George)

4.2.1.1 Probe head

The probe head houses the connection sleeve, which connects the sample fibre to the injection fibre from a light source. It also houses the connections for the temperature controller and the pick-up coil. Figure 4.7(a) shows the cross-sectional side view of the head of the flake probe. The probe head features two openings secured by vacuum-compatible screws, which permit the optical fibres for injection and collection to pass in and out of the probe. Figure 4.7(b) shows the insides of the probe head. It shows the 12-pin DIN connector on which 100 µm wires are soldered for the temperature sensor and the pickup coil. Two extra wires are also kept for standby in case any of the wires or connection fails. This wire can be soldered onto the desired place without dismantling the whole probe.

4.2.1.2 Probe tip

The probe tip as shown in Figure 4.8(a) was designed and developed by me using precise 3D printing with the help of the instrumentation team. As shown in Figure 4.8(a), it holds both the cryogenic temperature sensor (Cernox from Lakeshore) and the pickup coil. Figure 4.8(b), shows the cross-section of the probe tip, which has groves to contain the collimating lenses, focusing lens, mirrors, polariser and the injection and collection fibres. The light from the source travels along the incident path (indicated by the orange dashed line in the figure) within the sample fibre. It then transmits through the sample, gets collimated by the lens, reflects off two

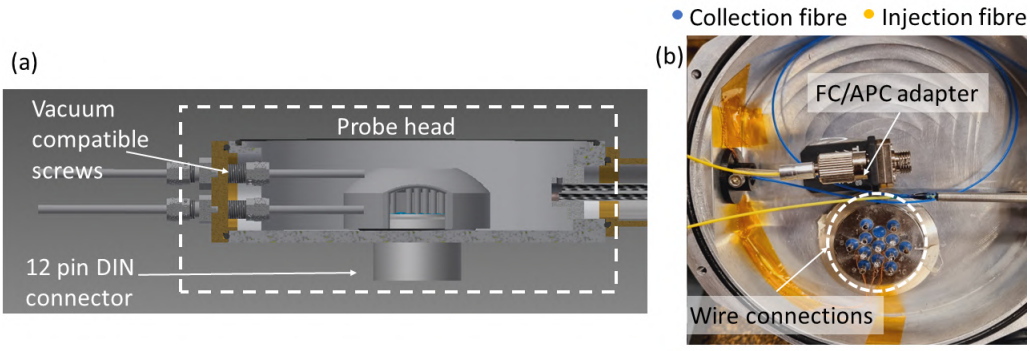

Figure 4.7: (a) Cross-sectional view of the probe head from the side. It shows the vacuum-compatible screws which hold the fibres entering the probe head in place. (CAD image courtesy- Sylvie George) (b) Shows the inside of the probe head which contains the FC/APC adapter, wire connections for the temperature sensor and the pickup and houses the injection and the collection fibre.

mirrors at 45 degrees, and is subsequently focused into the collection fibre. Finally, the light is transmitted to the spectrometer for analysis. These grooves help us to precisely adjust the position of the fibres from the lenses to attain maximum signal.

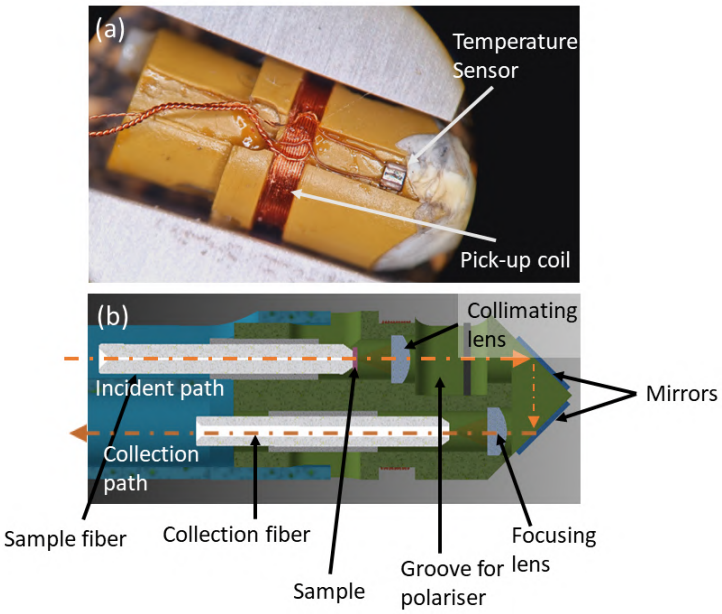

Figure 4.8: (a) Enlarged view of the probe tip (b) Cross-section of the probe tip showing different parts within. (CAD image courtesy- Sylvie George)

The cryogenic temperature sensor mentioned earlier is a four-terminal resistance thermometer which can operate at extremely low temperatures of superfluid helium (2.17 K). The temperature-resistance dependence can vary for different Cernox sen-

sors. The sensor used in this probe is particularly an uncalibrated one. To find this dependence, we used the resistance values provided in the datasheet for this particular temperature sensor and interpolated all the points in between the values provided. Figure 4.9 shows the calibration curve used to read the temperature from this sensor. The inset shows the schematic of the four terminal sensors.

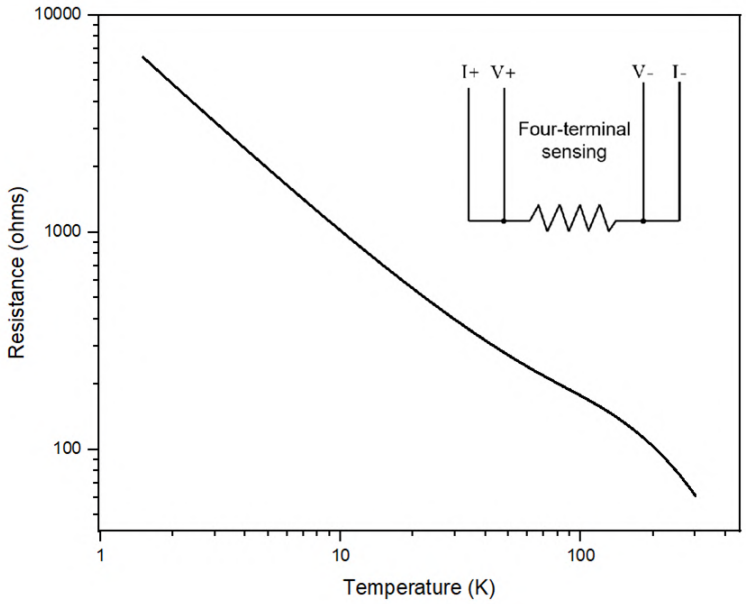

Figure 4.9: Calibration resistance/temperature curve of the resistance thermometer on the flake probe. Inset: schematic diagram of four-terminal sensing.

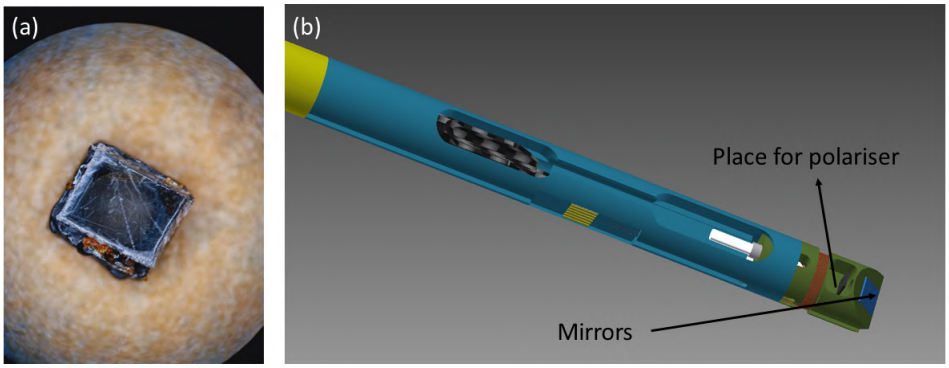

Figure 4.10: (a) Linear polariser with a quarter ($\lambda/4$) waveplate on the other side glued on a 3D printed mask.(b) It shows the part of the probe tip in which the polariser is placed during the measurements. (CAD image courtesy- Sylvie George)

The pickup coil inside the probe tip helps us to monitor the magnetic field produced in the coil. This operates on the fundamental principle of Faraday's electromagnetic induction. The pick-up is a coil made up of 10 loops of 100 µm

diameter insulated copper wire. When it encounters a change in the magnetic field, it induces a voltage (V) in the coil to counteract the change in the magnetic field,

$$V = -\frac{d\phi}{dt} = -N \times S\frac{dB}{dt} \tag{4.1}$$

where ϕ is the magnetic flux, N is the number of turns and S is the surface area of the loop and so $N \times S$ gives the effective area of the coil.

To study the Zeeman effect in a material, we need to conduct polarised magnetic field measurements. This is achieved using a linear polariser and a quarter ($\lambda/4$) wave plate, which enables the collection of the spectra from particular valleys. Figure 4.10(a) displays the circular polariser employed for these measurements. This polymer sheet features a linear polariser with its polarising axis aligned at 45 degrees to the fast axis of the $\lambda/4$ waveplate. Figure 4.10(b) illustrates the groove in the probe where the polariser is positioned during measurements. The subsequent section will address the preparation of sample fibers.

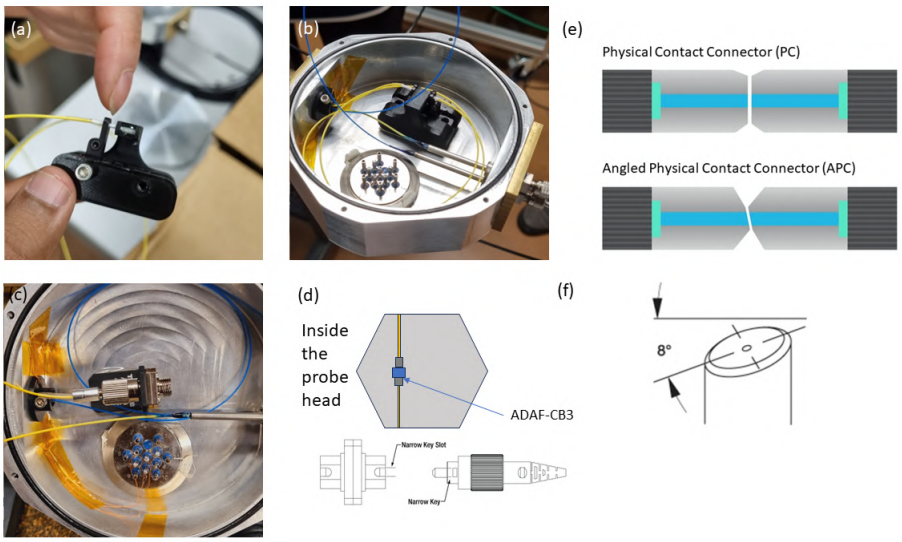

Figure 4.11: (a) Shows the initial arrangement to connect the fibres using a 3D-printed connecting sleeve. (b) Shows inside the probe head which houses the connection sleeve. (c) The modified setup implements the FC/APC connection sleeve to pacify febry-perot oscillations. (d) Schematics of the FC/APC connection and the connector sleeve. (e) Comparision between the flat physical contact (PC) connector and the angled physical contact (APC) connector. (f) The APC connector is angled at 8°.

4.2.2 Preparation of the sample fibres

The specific arrangement of the flake probe allows us to conduct measurements from a very small region of the sample, spanning in the range of micrometres. This

arrangement enables us to perform µPL and micro-transmission measurements on sample crystals with micrometer-scale dimensions.

To make this possible, monomode fibres with a core of size 10 µm were used. With the initial design of the probe, a flat ceramic ferrule-to-ferrule connection was used. Figure 4.11 (a) and (b) illustrates the schematics of the initial design of the ferrule connection, in the probe head. A 3D printed component (shown in black in Figure 4.11(b)) housing the ADAL1-5 Thorlabs mating sleeve was used to couple the two fibres. The major drawback of the design is that it introduces Fabry-Perot interference in the spectrum. To overcome this problem, the flat ceramic ferrules were replaced with FC/APC connections as shown in Figure 4.11 (c-d). The face of the ferrules was angled at 8°, which reduced the possibility of Fabry Perot oscillations. Figure 4.11(e) compares the two types of ferrules we discussed and the face of the APC connector is shown in Figure 4.11(f). Custom-made fibres from Thorlabs were used. One end has FC/APC termination, and the other end has a flat ceramic ferrule termination to hold the sample.

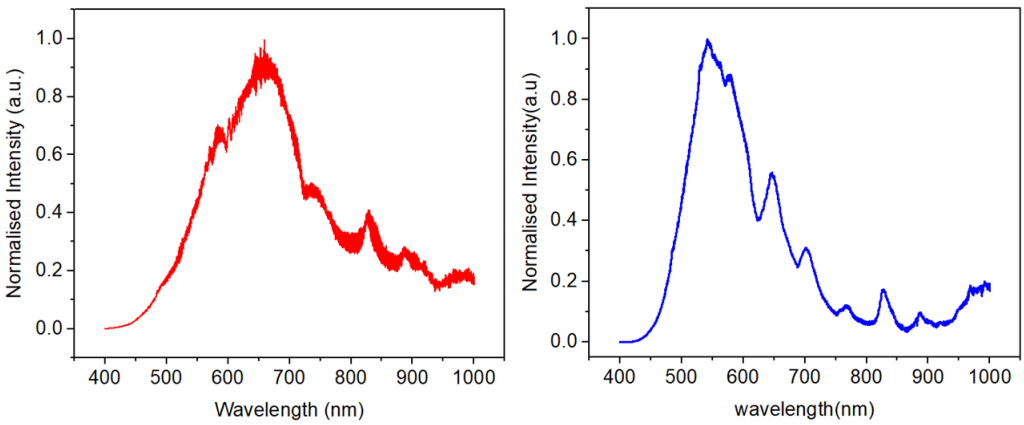

Figure 4.12: The graph in the left panel shows the occurrence of Fabry-perot oscillations in the previous configuration i.e. flat ferrule connection. The right panel shows the absence of these oscillations in the FC/APC arrangement.

In Figure 4.12, we compare the spectral characteristics observed after replacing the flat-face ferrule with FC/APC ferrules. The results indicate that Fabry-Perot oscillations, which were prevalent in the flat-face configuration, are significantly reduced in the FC/APC configuration. This change highlights the effectiveness of the FC/APC ferrules in minimizing interference effects and improving spectral quality.

The transfer setup used to transfer the target flakes on the fibre core is presented in Figure 4.13(a). The setup constitutes the 3-axis motorised stage which helps us to precisely control the movements of the flake on the PDMS stamp, under a microscopic objective. The fibre is held upright with the help of an FCM13 mount from Thorlabs. Once the flake has been located on the PDMS, the flake is lowered in a controlled manner using the motorised stage towards the ferule flat face. The

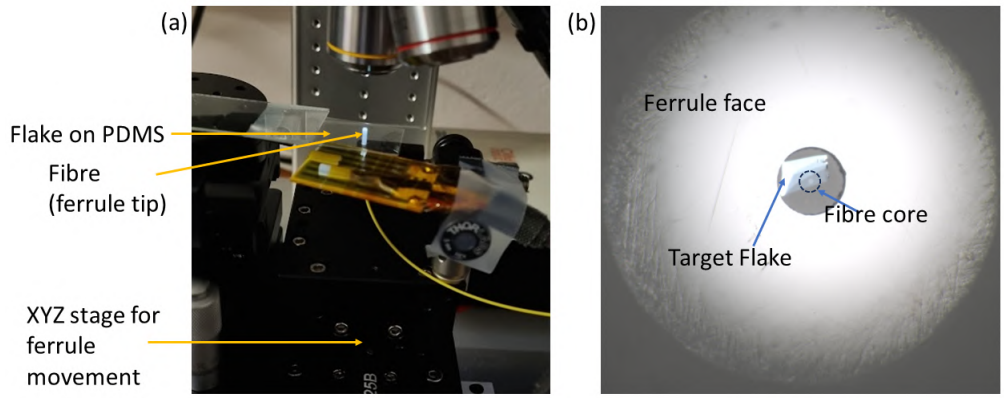

Figure 4.13: (a) The transfer setup used to transfer flakes on the fibre. (b) Shows the transferred flake on the core of the fibre seen under a microscope.

flake is aligned to the core of the fibre and lowered to make contact with the core and then the PDMS is slowly retracted leaving behind the flake on the fibre core. The final result of the transfer is shown in Figure 4.13(b). The flake can be seen covering whole of the core of the optical fibre.

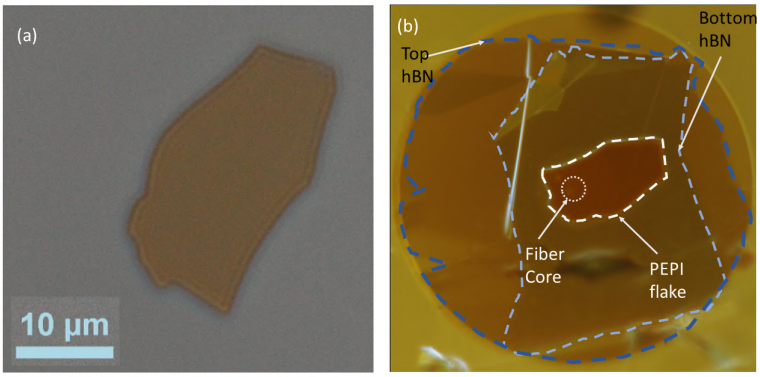

Figure 4.14: (a) Image showing the PEPI flake chosen for transfer to the fibre after exfoliation. (b) Shows the stacked heterostructure of hBN/PEPI/hBN on the fibre.

I initially started with the in-house setup for the transfer of flakes on the fibres. The setup was optimised still the success rate of transfer was low. In collaboration with TU Munich, Maciej Smiertka, from our team, conducted the fabrication process for encapsulated monolayers of perovskites, specifically the phenethylammonium lead iodide($(PEA)_2PbI_4$ abbreviated as PEPI). The transfer of flakes to the ferrule was accomplished using the highly precise dry transfer technique. Figure 4.14(a) shows the PEPI flake selected for the transfer. Figure 4.14(b) shows the transferred PEPI flake on the core of the sample fibre with hBN encapsulation to ensure the crystal does not degrade in ambient.

4.3 Pulsed magnetic field

High magnetic fields can be categorised as continuous steady fields that can be maintained for entire duration of experiments like few hours, and pulsed magnetic fields, which are brief and lasts about 10-100 milliseconds. This section will focus on pulsed magnetic fields central to the operations at the LNCMI-Toulouse facility. In our setup, a solenoid is used to generate a magnetic field (B-field) when current (I) passes through it. The B-field magnitude is proportional to the current and the solenoid's turn density (n), described by:

$$B = \mu_0 n I$$

where μ_0 is the magnetic permeability of free space. The right-hand rule determines the field's direction. This relationship is crucial for generating the significant magnetic pulses used in experiments at the LNCMI-Toulouse facility.

To generate a magnetic field in the facility, a generator and a resistive coil are required. These components will be discussed in the following sections. The process initiates with the accumulation of charges in a capacitor bank, which is subsequently discharged into a resistive coil. In essence, the electrical energy stored in the capacitors is transferred to the coils, resulting in the creation of a magnetic pulse.

LNCMI in Toulouse is equipped with the capability to generate non-destructive pulsed magnetic fields reaching up to 98.8 T. Additionally, the facility is equipped to create destructive magnetic fields of up to 209 T. This capability allows researchers to explore and manipulate materials under extreme magnetic conditions.

4.3.1 Generators

This facility houses two capacitor banks i.e. 14 MJ and 6 MJ, which are used to energise the resistive coils. In Figure 4.15, we summarise the different fields and their duration possible at the facility. The 14 MJ capacitor bank has 14 parts. Each part holds up to 1 MJ of energy, and a total capacitance of 48 mF. The 6 MJ capacitor bank has two 3 MJ parts, and the total capacitance is 21 mF. By combining these with different resistive coils, the lab can create magnetic field pulses with various durations and strengths for experiments. As shown in Figure 4.15, the 70 T and 60 T magnetic coils with a bore diameter of 13 mm are powered by the 6 MJ or the 14 MJ. Whereas, a magnetic field of 90 T is achieved in a resistive coil of a bore diameter of 8 mm. The design of this coil is different to others. This is a dual coil design in which one coil is powered by 6 MJ and the other is powered by the 14 MJ capacitor bank. The variation of the pulse duration takes into account the physical specifications of the coil like its bore diameter and the capacitor bank it is connected to.

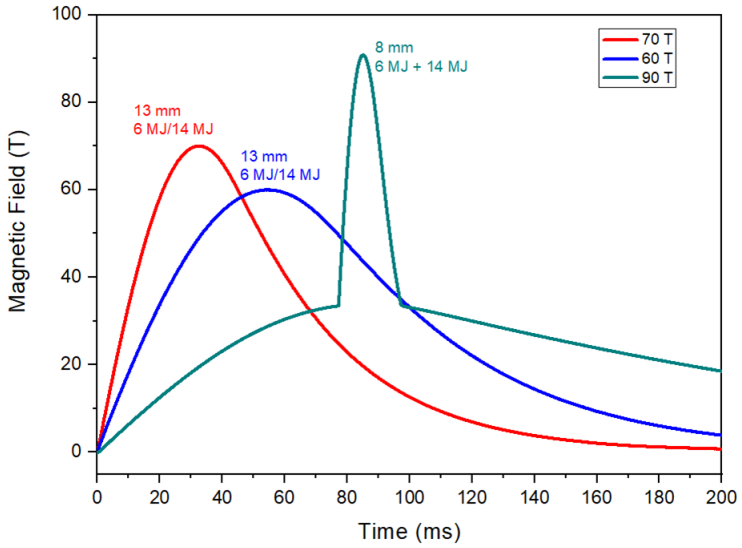

Figure 4.15: Magnetic field profiles as a function of time duration, obtained by different resistive coils. It also indicates the bore diameter of the coil at 77 K.

4.3.2 Cryostat

In Figure 4.16(a), we present the schematics of the cryostat used in the facility. Conducting magneto transmission measurements at low temperatures necessitates using a cryostat specifically designed for this purpose. The system comprises two compartments: the helium cryostat, depicted in Figure 4.16(b), nested inside the nitrogen cryostat. This specially designed helium cryostat consists of two main parts: the top bath and the lower bath, which are separated by a needle valve as shown in the schematics. This needle valve allows the controlled transfer of liquid helium from the top bath to the lower bath. The bottom bath has a long and narrow extension which is inserted directly into the bore of the coil. The probe containing the sample at the probe tip is placed at one end of the tail. A resistive heating coil made up of manganin is placed at this point, which allows the user to precisely control the temperature from 4.2 to 300 K.[LNCMP-team 2004]

4.3.3 Resistive Coils

Homemade resistive coils (shown in Figure 4.16 (c)), face two primary technical hurdles. First, there is a substantial magnetic pressure generated during the pulse, and second, the challenge of coil heating. Magnetic pressure is the amount of energy stored per unit volume in the space where the magnetic field is present. Mathematically it can be defined as $P_m = B^2/2\mu_0$, where B is the magnetic flux density and μ_0 is the permeability of free space. This pressure arises from the gradient in the magnetic field strength, which exerts a force that can generate tensile stress in the elements such as a conducting loop. At higher currents, the magnetic pressure can

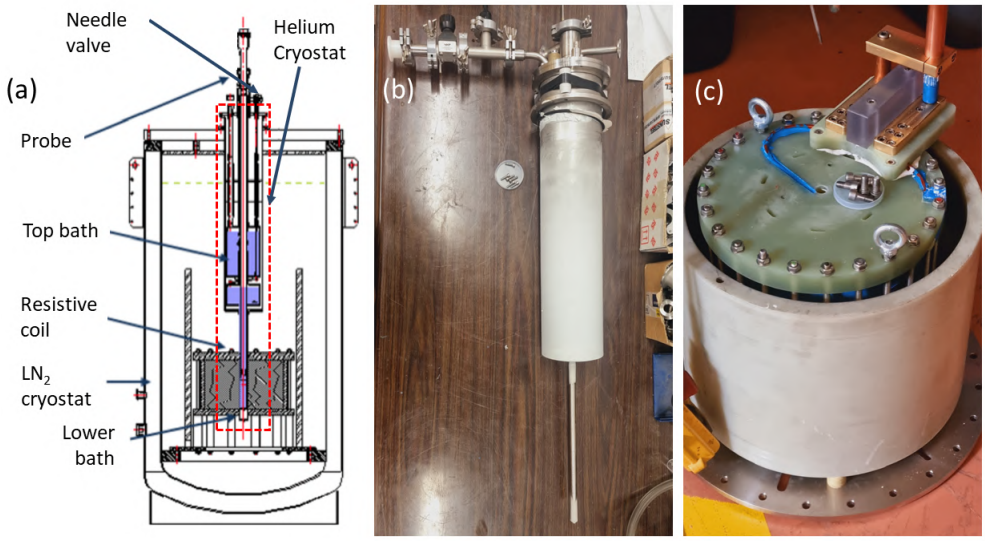

Figure 4.16: (a) Schematics of the cryostat (adapted from instrumentation team, LNCMI). The schematics show the helium cryostat (marked by red dotted lines) indicating the top and the lower baths, the liquid nitrogen (LN_2) cryostat, the resistive coil magnet and the probe. (b) Helium cryostat (c) The resistive coil which stays immersed in the liquid nitrogen inside the nitrogen cryostat.

cause the tensile stress to surpass the material's tensile strength leading to fracture or fragmentation of the current-carrying loop. To address the magnetic pressure issue, a unique alloy, CuSS (Copper Stainless Steel) with Zylon is employed. This material blend provides enhanced intrinsic strength without sacrificing conductivity. The CuSS alloy is designed to withstand the high magnetic pressures encountered during operation, while Zylon fibres offer additional mechanical support.

During a pulse of magnetic field, the temperature in and around the coil can increase significantly. To reduce the time required to bring down the temperature of the coil back to the operational temperatures, an effective solution involves immersing the coil in liquid nitrogen inside the specially designed cryostat as shown in Figure 4.17(a). The image shows the resistive coil placed inside the LN_2 cryostat seen through the opening made for placing the helium cryostat. Additionally, as depicted in Figure 4.17(b) the presence of vertical cooling channels inside the coil enhances the cooling rate significantly. These cooling channels facilitate efficient heat dissipation by increasing the surface area in contact with the coolant, By optimising the flow of the liquid nitrogen through these channels, the system ensures rapid and uniform cooling, preventing thermal hotspots and improving overall performance and longevity of the coil. This cooling method helps maintain the coil's temperature within acceptable limits during magnetic field pulses. Cooling down the coil to liquid nitrogen temperatures reduces the coil's resistance, which increases during the pulse predominantly due to Joule heating, given by the relation,

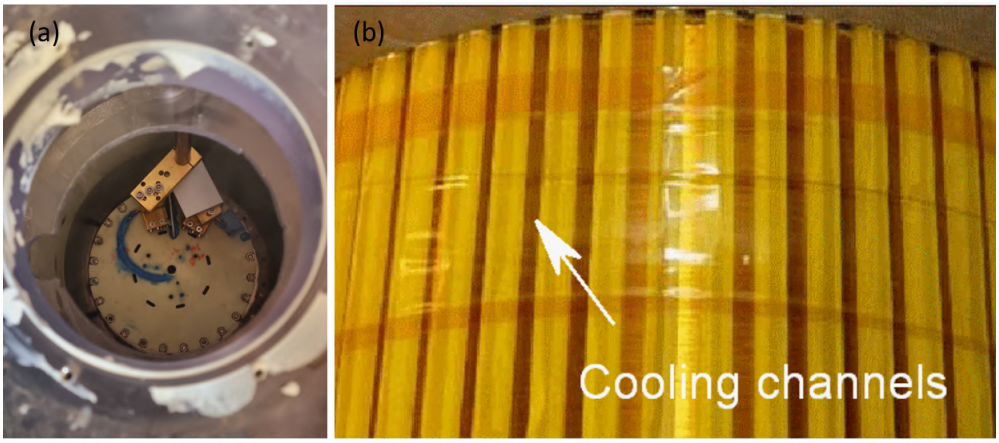

Figure 4.17: (a) Image showing the resistive coil sitting inside the nitrogen cryostat (seen through the opening made for the helium cryostat. (b) Cooling channels for the LN_2 circulation.

$Q = I^2Rt$, where Q is the heat energy produced, I is the current flowing through the coils, R is the electrical resistance and t is the time for which the current flows. Cooling down time of the coil to acceptable values depends on the field strength generated during the pulse.

Various combinations of the generators and coils along with different bore diameters result in different magnitudes and durations of pulse. Figure 4.15 gives a comprehensive view of the magnitude and duration of the pulses that can be generated in the facility at LNCMI-T. For example, the 70 T coil, which will be central to our discussion, has a 13 mm bore diameter. The typical duration of the pulse is 60 ms when the 6 MJ capacitor bank is used for charging the coil.

4.3.4 Synchronisation

In experiments with pulsed magnetic fields, precise timing synchronisation is crucial. For the 70 T field, which is central to our new experimental setup, the total effective duration of the pulse is approximately 60 ms. This further emphasizes the necessity for the precise synchronisation between the camera CCD and the magnetic pulse. To achieve this, we've put together an arrangement of trigger box and repeater to synchronize everything down to a fraction of a millisecond. The flow of how the synchronisation works is as follows:

The synchronisation algorithm is illustrated in a schematic flowchart in Figure 4.18. In this scenario, the CCD detector acts as the master trigger. First off, we send a pre-trigger signal to the detector to get it ready. Then the detector sends a series of pulses to acquire multiple frames to a waveform generator and an oscilloscope (from Hioki Inc.). The waveform generator converts the pulses into a transistor-transistor logic (TTL) rise signal that later is sent to the delay unit. The delay unit retards the trigger such that the acquisition of the spectrum occurs at

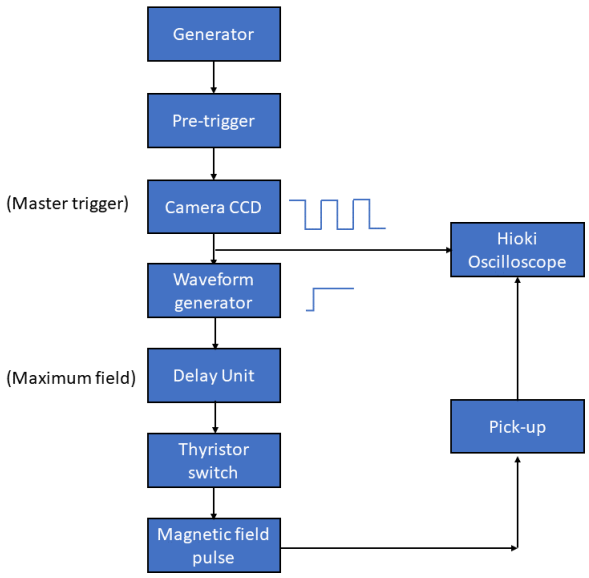

Figure 4.18: Schematic representation of the synchronization sequence in magneto-transmission measurements.

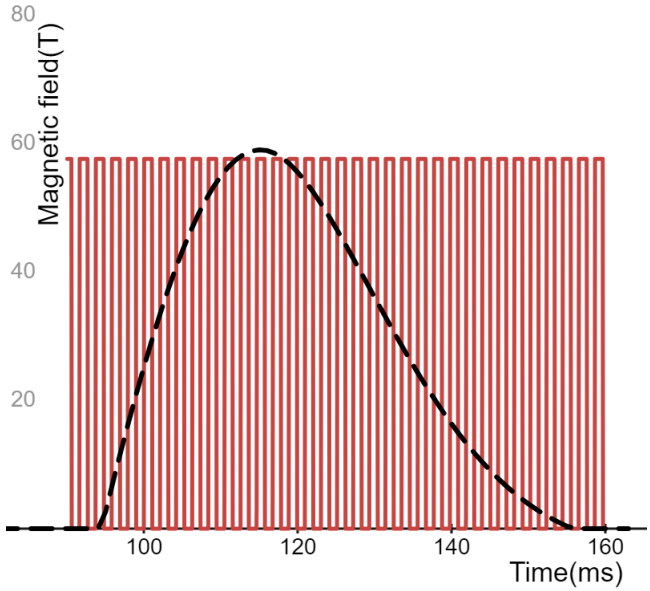

Figure 4.19: Magnetic field(black dashed line) as a function of time, during the 60 T pulse. Red rectangles represent the CCD acquisition frames.

the maximum of the magnetic pulse. The delay time has to be precisely adjusted. As an example, we show in Figure 4.19 a series of 35 CCD acquisition frames, each of 2 ms acquisition time on a Si CCD. The black dotted line in the plot denotes the 60 T magnetic pulse.

Prior to each pulse of a magnetic field, the CCD and the oscilloscope are activated into triggering mode. Once the user charges and presses the fire button, the magnetic pulse arrives exactly after the delay time set. In terms of number of frames, it is the delay time upon the acquisition time of each frame. The pulse is detected as a large spike by the pickup coil placed at the tip of the probe. Once the sequence of the CCD spectrometer frames and the magnetic field pickup signal is acquired by the oscilloscope, every frame or spectra can be mapped to the corresponding magnetic field value.

4.4 Magneto-transmission spectroscopy of $(PEA)_2PbI_4$

To ensure the proper functionality of the setup and verify the effectiveness of all arrangements, we conducted transmission spectroscopy on phenethylammonium lead iodide (PEPI) under the influence of a magnetic field.

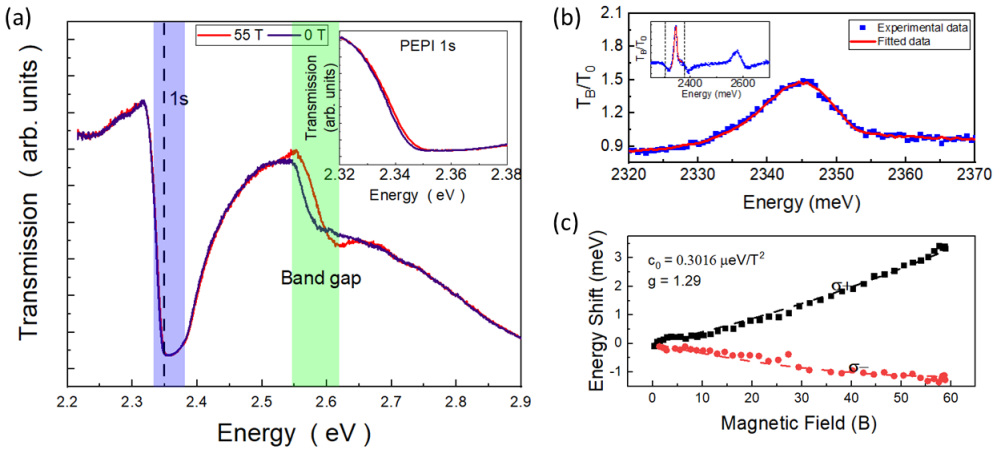

Figure 4.20: (a) Transmission spectra of PEPI collected at 2K at 0 T and 55 T show a visible shift in the 1s excitonic transition (in the inset figure) and the band gap. (b) T_B/T_0 spectra at 1s transition fitted using least-squares to find the energy shift. (c) Plot showing the energy shift for both the polarisations with the shift values calculated from the fit.

I studied the influence of the magnetic field on the transmission spectra of PEPI on the circular polarization basis. Figure 4.20(a) presents the transmission spectra of the PEPI crystal under the influence of a magnetic field, illustrating the shift of the excitonic (1s) absorption at 2.35 eV (shown in the inset of the Figure 4.20(a)) and the high-energy feature at 2.6 eV, corresponding to the bandgap. The small spectral shift induced by the external magnetic field is determined by calculating the ratio of the spectra measured in the magnetic field to the 0 T spectrum. The

resulting ratio spectrum, $\frac{T_B}{T_0}$, exhibits characteristic sharp features whose amplitude, width, and position are highly sensitive to the energy shift relative to the 0 T field spectrum. I assumed that the external magnetic field introduces only an energy shift while maintaining the overall lineshape of the spectrum, the ratioed spectrum can be represented as $\frac{T_0+\delta E}{T_0}$, where δE is a fitting parameter indicating the energy shift due to the magnetic field[Dyksik 2020, Baranowski 2019]. In Figure 4.20(b), the solid line correspond to the fit obtained using this method. The inset shows the ratioed transmission spectra in a broader range.

Measuring in both directions of the magnetic field allows access to the σ^+ and σ^- polarized states. The energy shifts for both polarizations were determined from the transmission spectra collected from PEPI, and the Zeeman split branches are presented in Figure 4.20(c). This plot demonstrates that the shift is different for the different polarizations. The plot shows that the σ^+ and σ^- branches show blue-shift and red-shift respectively. The non-symmetric shift for the polarizations results from a non-zero diamagnetic coefficient, c_0.

The diamagnetic shift, σ, was extracted by fitting the data points to the following equation:

$$\delta E_{\sigma_\pm} = \pm\frac{1}{2}g\mu_B B + c_0\frac{1}{2}B^2 \tag{4.2}$$

where g is the Landé g-factor, μ_B is the Bohr magneton, and c_0 is the diamagnetic coefficient of the transition. The fitting process, as a proof of concept, yielded a value of 0.3016 ± 0.0073 μeV/T^2 for the diamagnetic shift and a g-factor of 1.29 ± 0.012, which are very close to the values reported in the literature [Dyksik 2020].

Chapter 5

Conclusions

The research presented in this thesis discusses the intricate properties and applications of transition metal dichalcogenides (TMDCs), particularly focusing on MoS_2 and $MoSe_2$ monolayers and their heterostructures. This study highlights the significant advancements in the fabrication, characterization, and optimization of these materials, with an emphasis on their structural and optical properties.

The fabrication process employed in this research utilized a novel technique involving nail polish stamping, which allowed for the efficient exfoliation and assembly of TMDC heterostructures encapsulated by hexagonal boron nitride (hBN).

A major contribution of this thesis is the application of Atomic Force Microscopy (AFM) ironing as a post-fabrication technique to enhance the surface flatness and uniformity of the TMDC monolayers and their heterostructures. The AFM ironing process was systematically studied, revealing its effectiveness in reducing surface roughness and mitigating interlayer inhomogeneity. The AFM ironing was performed with forces ranging from 5 nN to 400 nN, which generated pressures approximately between 2.2 to 9.8 GPa. This process significantly improved the structural quality, as evidenced by a noticeable decrease in the surface RMS roughness and the reduction of bubble and wrinkle densities.

The optical properties of the TMDC heterostructures were extensively analyzed using steady-state photoluminescence (PL) spectroscopy. The results indicated that AFM ironing not only improved the structural integrity but also had a profound impact on the excitonic transitions. The PL spectra showed enhanced intensity and reduced linewidths, particularly in the ironed regions. For instance, the PL intensity in the ironed regions of sample B showed an average increase of about 15% compared to non-ironed areas. Similarly, in sample C, an increase of approximately 138% was observed in the intensity of the interlayer exciton (IX) peak.

Statistical analyses of the PL spectra revealed a redshift in the IX transition, which was roughly proportional to the applied ironing force, with a coefficient of -286 $\pm$ 225 µeV/nN for samples A and B, and 420 µeV/nN for sample C. Additionally, the linewidth distribution narrowed post-ironing, indicating a more uniform spectral distribution.

In Chapter 4, the development and utilization of a flake probe for magneto-transmission measurements were introduced. This innovative setup, synchronized with resistive coils and cryostat systems, enabled the precise study of the electronic properties of TMDC heterostructures under varying magnetic fields. The proof of concept was demonstrated on 2D phenethylammonium lead iodide (PEPI), providing critical insights into the magneto-optical behavior of 2D materials.

The findings of this research contribute significantly to the broader understanding of 2D materials and their potential applications in advanced nanoelectronic and optoelectronic devices. The successful application of AFM ironing to enhance the structural and optical properties of TMDC heterostructures paves the way for further investigations into other 2D materials and their heterostructures.

Future research could explore the scalability of the nail polish stamping technique for large-area fabrication of TMDC heterostructures and the application of AFM ironing to other types of 2D materials. Additionally, further studies on the interplay between mechanical forces and optical properties could provide deeper insights into the fundamental physics of 2D materials.

In conclusion, this thesis has demonstrated the critical role of innovative fabrication and post-fabrication techniques in advancing the field of 2D materials, particularly TMDCs. The improved understanding and enhanced properties achieved through these techniques hold great promise for the development of next-generation electronic and optoelectronic devices.

Appendix A

Publications

Publications based on the results of this thesis:

1. **Swaroop Kumar Palai**, Mateusz Dyksik, Nikodem Sokolowski, Mariusz Ciorga, Estrella Sánchez Viso, Yong Xie, Alina Schubert, Takashi Taniguchi, Kenji Watanabe, Duncan K. Maude, Alessandro Surrente, Michał Baranowski, Andres Castellanos-Gomez, Carmen Munuera, and Paulina Plochocka
   "Approaching the Intrinsic Properties of Moiré Structures Using Atomic Force Microscopy Ironing"
   Nano Lett. 2023, 23, 11, 4749–4755

2. Nikodem Sokolowski, **Swaroop Palai**, Mateusz Dyksik, Katarzyna Posmyk, Michał Baranowski, Alessandro Surrente, Duncan Maude, Felix Carrascoso, Onur Cakiroglu, Estrella Sanchez, Alina Schubert, Carmen Munuera, Takashi Taniguchi, Kenji Watanabe, Joakim Hagel, Samuel Brem, Andres Castellanos-Gomez, Ermin Malic and Paulina Plochocka
   "Twist-angle dependent dehybridization of momentum-indirect excitons in $MoSe_2/MoS_2$ heterostructures"
   Nikodem Sokolowski et al 2023 2D Mater. 10 034003

Other publications:

1. Jakub Jasiński, Joshua J P Thompson, **Swaroop Palai**, Maciej Śmietrka, Mateusz Dyksik, Takashi Taniguchi, Kenji Watanabe, Michał Baranowski, Duncan K Maude, Alessandro Surrente, Ermin Malic, and Paulina Plochocka
   "Control of the valley polarization of monolayer WSe_2 by Dexter-like coupling"
   Jakub Jasiński et al 2024 2D Mater. 11 025007

2. Andrzej Nowok, Mirosław Mączka, Anna Gągor, Maciej Ptak, Jan K. Zaręba, Daria Szewczyk, **Swaroop Palai**, and Adam Sieradzki
   "Low-Temperature Persistent Disorder and Lattice Dynamics in a Luminescent 1D Hybrid Lead Halide: Implications and Insights"
   Chem. Mater. 2024, 36, 13, 6588–6597

Appendix B

Résumé de la thèse en français

Dans cette annexe, nous présentons un résumé en français de ce travail de thèse. Le lecteur ne trouvera aucune nouvelle information et les figures utilisées sont les mêmes que dans la version anglaise.

B.1 Introduction

L'émergence des matériaux bidimensionnels (2D) a révolutionné le domaine des nanotechnologies. Depuis le succès du graphène, environ 150 matériaux 2D ont été explorés. Ces matériaux sont caractérisés par des couches faiblement liées par des interactions de van der Waals, ce qui permet de les exfolier mécaniquement en monocouches. Ils peuvent être métalliques (comme le borophène), semi-métalliques (comme le silicène), semi-conducteurs (comme les dichalcogénures de métaux de transition, TMDCs) ou isolants (comme le nitrure de bore hexagonal, hBN) [Geim 2007].

Les propriétés de ces matériaux peuvent être modulées en fonction du nombre de couches, en raison des effets de couplage inter-couches et de confinement quantique. Par exemple, le phosphore noir maintient un gap direct, qui passe du spectre infrarouge moyen en forme de vrac à la gamme visible en monocouches [Li 2014a]. Les TMDCs sont particulièrement intéressants pour leurs propriétés électriques et optiques uniques, et promettent de nouvelles applications dans la nanoélectronique, la détection à l'échelle nanométrique et la nanophotonique [Wang 2012].

B.2 Structure Cristalline et Propriétés Physiques

Les TMDCs, représentés par la formule MX_2 (où M est un métal et X un chalcogénure), possèdent une structure en couches avec des liaisons covalentes fortes dans chaque couche et des forces de van der Waals entre les couches. Les TMDCs du groupe VI, tels que MoS_2, $MoSe_2$, $MoTe_2$, WS_2 et WSe_2, sont particulièrement étudiés [Splendiani 2010].

B.2.1 Réseau Réciproque et Zone de Brillouin des Composés MX_2

Le réseau réciproque et la zone de Brillouin des composés MX_2 fournissent des informations cruciales sur les propriétés électroniques et les symétries du matériau. Les vecteurs du réseau réciproque sont construits à partir des vecteurs du réseau

direct et servent de base pour comprendre l'évolution des structures de bandes électroniques(Figure B.1).

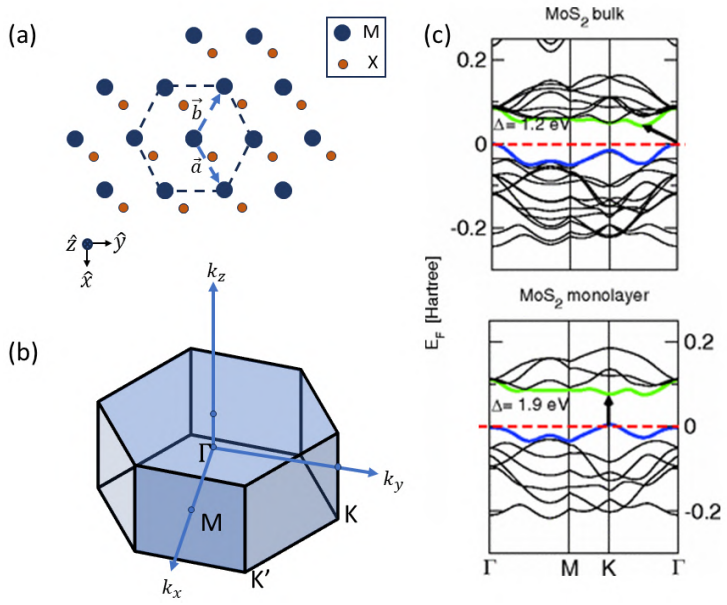

Figure B.1: (a) Vecteurs du réseau dans le plan. (b) Illustration de la zone de Brillouin avec les points de symétrie pour les composés 2H-MX_2. (c) Calculs de la structure de bande montrant les transitions indirectes au point Γ et les transitions directes au point K en monocouche [Kuc 2011].

B.3 Propriétés Optiques et Évolution de la Structure de Bande

Les TMDCs montrent une transition du gap indirect au gap direct lorsqu'ils passent de la forme en vrac à la monocouche. Cela a été démontré par des études théoriques et expérimentales, notamment par Mak et al. en 2010, qui ont rapporté un gap indirect de 1,29 eV pour le MoS_2 en vrac et un gap direct de 1,90 eV en monocouche [Mak 2010, Splendiani 2010](Figure B.2).

Les calculs de la structure de bande révèlent que les états électroniques participant à la transition indirecte au point Γ et à la transition directe au point K sont principalement composés d'orbitales d du métal et d'orbitales p du chalcogénure [Kuc 2011].

Les spectres de photoluminescence et de réflectance différentielle des flocons de MX_2 en monocouche sur des substrats de quartz montrent les transitions excitoniques A, B et C, qui sont associées aux effets de couplage spin-orbite dans la bande de valence et à la structure de bande [Kozawa 2014](Figure B.3).

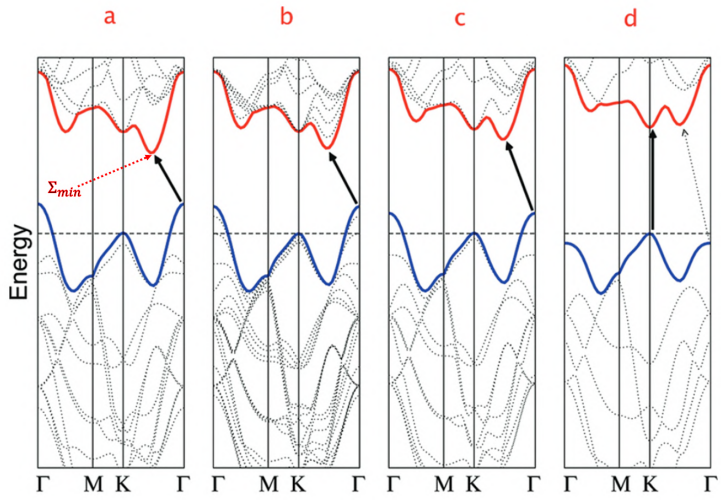

Figure B.2: Calculs de la structure de bande pour (a) MoS_2 en vrac, (b) MoS_2 à quatre couches, (c) MoS_2 à deux couches, et (d) MoS_2 en monocouche. Les flèches indiquent les transitions énergétiques les plus basses [Splendiani 2010].

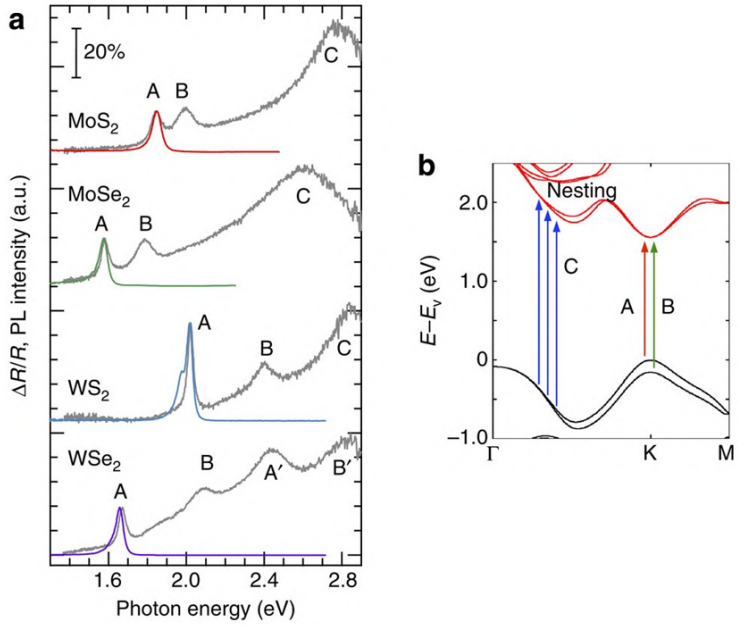

Figure B.3: (a) Spectres de PL et de réflectance différentielle des flocons de MX_2 en monocouche. (b) Structure de bande du MoS_2 en monocouche calculée par DFT, avec les transitions des excitons A et B indiquées par des flèches [Kozawa 2014].

B.4 Physique des Excitons

Les excitons, des quasi-particules formées par l'interaction entre un électron et un trou, jouent un rôle crucial dans la réponse optique des TMDCs en mono-

couche. Les excitons de type Frenkel sont des paires e^- et h^+ fortement liées, tandis que les excitons de type Wannier-Mott sont des paires e^- et h^+ faiblement liées [Wang 2012](Figure B.4).

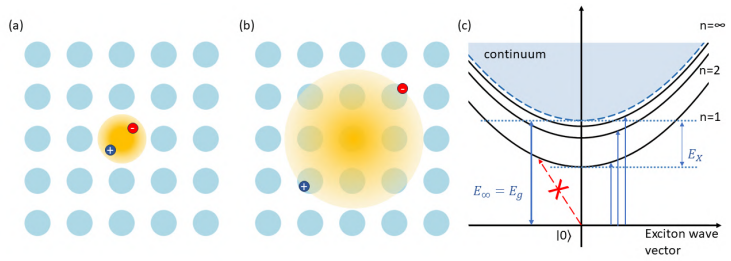

Figure B.4: (a) Excitons de type Frenkel et (b) Excitons de type Wannier-Mott.

Les excitons intralayer et interlayer dans les hétérostructures TMDC sont particulièrement intéressants pour leurs propriétés uniques. La modélisation des excitons en 2D permet de comprendre leur comportement dans ces systèmes [Rivera 2015].

B.5 Hétérostructures van der Waals (vdW)

Les hétérostructures vdW, formées par l'empilement de monocouches isolées de TMDCs, ouvrent de nouvelles perspectives de recherche en science des matériaux et en nanotechnologie. Ces constructions complexes, souvent appelées hétérostructures vdW, sont créées en empilant couche par couche dans une séquence choisie [Geim 2013].

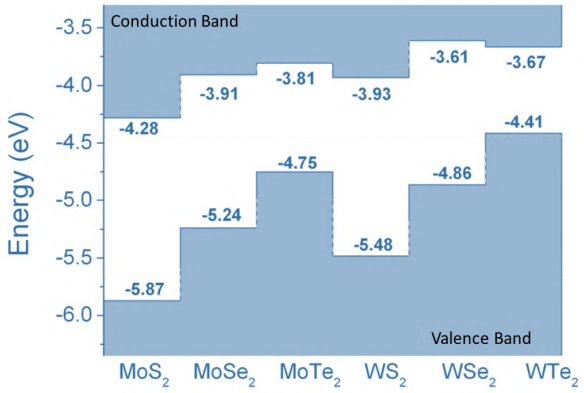

Figure B.5: Alignement des bandes des TMDCs calculé en utilisant les calculs Perdew-Burke-Ernzerhof (PBE). Alignement de bande de type-II où le CBM et le VBM résident dans des couches différentes [Kang 2013].

Les hétérostructures vdW permettent la réalisation d'excitons interlayer fortement liés et localisés, en raison de l'énergie de liaison des excitons significativement

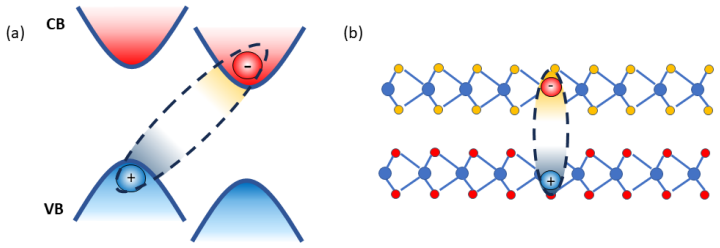

Figure B.6: Schémas montrant l'exciton interlayer en espace k et en espace réel avec les charges localisées dans deux couches différentes.

plus élevée dans les TMDCs 2D par rapport aux semi-conducteurs conventionnels comme le silicium ou le GaAs [Geim 2013].

Excitons Intercouches dans les Hétérostructures de Type-II

L'alignement des bandes dans les hétérostructures de TMDCs affecte de manière significative le comportement des états excités. Dans une configuration de type-II, le bas de la bande de conduction (CBM) d'une couche est plus bas que celui de l'autre couche, et le sommet de la bande de valence (VBM) de la première couche est plus haut que celui de l'autre couche. Cette disposition permet un transfert rapide des charges entre les couches, facilitant la création d'excitons intercouches (IX) et le maintien d'une polarisation de spin et de vallée durable dans les porteurs de charge. Les excitons intercouches sont fortement liés et localisés en raison de la grande énergie de liaison des excitons, qui peut atteindre des centaines de meV (Figure 1.9).

Les spectres de photoluminescence (PL) à basse température de WSe_2, $MoSe_2$ et des hétérostructures montrent l'émergence d'un pic IX à basse énergie, autour de 1.35 eV (Figure 1.10). L'observation initiale des IX a été rapportée dans un système $MoSe_2$-WSe_2 par Rivera et al. (2015), où ils ont noté que la durée de vie des IX est d'un ordre de grandeur plus longue que celle des excitons intralayer à 1.8 ns. Ils ont démontré que le transfert ultrarapide de porteurs de charge optiquement excités résulte en une accumulation d'électrons et de trous dans des couches séparées, formant des IX ([Hong 2014, Ceballos 2014]).

Des études ultérieures ont montré que l'amplitude de photocourant des excitons intercouches est environ 200 fois plus petite que celle des excitons intralayer, indiquant que la force oscillatrice des excitons intercouches est deux ordres de grandeur plus petite que celle des excitons intralayer ([Ross 2017]). En utilisant la spectroscopie pump-probe, Kim et al. ([Kim 2017]) ont montré que les trous polarisés en vallée sont générés en WSe_2 dans les 50 fs via un transfert de charge ultrarapide dans l'hétérostructure WSe_2/MoS_2 ([Hong 2014, Ceballos 2014]). Ces trous polarisés en vallée ont une durée de vie dépassant 1 µs et une durée de vie de dépolarisation de plus de 40 µs à 10 K. Wilson et al. ont également établi que l'énergie de liaison des IX est de 200 meV dans l'hétérostructure $MoSe_2/WSe_2$, ce qui est un ordre de

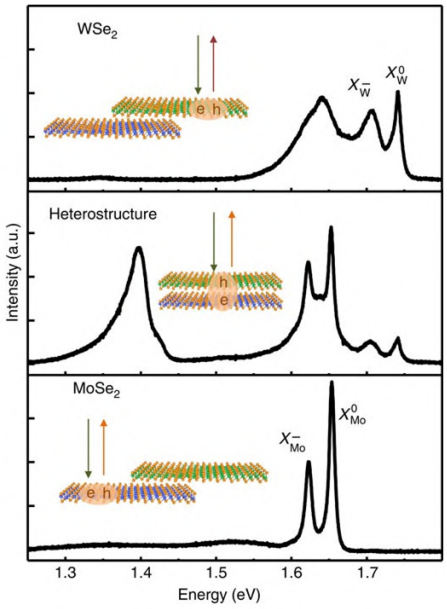

Figure B.7: Spectres de PL à basse température de WSe_2, $MoSe_2$ et des hétérostructures montrant l'émergence d'un pic IX à basse énergie, autour de 1.35 eV. Reproduit avec permission de [Rivera 2015] copyright (2024) de Springer Nature.

grandeur plus élevé que celle des structures de GaAs ([Wilson 2017]).

Formation de Motif Moiré

La formation d'un motif moiré se produit lorsque deux motifs périodiques se superposent avec des périodes ou des orientations légèrement différentes, produisant un nouveau motif qui varie lentement. Cette interférence peut mener à l'émergence de motifs à grande échelle, démontrant la sensibilité du motif moiré aux orientations relatives et à l'espacement des structures superposées (Figure 1.11).

Dans les couches TMDC bidimensionnelles, le motif moiré devient particulièrement significatif. Le premier motif moiré observé dans ces hétérostructures a été rapporté dans un système $MoSe_2/WSe_2$ aligné avec précision utilisant la microscopie STM ([Zhang 2017a]). La périodicité du motif moiré peut être ajustée, permettant de moduler les propriétés optoélectroniques des hétérostructures résultantes. La variation de l'arrangement atomique local à travers une supercellule moiré conduit à une variation de potentiel lentement changeante, connue sous le nom de potentiel moiré (Figure 1.12b).

Lorsque des couches TMDC périodiques sont empilées avec une légère torsion ou un décalage de réseau, l'interférence entre leurs structures atomiques génère un motif moiré (Figure 1.12a). Dans le contexte des super-réseaux moirés, les empilements parallèles près de 0° et les empilements antiparallèles près de 60° sont appelés empilements de type R et H, respectivement. Ces points symétriques représentent des extrêmes locaux (Figure 1.12b) dans le paysage énergétique où les excitons sont

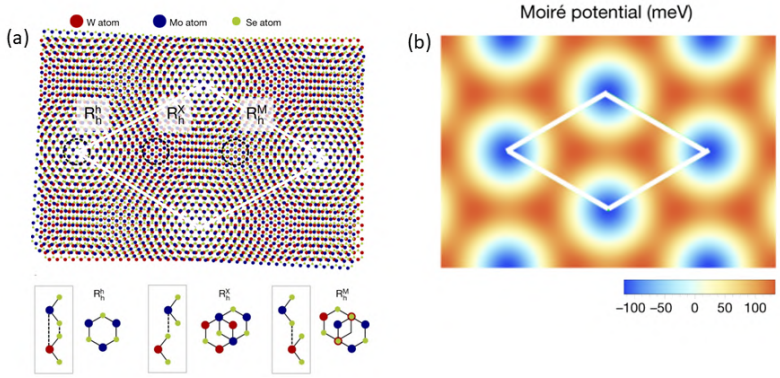

Figure B.8: (a) Alignements atomiques dans une hétérostructure $MoSe_2/WSe_2$ alignée. (b) Potentiel moiré pour la transition d'exciton intercouche, illustrant un minimum local au site R_h. Reproduit avec permission de [Tran 2019] copyright (2024) de Springer Nature.

confinés, imposant différentes règles de sélection optique spécifiques au site.

La profondeur du potentiel moiré dans une hétérostructure est déterminée par l'interaction intercouche. Les calculs de premiers principes estiment que le potentiel moiré est de l'ordre de 100-200 meV [Tran 2019]. Ce potentiel confine plusieurs résonances excitoniques IX (Figure 1.13a), ce qui a également été confirmé expérimentalement par STM sur une hétérostructure $MoSe_2/WSe_2$ cultivée par CVD [Zhang 2017a].

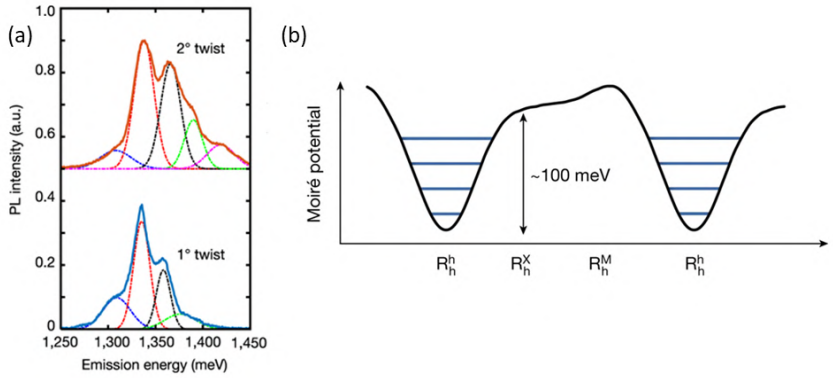

Figure B.9: (a) Spectres de PL des régions d'hétérostructure avec des angles de torsion de 2° (en haut) et 1° (en bas) ajustés avec des fonctions gaussiennes. (b) Schéma montrant la variation spatiale des potentiels moirés aux points symétriques de la supercellule confiant de multiples résonances excitoniques. Reproduit avec permission de [Tran 2019], copyright (2024) Springer Nature.

Hybridation Intercouche des États Électroniques

L'empilement de différentes couches TMDC permet de contrôler précisément les propriétés électroniques en fonction du choix des matériaux. L'empilement de monocouches TMDC conduit à une hybridation des états électroniques due au chevauchement des orbitales atomiques des couches participantes. Les orbitales d des atomes de métal de transition et les orbitales p des atomes de chalcogène jouent un rôle crucial dans cette hybridation [Splendiani 2010, Liu 2013]. Le couplage intercouche dans les hétérostructures TMDC provient du chevauchement des orbitales atomiques aux interfaces, affectant les états autour du point Γ dans la zone de Brillouin (Figure 1.14a).

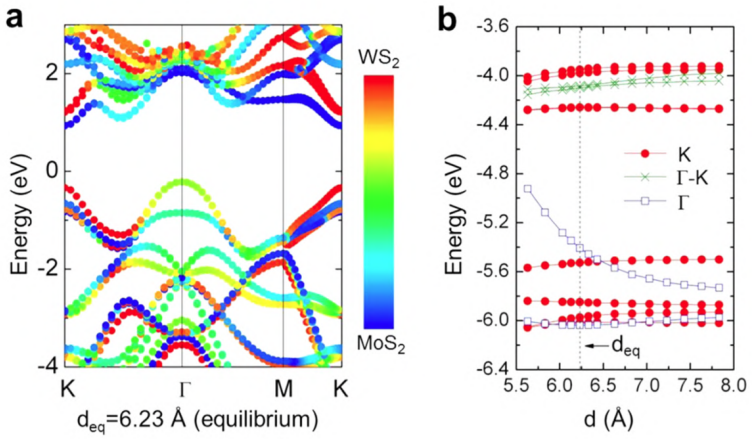

Figure B.10: (a) Calcul DFT illustrant la transition du gap indirect au gap direct dans une hétérostructure MoS_2/WS_2. (b) Les niveaux d'énergie des états de bande de bord en fonction de la distance intercouche d. Reproduit (adapté) avec permission de [Tongay 2014], copyright (2024) American Chemical Society.

Cette hybridation conduit à des effets significatifs sur les états orbitaux ([Kuc 2011, Raja 2018]). Les modèles de structure de bande montrent que dans les hétérostructures $MoSe_2/MoS_2$ et MoS_2/WS_2, la structure de bande est significativement affectée par l'hybridation intercouche ([Su 2016, Hagel 2021]). Cette hybridation place le VBM au point Γ et le CBM au point K de la zone de Brillouin, rendant les IX indirects à la fois en espace réel et en espace k.

La sensibilité du VBM au point Γ est attribuée à l'émission assistée par phonons, qui se déplace avec l'augmentation de l'annéaling thermique. En revanche, le pic de photoluminescence (PL) $P_{\text{hétéro}}$ à 1.95 eV est approximativement 200 meV en dessous du P_{WS_2}, indiquant une émission directe ([Wilson 2017]). Ces résultats démontrent que l'hybridation affecte fortement les bandes au point Γ mais la valence et la bande de conduction restent aux points K.

En conclusion, les études montrent que la distance intercouche influence la structure de bande et les propriétés optiques des IX dans les hétérostructures TMDC,

ouvrant ainsi des possibilités prometteuses pour des applications optoélectroniques avancées.

B.6 Repassage par Microscopie à Force Atomique (AFM) des Monocouches et Hétérostructures de TMDCs

B.6.1 Repassage par AFM de la Monocouche de MoS_2

Pour comprendre l'effet du repassage par AFM sur la morphologie de surface, une monocouche de MoS2 exfoliée sur un substrat hBN a été analysée. L'échantillon comprenait deux régions distinctes : l'une recouverte de hBN et l'autre une monocouche de MoS_2 non recouverte. Le repassage par AFM a été réalisé sur une zone de 10 µm par 10 µm en mode contact avec des forces allant de 5 nN à 400 nN. Des scans dynamiques AFM ont été effectués après le repassage pour évaluer les effets.

B.6.1.1 Identification des Régimes de Force de Repassage et Modifications de Surface

Pendant le processus de repassage, trois régimes de force distincts ont été identifiés :

Faible force (en dessous de 20 nN) : Les débris de surface et les adsorbats s'accumulent, formant des motifs ondulés. Ceux-ci sont visibles dans les images de friction mais diminuent lorsque les forces dépassent 30 nN.

Force intermédiaire (20-200 nN) : À mesure que la force augmente, les motifs ondulés diminuent et la surface commence à s'aplanir. La Figure B.11 illustre les images de force latérale pendant ce processus.

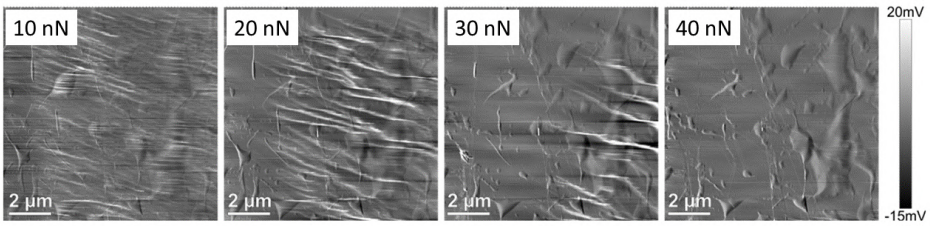

Figure B.11: Images de force latérale obtenues pendant le processus de repassage en mode contact, révélant une trace distincte laissée par les adsorbats de surface déplacés à faibles forces. Cette trace est particulièrement visible dans les images de friction mais diminue notablement pour des forces dépassant 30 nN.

Haute force (au-dessus de 200 nN) : La pointe AFM commence à endommager la couche supérieure, entraînant des caractéristiques de surface rompues et des couches supérieures endommagées comme le montre la Figure B.12.

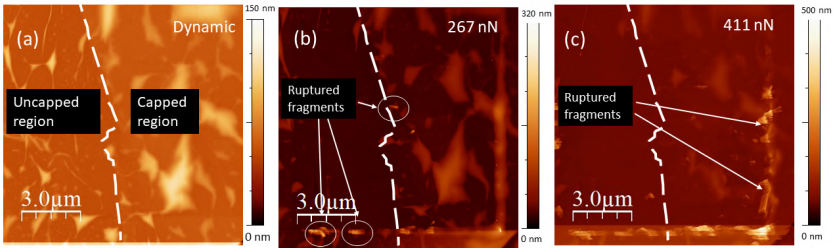

Figure B.12: (a) Montre le scan dynamique initial qui révèle les bulles et les plis présents. (b) Montre un scan à ∼ 267 nN, qui commence à montrer des morceaux de flocons rompus sur les bords. (c) Montre le scan final à ∼ 411 nN avec des caractéristiques de surface rompues et une couche supérieure endommagée.

B.6.1.2 Effets et Implications du Repassage sur la Surface et les Bulles

À des forces inférieures à 30 nN, les caractéristiques de surface telles que les bulles et les plis restent largement inchangées. Des changements significatifs ont été observés seulement à des forces supérieures à 30 nN, en particulier dans les régions non recouvertes de MoS_2. Les bulles plus grandes (dépassant 1 µm) montraient peu de changements, même à des forces plus élevées.

Rugosité de Surface : La rugosité moyenne quadratique (RMS) de la surface a été analysée avant et après le repassage (Figure B.13(d)). Les forces plus élevées ont aplati la surface et réduit la rugosité, mais les bulles plus grandes ont été simplement remodelées plutôt que supprimées (Figures B.13(e-g)).

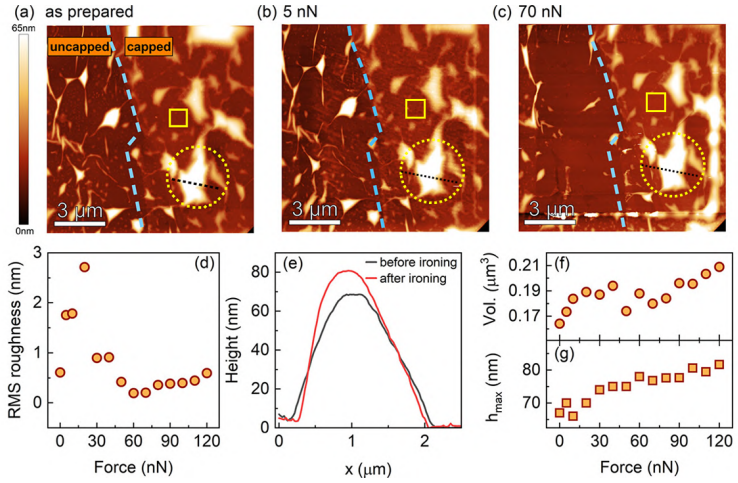

Figure B.13: (a-c) Montre des images AFM avant et après le repassage avec différentes forces. Le panneau (d) affiche le changement de la valeur RMS de la rugosité de surface avec les forces de repassage (à l'intérieur du carré jaune de 1µm2). (e) Montre le profil de hauteur d'une bulle (à l'intérieur du cercle jaune) avant et après le repassage. Les panneaux (f) et (g) montrent le volume et la hauteur de la bulle en fonction des forces de repassage.

B.6.2 Repassage par AFM des Hétérostructures $MoS_2/MoSe_2$

Les effets du repassage par AFM sur les hétérostructures $MoS_2/MoSe_2$ ont été examinés, en se concentrant sur des échantillons avec différents angles de torsion (type-H et type-R). Les échantillons A et B présentent un angle de torsion de 57,2° et 56,3° respectivement, tous deux de type II. Pour ces échantillons, les forces de repassage appliquées étaient de 30, 60, 80 nN pour l'échantillon A, et de 70 nN pour l'échantillon B. En revanche, l'échantillon C, de type R avec un angle de torsion de 1,3°, a été soumis à des forces de repassage de 10 et 100 nN.

Repassage par AFM de l'Échantillon A et B (type-H)

Processus de Repassage et Modifications de Surface : Les scans topographiques AFM de l'Échantillon A ont révélé une élimination significative des débris de surface et une amélioration de la planéité après un repassage avec des forces allant de 30 à 80 nN (Figure B.14). Des observations similaires ont été faites pour l'Échantillon B, repassé avec une force de 70 nN (Figure B.15).

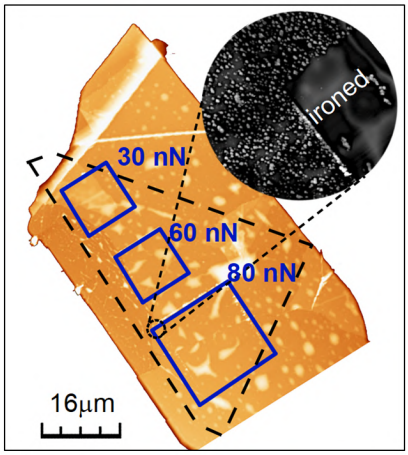

Figure B.14: Scan topographique AFM en mode dynamique de l'échantillon A montrant les régions soumises à des forces de repassage variables, avec une vue rapprochée de la zone repassée (80 nN) fournie dans l'encart.

Analyse de la Photoluminescence (PL) : L'analyse statistique des spectres de PL a indiqué une augmentation de l'intensité de PL dans les régions repassées, signifiant un meilleur contact entre les couches et une densité de bulles réduite (Figure B.16). Les spectres de PL ont montré un décalage vers le rouge de l'énergie de pic, une réduction de la largeur de raie et une augmentation de l'intensité après le repassage.

Processus de Repassage et Modification de Surface de l'Échantillon C (type-R)

Effets du Repassage : L'échantillon C, repassé avec des forces de 10 nN et 100 nN, a montré des différences distinctes. La force plus élevée a conduit à des changements plus visibles, y compris l'accumulation de débris et des variations de contraste de

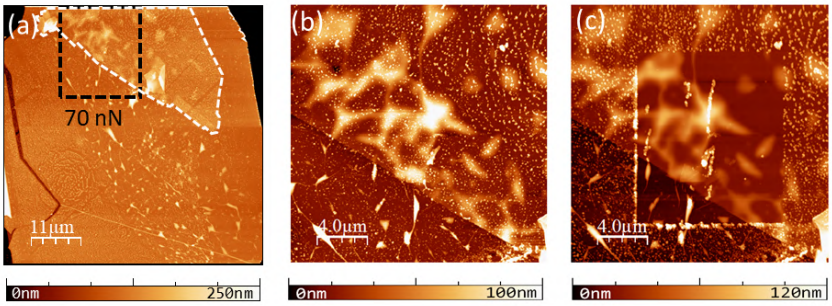

Figure B.15: (a) Illustre la topographie AFM de la zone d'hétérostructure sélectionnée avant le scan en mode contact. La ligne pointillée blanche indique la couche supérieure de hBN. (b,c) Montre la région avant et après le repassage, soulignant l'accumulation de débris aux bords sous une force de scan de 70 nN.

phase (Figure B.17). La cartographie de PL a révélé une augmentation de l'intensité et des changements dans la largeur de raie et l'énergie du pic d'émission IX dans la zone repassée à 100 nN (Figure B.18).

B.6.3 Analyse Statistique des Spectres de Photoluminescence

Pour valider les observations faites précédemment et obtenir des informations plus approfondies sur l'évolution des caractéristiques des excitons intercouches (IX), nous avons effectué une analyse statistique des spectres de photoluminescence mesurés à divers endroits sur l'hétérostructure des échantillons A et B. Les histogrammes présentés à la Figure B.19 illustrent la distribution de l'énergie de pic PL, de la largeur de raie et de l'intensité pour différentes forces utilisées lors du processus de repassage.

Le repassage induit un décalage vers le rouge de la transition IX, comme on peut le voir à la Figure B.19(a-c). Ce décalage semble être approximativement proportionnel à la force de repassage appliquée, avec un coefficient de -286±225 µeV/nN dérivé de l'ajustement montré à la Figure B.20(a).

À la Figure B.19(d-f), la distribution de la largeur de raie des spectres IX est présentée. La moyenne de l'élargissement de la ligne d'émission augmente avec un coefficient de 0.26 ± 0.07 µeV/nN, comme montré à la Figure B.20(b). Les barres d'erreur sur les graphiques représentent la variabilité des paramètres spectraux dérivés des mesures prises à différents points de l'échantillon. Cette incertitude provient principalement de l'inhomogénéité de l'échantillon. Cependant, la distribution se resserre après le repassage, comme en témoignent les histogrammes à la Figure B.19(d-f).

Les histogrammes de l'intensité intégrée, montrés à la Figure B.19(g-i), révèlent que l'intensité PL dans les régions repassées montre une augmentation moyenne d'environ 15% par rapport aux zones non repassées (comme montré à la Figure B.20(c)). Ces résultats sont cohérents avec l'idée d'un contact plus intime entre les

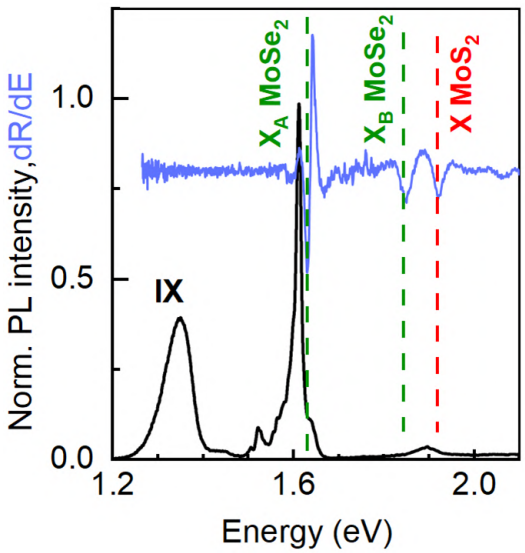

Figure B.16: Photoluminescence (en noir) et spectres de réflectance (en gris) acquis à 4.5 K de la région d'hétérostructure montrant les résonances d'excitons intercouches (IX) et intracouches, comme indiqué.

couches au sein des hétérostructures, résultant de la densité réduite de bulles après le traitement AFM.

Aperçus du Repassage des Trois Échantillons

Modifications de la Rugosité de Surface : Le repassage par AFM a significativement diminué la rugosité RMS des zones repassées, conduisant à une distribution plus uniforme des propriétés optiques (Figure B.21).

Modulation des Propriétés Optiques : Le repassage a non seulement modifié la surface mais a également significativement impacté les propriétés optiques des hétérostructures, conduisant à une diminution de l'écart-type de l'énergie IX, de la largeur de raie et de l'intensité, et améliorant l'uniformité et la performance globale des hétérostructures.

En résumé, le repassage par AFM améliore efficacement la planéité et l'uniformité des monocouches et des hétérostructures de TMDC. En optimisant les forces de repassage, des améliorations significatives de la morphologie de surface et des propriétés optiques peuvent être réalisées, faisant du repassage par AFM une technique post-fabrication précieuse pour les matériaux 2D.

B.7 Mesures Magneto-Optiques

Installation de Magnéto-Transmission dans notre Installation

L'installation que j'ai développée en interne avec l'assistance d'Andrzej Nowok et de l'équipe d'instrumentation aborde avec succès les problèmes que nous avons identi-

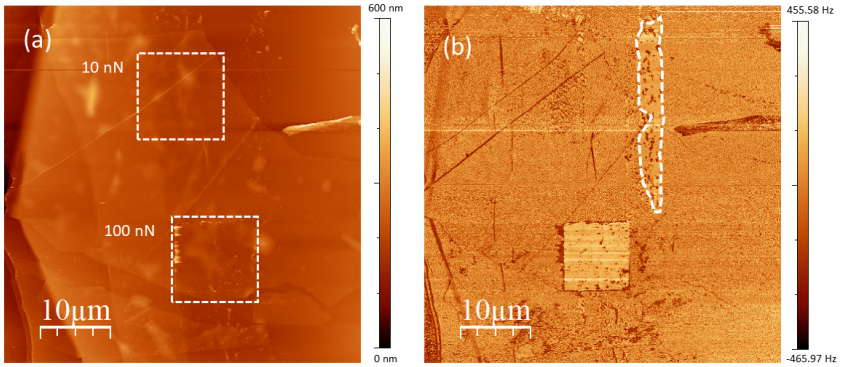

Figure B.17: (a) Image topographique AFM montrant les zones scannées avec 10 nN et 100 nN. (b) Scan de phase AFM montrant le changement de phase de la pointe de surface de l'échantillon.

fiés dans la section précédente. Les schémas de l'installation sont présentés dans la Figure B.22. Elle se compose de trois sections importantes, à savoir l'excitation et la détection en espace libre, la sonde de magnéto- transmission et la bobine résistive pour la génération de champs magnétiques pulsés.

Pour exciter l'échantillon sur un petit cœur de fibre de 10 µm, un arrangement spécial est mis en place. Comme le montre la Figure B.22, une source de lumière blanche est collimatée à l'aide d'un miroir parabolique hors axe (Thorlabs inc.) et ciblée sur un objectif microscopique super achromatique avec une ouverture numérique de 0,1 NA, pour correspondre à l'ouverture numérique de la fibre de 10 µm. Cela minimise la perte d'intensité due au surremplissage de la fibre d'injection. La fibre transmet ensuite la lumière incidente couplée à travers le flocon d'échantillon à l'extrémité de la fibre, à la pointe de la sonde.

La sonde de magnéto- transmission est ensuite soigneusement placée à l'intérieur du cryostat à hélium où la pointe de la sonde se trouve précisément au centre du champ magnétique à l'intérieur de l'alésage de la bobine résistive. Une fibre de collecte séparée recueille le signal transmis de l'échantillon au monochromateur. Deux lentilles sont utilisées avant le monochromateur, l'une pour collimater le signal et l'autre pour focaliser le signal sur le monochromateur. Dans les sections suivantes, nous discuterons de la conception et de l'optimisation de la sonde de magnéto- transmission et des aspects techniques de la bobine résistive utilisée pour la génération du champ magnétique.

Conception de notre sonde de magnéto- transmission

La sonde de magnéto- transmission discutée dans cette sous-section a été conçue, construite et optimisée par moi-même, en interne au LNCMI Toulouse avec l'aide de Sylvie George, Nicolas Bruyant et Noé Estorges de l'équipe d'instrumentation et Andrzej Nowok. Cette sonde, comme les autres dans l'installation, comporte deux parties principales en plus du corps. Le corps de la sonde abrite le tube en fibre

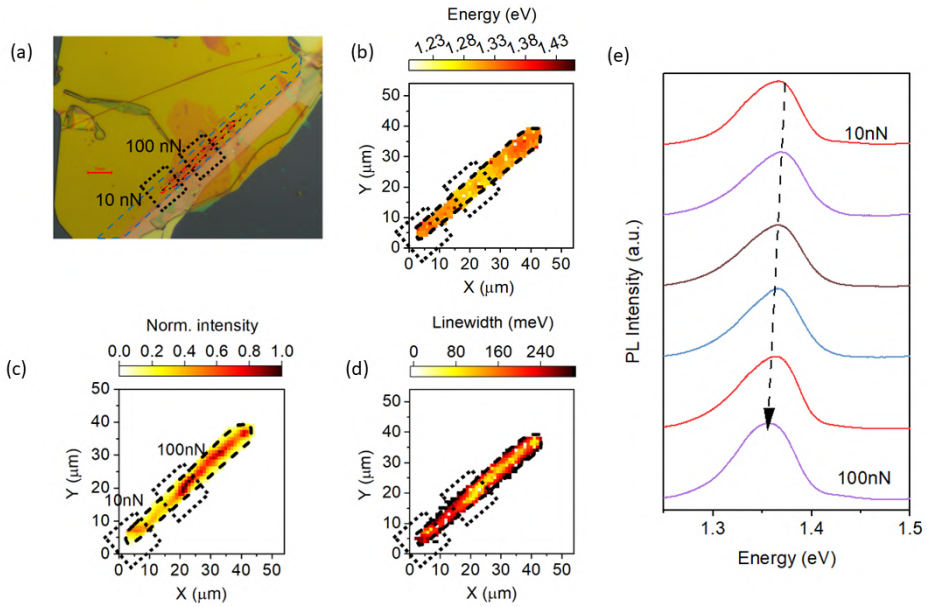

Figure B.18: (a) Micrographie de l'échantillon C, (b) cartes d'énergie, d'intensité normalisée (c), de largeur de raie (d), et (e) spectre de photoluminescence (PL) obtenus de l'échantillon.

de carbone et fournit un support structurel aux fibres optiques à l'intérieur de la sonde. Les autres parties sont la tête de la sonde et la pointe de la sonde.

Tête de sonde

La tête de la sonde abrite le manchon de connexion, qui relie la fibre d'échantillon à la fibre d'injection provenant d'une source lumineuse. Elle abrite également les connexions pour le contrôleur de température et la bobine de détection. La Figure B.23(a) montre une vue latérale en coupe transversale de la tête de la sonde de magnéto- transmission. La tête de la sonde présente deux ouvertures sécurisées par des vis compatibles sous vide, qui permettent aux fibres optiques d'entrer et de sortir de la sonde. La Figure B.23(b) montre l'intérieur de la tête de la sonde, y compris le connecteur DIN à 12 broches sur lequel des fils de 100 µm sont soudés pour le capteur de température et la bobine de détection. Deux fils supplémentaires sont également gardés en réserve en cas de défaillance de l'un des fils ou des connexions. Ces fils peuvent être soudés à l'endroit souhaité sans démonter toute la sonde.

Pointe de sonde

La pointe de la sonde, comme le montre la Figure B.24(a), a été conçue et développée par moi-même à l'aide d'une impression 3D précise avec l'aide de l'équipe d'instrumentation. Comme le montre la Figure B.24(a), elle contient à la fois le capteur de température cryogénique (Cernox de Lakeshore) et la bobine de détec-

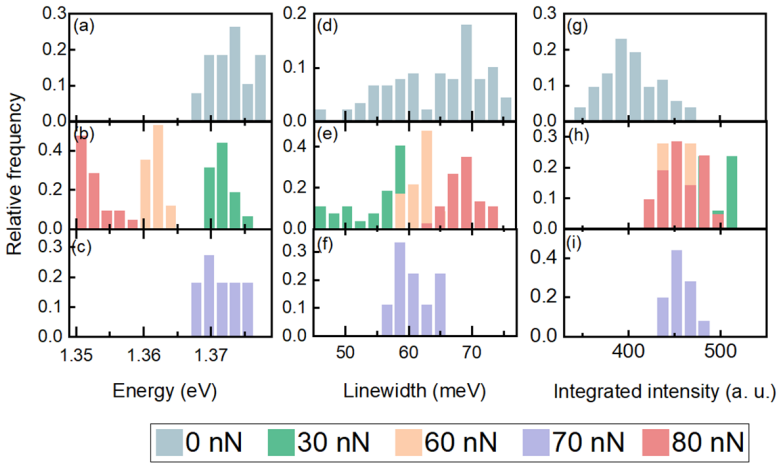

Figure B.19: Histogrammes montrant la distribution de (a-c) l'énergie PL, (d-f) la largeur de raie, et (g-i) l'intensité pour les régions non repassées et repassées dans l'hétérostructure des échantillons A (30, 60 et 80 nN) et B (70 nN).

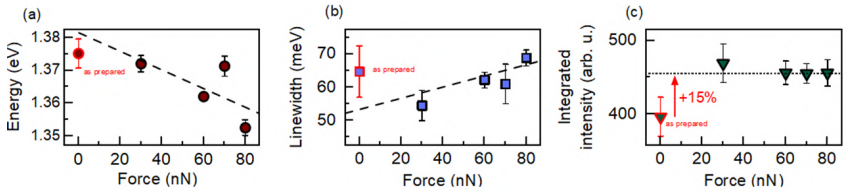

Figure B.20: Les graphiques illustrent les valeurs moyennes de l'énergie de transition IX (a), de la largeur de raie (b), et de l'intensité PL (c) en fonction de la force de repassage. Les lignes pointillées indiquent les ajustements linéaires dans (a-b).

tion. La Figure B.24(b) montre la section transversale de la pointe de la sonde, qui comporte des rainures pour contenir les lentilles de collimation, la lentille de focalisation, les miroirs, le polariseur et les fibres d'injection et de collecte. La lumière de la source se déplace le long du chemin incident (indiqué par la ligne pointillée orange dans la figure) à l'intérieur de la fibre d'échantillon. Elle transmet ensuite à travers l'échantillon, est collimatée par la lentille, réfléchie par deux miroirs à 45 degrés, et est ensuite focalisée dans la fibre de collecte. Enfin, la lumière est transmise au spectromètre pour analyse. Ces rainures nous aident à ajuster précisément la position des fibres par rapport aux lentilles pour obtenir un signal maximal.

Le capteur de température cryogénique mentionné plus tôt est un thermomètre à résistance à quatre bornes qui peut fonctionner à des températures extrêmement basses de l'hélium superfluide (2,17 K). La dépendance température-résistance peut varier pour différents capteurs Cernox. Le capteur utilisé dans cette sonde est particulièrement non calibré. Pour trouver cette dépendance, nous avons utilisé les valeurs de résistance fournies dans la fiche technique pour ce capteur de température particulier et interpolé tous les points entre les valeurs fournies.

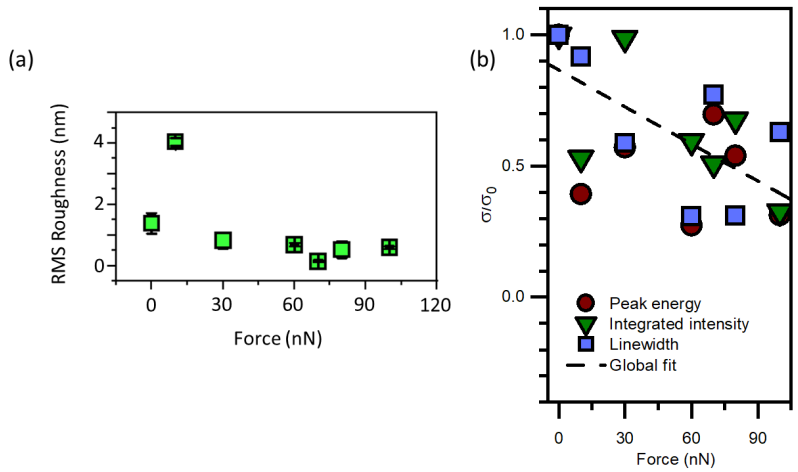

Figure B.21: (a) Le graphique montre le changement de la valeur RMS moyennée sur une zone de 1 nm2 à l'intérieur de la zone repassée. (b) Le graphique montre l'écart-type (σ) de l'énergie de transition IX, de la largeur de raie et de l'intensité PL normalisée à l'écart-type mesuré sur des zones non repassées (σ_0) en fonction de la force de repassage dérivée des trois échantillons discutés. La ligne pointillée représente l'ajustement linéaire global de l'écart-type relatif de tous les paramètres.

La bobine de détection à l'intérieur de la pointe de la sonde nous aide à surveiller le champ magnétique produit dans la bobine. Elle fonctionne sur le principe fondamental de l'induction électromagnétique de Faraday. La bobine de détection est composée de 10 boucles de fil de cuivre isolé de 100 µm de diamètre. Lorsqu'elle rencontre un changement de champ magnétique, elle induit une tension (V) dans la bobine pour contrecarrer le changement de champ magnétique.

Spectroscopie de Magnéto-Transmission de $(PEA)_2PbI_4$

Pour assurer le bon fonctionnement de l'installation et vérifier l'efficacité de tous les dispositifs, nous avons réalisé une spectroscopie de transmission sur l'iodure de plomb de phénéthylammonium (PEPI) sous l'influence d'un champ magnétique.

J'ai étudié l'influence du champ magnétique sur les spectres de transmission de PEPI dans la base de polarisation circulaire. La Figure B.25(a) présente les spectres de transmission du cristal de PEPI sous l'influence d'un champ magnétique, illustrant le décalage de l'absorption excitonique (1s) à 2,35 eV (montré dans l'encart de la Figure B.25(a)) et la caractéristique à haute énergie à 2,6 eV, correspondant à la bande interdite. Le petit décalage spectral induit par le champ magnétique externe est déterminé en calculant le rapport des spectres mesurés dans le champ magnétique au spectre à 0 T. Le spectre de rapport résultant, TB/T0, présente des caractéristiques nettes dont l'amplitude, la largeur et la position sont très sensibles au décalage d'énergie par rapport au spectre du champ 0 T. En supposant que le champ magnétique externe n'introduit qu'un décalage d'énergie tout en maintenant

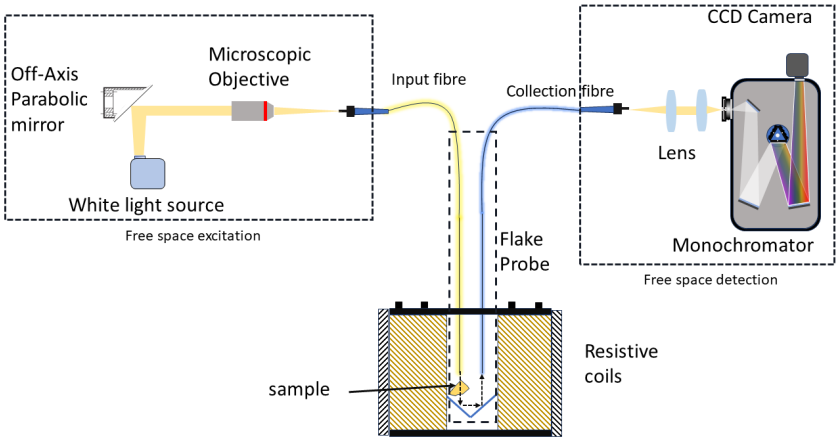

Figure B.22: Configuration expérimentale montrant la partie injection et la partie détection de la sonde de magnéto- transmission.

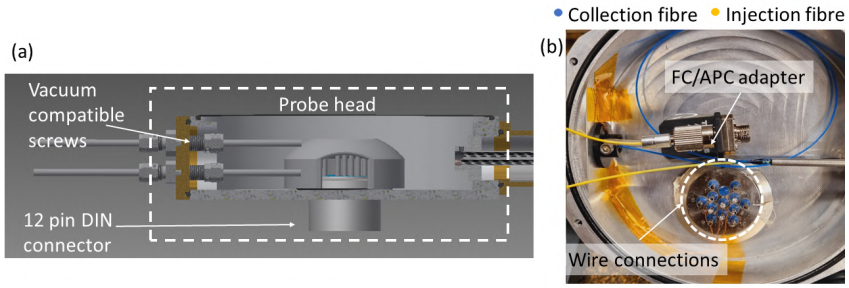

Figure B.23: (a) Vue en coupe transversale de la tête de la sonde depuis le côté. Elle montre les vis compatibles sous vide qui maintiennent les fibres entrant dans la tête de la sonde en place. (b) Montre l'intérieur de la tête de la sonde contenant l'adaptateur FC/APC, les connexions de fils pour le capteur de température et la bobine de détection, ainsi que les fibres d'injection et de collecte.

la forme globale du spectre, le spectre rapporté peut être représenté par $\frac{T_0+\delta E}{T_0}$, où δE est un paramètre d'ajustement indiquant le décalage d'énergie dû au champ magnétique. La Figure B.25(b) montre la ligne solide correspondant à l'ajustement obtenu par cette méthode. L'encart montre les spectres de transmission rapportés sur une plage plus large.

En mesurant dans les deux directions du champ magnétique, on accède aux états polarisés σ^+ et σ^-. Les décalages d'énergie pour les deux polarisations ont été déterminés à partir des spectres de transmission collectés de PEPI, et les branches séparées de Zeeman sont présentées dans la Figure B.25(c). Ce graphique montre que le décalage est différent pour les différentes polarisations. Le graphique montre que les branches σ^+ et σ^- présentent un décalage vers le bleu et le rouge respectivement. Le décalage non symétrique pour les polarisations résulte d'un coefficient diamagnétique non nul, c_0.

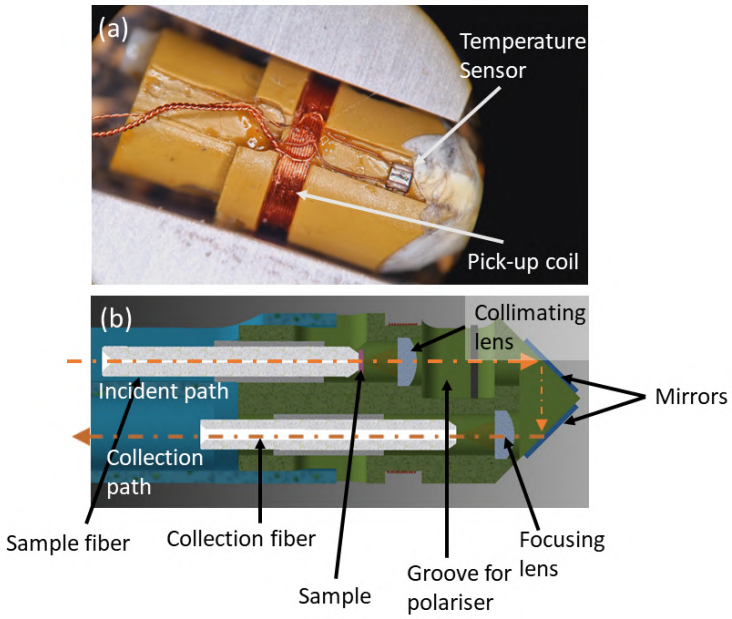

Figure B.24: (a) Vue agrandie de la pointe de la sonde (b) Coupe transversale de la pointe de la sonde montrant les différentes parties à l'intérieur. (Image CAD courtoisie de Sylvie George)

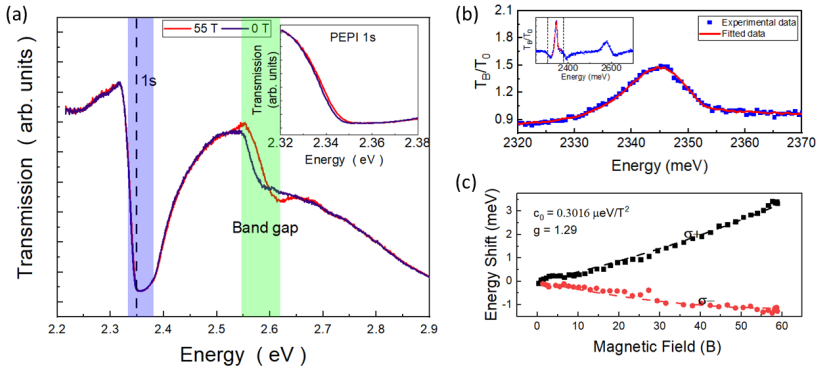

Figure B.25: (a) Spectres de transmission de PEPI collectés à 2K à 0 T et 55 T montrent un décalage visible dans la transition excitonique 1s (dans l'encart de la figure) et la bande interdite. (b) Spectres T_B/T_0 à la transition 1s ajustés par moindres carrés pour trouver le décalage d'énergie. (c) Graphique montrant le décalage d'énergie pour les deux polarisations avec les valeurs de décalage calculées à partir de l'ajustement.

Le décalage diamagnétique, c_0, a été extrait en ajustant les points de données à l'équation suivante :

$$\delta E_{\sigma\pm} = \pm\frac{1}{2}g\mu_B B + c_0\frac{1}{2}B^2$$

En résumé, l'installation et les mesures réalisées démontrent l'efficacité de la sonde de magnéto- transmission et permettent une analyse détaillée des effets magnétiques sur les matériaux 2D comme PEPI. Ces résultats montrent l'importance des champs magnétiques pour moduler les propriétés optiques de ces matériaux, ouvrant la voie à des applications potentielles dans l'optoélectronique de nouvelle génération.

Bibliography

[Aivazian 2015] Grant Aivazian, Zhirui Gong, Aaron M Jones, Rui-Lin Chu, Jiaqiang Yan, David G Mandrus, Chuanwei Zhang, David Cobden, Wang Yao and Xiaodong Xu. *Magnetic control of valley pseudospin in monolayer WSe 2.* Nature Physics, vol. 11, no. 2, pages 148–152, 2015. (Cited on page 66.)

[Andersen 2021] Trond I Andersen, Giovanni Scuri, Andrey Sushko, Kristiaan De Greve, Jiho Sung, You Zhou, Dominik S Wild, Ryan J Gelly, Hoseok Heo, Damien Bérubé*et al.* *Excitons in a reconstructed moiré potential in twisted WSe2/WSe2 homobilayers.* Nature materials, vol. 20, no. 4, pages 480–487, 2021. (Cited on page 17.)

[Arora 2015] Ashish Arora, Maciej Koperski, Karol Nogajewski, Jacques Marcus, Clément Faugeras and Marek Potemski. *Excitonic resonances in thin films of WSe 2: from monolayer to bulk material.* Nanoscale, vol. 7, no. 23, pages 10421–10429, 2015. (Cited on page 27.)

[Asahina 1983] Hideo Asahina, Yusei Maruyama and Akira Morita. *Optical reflectivity and band structure of black phosphorus.* Physica B+C, vol. 117-118, pages 419–421, 1983. (Cited on page 1.)

[Baranowski 2017] Michal Baranowski, Alessandro Surrente, L Klopotowski, Joanna M Urban, Nan Zhang, Duncan K Maude, Kamil Wiwatowski, Sebastian Mackowski, Yen-Cheng Kung, Dumitru Dumcenco*et al.* *Probing the interlayer exciton physics in a MoS2/MoSe2/MoS2 van der Waals heterostructure.* Nano letters, vol. 17, no. 10, pages 6360–6365, 2017. (Cited on page 53.)

[Baranowski 2019] Michał Baranowski, Krzysztof Galkowski, Alessandro Surrente, Joanna Urban, Łukasz Kłopotowski, Sebastian Maćkowski, Duncan Kennedy Maude, Rim Ben Aich, Kais Boujdaria, Maria Chamarro*et al.* *Giant fine structure splitting of the bright exciton in a bulk MAPbBr3 single crystal.* Nano Letters, vol. 19, no. 10, pages 7054–7061, 2019. (Cited on page 83.)

[Bastante 2023] Pablo Bastante, Thomas Pucher and Andres Castellanos-Gomez. *Finding a cost-effective optical system to identify 2D materials*, April 2023. (Cited on pages 29 and 31.)

[Bernardi 2013] Marco Bernardi, Maurizia Palummo and Jeffrey C Grossman. *Extraordinary sunlight absorption and one nanometer thick photovoltaics using two-dimensional monolayer materials.* Nano letters, vol. 13, no. 8, pages 3664–3670, 2013. (Cited on page 14.)

[Brem 2020] Samuel Brem, Kai-Qiang Lin, Roland Gillen, Jonas M Bauer, Janina Maultzsch, John M Lupton and Ermin Malic. *Hybridized intervalley moiré excitons and flat bands in twisted WSe 2 bilayers.* Nanoscale, vol. 12, no. 20, pages 11088–11094, 2020. (Cited on page 61.)

[Britnell 2012] Liam Britnell, RV Gorbachev, Rashid Jalil, BD Belle, Fredrik Schedin, Artem Mishchenko, Thanasis Georgiou, MI Katsnelson, Laurence Eaves, SV Morozov*et al. Field-effect tunneling transistor based on vertical graphene heterostructures.* Science, vol. 335, no. 6071, pages 947–950, 2012. (Cited on page 14.)

[Britnell 2013a] L Britnell, RV Gorbachev, AK Geim, LA Ponomarenko, A Mishchenko, MT Greenaway, TM Fromhold, KS Novoselov and Laurence Eaves. *Resonant tunnelling and negative differential conductance in graphene transistors.* Nature communications, vol. 4, no. 1, page 1794, 2013. (Cited on page 14.)

[Britnell 2013b] Liam Britnell, Ricardo Mendes Ribeiro, Axel Eckmann, Rashid Jalil, Branson D Belle, Artem Mishchenko, Y-J Kim, Roman V Gorbachev, Thanasis Georgiou, Sergei V Morozov*et al. Strong light-matter interactions in heterostructures of atomically thin films.* Science, vol. 340, no. 6138, pages 1311–1314, 2013. (Cited on page 23.)

[Bromley 1972] RA Bromley, Ray B Murray and Abe D Yoffe. *The band structures of some transition metal dichalcogenides. III. Group VIA: trigonal prism materials.* Journal of Physics C: Solid State Physics, vol. 5, no. 7, page 759, 1972. (Cited on page 5.)

[Bui 2022] Hoa Thi Bui, Do Chi Linh, Lam Duc Nguyen, HyungIl Chang, Supriya A Patil, Nabeen K Shrestha, Khuyen Xuan Bui, Tung Son Bui, Thi Ngoc Anh Nguyen, Nguyen Thanh Tung*et al. In-situ formation and integration of graphene into MoS2 interlayer spacing: expansion of interlayer spacing for superior hydrogen evolution reaction in acidic and alkaline electrolyte.* Journal of Materials Science, vol. 57, no. 40, pages 18993–19005, 2022. (Cited on page 2.)

[Cadiz 2017] Fabian Cadiz, Emmanuel Courtade, Cédric Robert, Gang Wang, Yuxia Shen, Hui Cai, Takashi Taniguchi, Kenji Watanabe, Helene Carrere, Delphine Lagarde*et al. Excitonic linewidth approaching the homogeneous limit in MoS 2-based van der Waals heterostructures.* Physical Review X, vol. 7, no. 2, page 021026, 2017. (Cited on pages 14, 23 and 53.)

[Carvalho 2013] A Carvalho, RM Ribeiro and AH Castro Neto. *Band nesting and the optical response of two-dimensional semiconducting transition metal dichalcogenides.* Physical Review B—Condensed Matter and Materials Physics, vol. 88, no. 11, page 115205, 2013. (Cited on page 8.)

[Castellanos-Gomez 2013] Andres Castellanos-Gomez, Rafael Roldán, Emmanuele Cappelluti, Michele Buscema, Francisco Guinea, Herre SJ Van Der Zant and Gary A Steele. *Local strain engineering in atomically thin MoS2.* Nano letters, vol. 13, no. 11, pages 5361–5366, 2013. (Cited on page 26.)

[Castellanos-Gomez 2014] Andres Castellanos-Gomez, Leonardo Vicarelli, Elsa Prada, Joshua O Island, KL Narasimha-Acharya, Sofya I Blanter, Dirk J Groenendijk, Michele Buscema, Gary A Steele, JV Alvarez*et al.* *Isolation and characterization of few-layer black phosphorus.* 2D Materials, vol. 1, no. 2, page 025001, 2014. (Cited on page 1.)

[Ceballos 2014] Frank Ceballos, Matthew Z Bellus, Hsin-Ying Chiu and Hui Zhao. *Ultrafast charge separation and indirect exciton formation in a MoS2–MoSe2 van der Waals heterostructure.* ACS nano, vol. 8, no. 12, pages 12717–12724, 2014. (Cited on pages 16 and 93.)

[Cheiwchanchamnangij 2012] Tawinan Cheiwchanchamnangij and Walter RL Lambrecht. *Quasiparticle band structure calculation of monolayer, bilayer, and bulk MoS 2.* Physical Review B, vol. 85, no. 20, page 205302, 2012. (Cited on pages 6 and 8.)

[Chen 2021] Sihan Chen, Jangyup Son, Siyuan Huang, Kenji Watanabe, Takashi Taniguchi, Rashid Bashir, Arend M Van Der Zande and William P King. *Tip-based cleaning and smoothing improves performance in monolayer MoS2 devices.* ACS omega, vol. 6, no. 5, pages 4013–4021, 2021. (Cited on pages 47 and 48.)

[Chernikov 2014] Alexey Chernikov, Timothy C. Berkelbach, Heather M. Hill, Albert Rigosi, Yilei Li, Burak Aslan, David R. Reichman, Mark S. Hybertsen and Tony F. Heinz. *Exciton Binding Energy and Nonhydrogenic Rydberg Series in Monolayer* WS_2. Phys. Rev. Lett., vol. 113, page 076802, Aug 2014. (Cited on pages 12 and 13.)

[Chiu 2015] Ming-Hui Chiu, Chendong Zhang, Hung-Wei Shiu, Chih-Piao Chuu, Chang-Hsiao Chen, Chih-Yuan S Chang, Chia-Hao Chen, Mei-Yin Chou, Chih-Kang Shih and Lain-Jong Li. *Determination of band alignment in the single-layer MoS2/WSe2 heterojunction.* Nature communications, vol. 6, no. 1, page 7666, 2015. (Cited on page 14.)

[Choi 2021] Junho Choi, Matthias Florian, Alexander Steinhoff, Daniel Erben, Kha Tran, Dong Seob Kim, Liuyang Sun, Jiamin Quan, Robert Claassen, Somak Majumder*et al.* *Twist angle-dependent interlayer exciton lifetimes in van der Waals heterostructures.* Physical Review Letters, vol. 126, no. 4, page 047401, 2021. (Cited on page 21.)

[Coehoorn 1987] R Coehoorn, C Haas and RA De Groot. *Electronic structure of MoSe 2, MoS 2, and WSe 2. II. The nature of the optical band gaps.* Physical Review B, vol. 35, no. 12, page 6203, 1987. (Cited on pages 2, 6, 8 and 37.)

[Dean 2010] Cory R Dean, Andrea F Young, Inanc Meric, Chris Lee, Lei Wang, Sebastian Sorgenfrei, Kenji Watanabe, Takashi Taniguchi, Phillip Kim, Kenneth L Shepard*et al. Boron nitride substrates for high-quality graphene electronics.* Nature nanotechnology, vol. 5, no. 10, pages 722–726, 2010. (Cited on page 23.)

[Dhakal 2014] Krishna P Dhakal, Dinh Loc Duong, Jubok Lee, Honggi Nam, Minsu Kim, Min Kan, Young Hee Lee and Jeongyong Kim. *Confocal absorption spectral imaging of MoS 2: optical transitions depending on the atomic thickness of intrinsic and chemically doped MoS 2.* Nanoscale, vol. 6, no. 21, pages 13028–13035, 2014. (Cited on page 27.)

[Dickinson 1923] Roscoe G Dickinson and Linus Pauling. *The crystal structure of molybdenite.* Journal of the American Chemical Society, vol. 45, no. 6, pages 1466–1471, 1923. (Cited on page 2.)

[Duong 2017] Dinh Loc Duong, Seok Joon Yun and Young Hee Lee. *van der Waals layered materials: opportunities and challenges.* ACS nano, vol. 11, no. 12, pages 11803–11830, 2017. (Cited on page 1.)

[Dyksik 2020] Mateusz Dyksik, Herman Duim, Xiangzhou Zhu, Zhuo Yang, Masaki Gen, Yoshimitsu Kohama, Sampson Adjokatse, Duncan K Maude, Maria Antonietta Loi, David A Egger*et al. Broad tunability of carrier effective masses in two-dimensional halide perovskites.* ACS Energy Letters, vol. 5, no. 11, pages 3609–3616, 2020. (Cited on page 83.)

[Falin 2017] Aleksey Falin, Qiran Cai, Elton JG Santos, Declan Scullion, Dong Qian, Rui Zhang, Zhi Yang, Shaoming Huang, Kenji Watanabe, Takashi Taniguchi*et al. Mechanical properties of atomically thin boron nitride and the role of interlayer interactions.* Nature communications, vol. 8, no. 1, page 15815, 2017. (Cited on page 46.)

[Fox 2010] Mark Fox. Optical properties of solids, volume 3. Oxford university press, 2010. (Cited on page 11.)

[Frisenda 2017] Riccardo Frisenda, Yue Niu, Patricia Gant, Aday J Molina-Mendoza, Robert Schmidt, Rudolf Bratschitsch, Jinxin Liu, Lei Fu, Dumitru Dumcenco, Andras Kis*et al. Micro-reflectance and transmittance spectroscopy: a versatile and powerful tool to characterize 2D materials.* Journal of Physics D: Applied Physics, vol. 50, no. 7, page 074002, 2017. (Cited on page 25.)

[Fuhr 1999] J. D. Fuhr, J. O. Sofo and Andrés Saúl. *Adsorption of Pd on* $MoS_2(1000)$ *: Ab initio electronic-structure calculations.* Phys. Rev. B, vol. 60, pages 8343–8347, Sep 1999. (Cited on page 7.)

[Gasparutti 2020] Isabella Gasparutti, Seung Hyun Song, Michael Neumann, Xu Wei, Kenji Watanabe, Takashi Taniguchi and Young Hee Lee. *How*

clean is clean? Recipes for van der Waals heterostructure cleanliness assessment. ACS applied materials & interfaces, vol. 12, no. 6, pages 7701–7709, 2020. (Cited on pages 34, 47 and 48.)

[Geim 2007] Andre K Geim and Konstantin S Novoselov. *The rise of graphene.* Nature materials, vol. 6, no. 3, pages 183–191, 2007. (Cited on pages 1 and 89.)

[Geim 2013] Andre K Geim and Irina V Grigorieva. *Van der Waals heterostructures.* Nature, vol. 499, no. 7459, pages 419–425, 2013. (Cited on pages 14, 92 and 93.)

[Gillen 2018] Roland Gillen and Janina Maultzsch. *Interlayer excitons in MoSe 2/WSe 2 heterostructures from first principles.* Physical Review B, vol. 97, no. 16, page 165306, 2018. (Cited on page 19.)

[Goossens 2012] AM Goossens, VE Calado, A Barreiro, K Watanabe, T Taniguchi and LMK Vandersypen. *Mechanical cleaning of graphene.* Applied Physics Letters, vol. 100, no. 7, 2012. (Cited on page 35.)

[Gupta 2017] Garima Gupta, Sangeeth Kallatt and Kausik Majumdar. *Direct observation of giant binding energy modulation of exciton complexes in monolayer MoS e 2.* Physical Review B, vol. 96, no. 8, page 081403, 2017. (Cited on page 12.)

[Hagel 2021] Joakim Hagel, Samuel Brem, Christopher Linderälv, Paul Erhart and Ermin Malic. *Exciton landscape in van der Waals heterostructures.* Physical Review Research, vol. 3, no. 4, page 043217, 2021. (Cited on pages 20, 21 and 96.)

[Haley 2021] Kristine L Haley, Jeffrey A Cloninger, Kayla Cerminara, Randy M Sterbentz, Takashi Taniguchi, Kenji Watanabe and Joshua O Island. *Heated assembly and transfer of van der Waals heterostructures with common nail polish.* Nanomanufacturing, vol. 1, no. 1, pages 49–56, 2021. (Cited on page 28.)

[Herlach 1995] Fritz Herlach and Jos AAJ Perenboom. *Magnet laboratory facilities worldwide—An update.* Physica B: Condensed Matter, vol. 211, no. 1-4, pages 1–16, 1995. (Cited on page 69.)

[Hong 2014] Xiaoping Hong, Jonghwan Kim, Su-Fei Shi, Yu Zhang, Chenhao Jin, Yinghui Sun, Sefaattin Tongay, Junqiao Wu, Yanfeng Zhang and Feng Wang. *Ultrafast charge transfer in atomically thin MoS2/WS2 heterostructures.* Nature nanotechnology, vol. 9, no. 9, pages 682–686, 2014. (Cited on pages 16 and 93.)

[Horcas 2007] Ignacio Horcas, Rs Fernández, JM Gomez-Rodriguez, JWSX Colchero, JWSXM Gómez-Herrero and AM Baro. *WSXM: A software for*

scanning probe microscopy and a tool for nanotechnology. Review of scientific instruments, vol. 78, no. 1, 2007. (Cited on page 35.)

[Howland 1996] Rebecca Howland and Lisa Benatar. *A Practical Guide: To Scanning Probe Microscopy.* 1996. (Cited on pages 41 and 43.)

[Huang 2022] Di Huang, Junho Choi, Chih-Kang Shih and Xiaoqin Li. *Excitons in semiconductor moiré superlattices.* Nature nanotechnology, vol. 17, no. 3, pages 227–238, 2022. (Cited on page 17.)

[Johnson 1987] Kenneth Langstreth Johnson and Kenneth Langstreth Johnson. Contact mechanics. Cambridge university press, 1987. (Cited on page 46.)

[Jung 2019] Younghun Jung, Min Sup Choi, Ankur Nipane, Abhinandan Borah, Bumho Kim, Amirali Zangiabadi, Takashi Taniguchi, Kenji Watanabe, Won Jong Yoo, James Hone*et al. Transferred via contacts as a platform for ideal two-dimensional transistors.* Nature Electronics, vol. 2, no. 5, pages 187–194, 2019. (Cited on page 35.)

[Jung 2021] E. Jung, Jin Cheol Park, Yu-Seong Seo, Ji-Hee Kim, Jungseek Hwang and Young Hee Lee. *Unusually large exciton binding energy in multilayered 2H-MoTe2.* Scientific Reports, vol. 12, 2021. (Cited on page 12.)

[Kang 2013] Jun Kang, Sefaattin Tongay, Jian Zhou, Jingbo Li and Junqiao Wu. *Band offsets and heterostructures of two-dimensional semiconductors.* Applied Physics Letters, vol. 102, no. 1, 2013. (Cited on pages 14, 15 and 92.)

[Keldysh 1979] Keldysh. *Coulomb interaction in thin semiconductor and semimetal films.* Soviet Journal of Experimental and Theoretical Physics, vol. 29, page 658, 1979. (Cited on page 12.)

[Keyes 1953] Robert W Keyes. *The electrical properties of black phosphorus.* Physical Review, vol. 92, no. 3, page 580, 1953. (Cited on page 1.)

[Kheng 1993] K Kheng, RT Cox, Merle Y d'Aubigné, Franck Bassani, K Saminadayar and S Tatarenko. *Observation of negatively charged excitons X- in semiconductor quantum wells.* Physical review letters, vol. 71, no. 11, page 1752, 1993. (Cited on page 37.)

[Kim 2017] Jonghwan Kim, Chenhao Jin, Bin Chen, Hui Cai, Tao Zhao, Puiyee Lee, Salman Kahn, Kenji Watanabe, Takashi Taniguchi, Sefaattin Tongay*et al. Observation of ultralong valley lifetime in WSe2/MoS2 heterostructures.* Science advances, vol. 3, no. 7, page e1700518, 2017. (Cited on pages 16 and 93.)

[Kim 2019] Youngwook Kim, Patrick Herlinger, Takashi Taniguchi, Kenji Watanabe and Jurgen H Smet. *Reliable postprocessing improvement of van der Waals heterostructures.* ACS nano, vol. 13, no. 12, pages 14182–14190, 2019. (Cited on pages 35, 48 and 50.)

[Kinney 1996] JH Kinney, M Balooch, SJ Marshall, GW Marshall Jr and TP Weihs. *Atomic force microscope measurements of the hardness and elasticity of peritubular and intertubular human dentin.* 1996. (Cited on page 41.)

[Ko 2016] Kyung Yong Ko, Jeong-Gyu Song, Youngjun Kim, Taejin Choi, Sera Shin, Chang Wan Lee, Kyounghoon Lee, Jahyun Koo, Hoonkyung Lee, Jongbaeg Kim*et al. Improvement of gas-sensing performance of large-area tungsten disulfide nanosheets by surface functionalization.* ACS nano, vol. 10, no. 10, pages 9287–9296, 2016. (Cited on page 2.)

[Kolobov 2016] Alexander V Kolobov and Junji Tominaga. Two-dimensional transition-metal dichalcogenides, volume 239. Springer, 2016. (Cited on page 3.)

[Kośmider 2013] Krzysztof Kośmider and Joaquın Fernández-Rossier. *Electronic properties of the MoS 2-WS 2 heterojunction.* Physical Review B, vol. 87, no. 7, page 075451, 2013. (Cited on page 14.)

[Kozawa 2014] Daichi Kozawa, Rajeev Kumar, Alexandra Carvalho, Kiran Kumar Amara, Weijie Zhao, Shunfeng Wang, Minglin Toh, Ricardo M Ribeiro, Antonio H Castro Neto, Kazunari Matsuda*et al. Photocarrier relaxation pathway in two-dimensional semiconducting transition metal dichalcogenides.* Nature communications, vol. 5, no. 1, page 4543, 2014. (Cited on pages 8, 90 and 91.)

[Krasnok 2018] Alex Krasnok, Sergey Lepeshov and Andrea Alú. *Nanophotonics with 2D transition metal dichalcogenides.* Optics express, vol. 26, no. 12, pages 15972–15994, 2018. (Cited on page 2.)

[Kretinin 2014] Andrey V Kretinin, Yuan Cao, Jhih-Sian Tu, GL Yu, Rashid Jalil, Konstantin S Novoselov, Sarah J Haigh, Ali Gholinia, Artem Mishchenko, Marcelo Lozada*et al. Electronic properties of graphene encapsulated with different two-dimensional atomic crystals.* Nano letters, vol. 14, no. 6, pages 3270–3276, 2014. (Cited on page 35.)

[Kuc 2011] Agnieszka Kuc, Nourdine Zibouche and Thomas Heine. *Influence of quantum confinement on the electronic structure of the transition metal sulfide T S 2.* Physical review B, vol. 83, no. 24, page 245213, 2011. (Cited on pages 4, 20, 90 and 96.)

[Kuc 2015] Agnieszka Kuc and Thomas Heine. *The electronic structure calculations of two-dimensional transition-metal dichalcogenides in the presence of external electric and magnetic fields.* Chemical Society Reviews, vol. 44, no. 9, pages 2603–2614, 2015. (Cited on pages 3 and 7.)

[Li 2014a] Siying Li, Wei Tang, Xiaoli Xu, Motao Cao, Yizheng Jin and Xiaojun Guo. *Comparative study of encapsulated solution-processed zinc oxide*

ultraviolet photodetectors with different contacts. physica status solidi (a), vol. 211, no. 9, pages 2184–2188, 2014. (Cited on pages 26 and 89.)

[Li 2014b] Yilei Li, Jonathan Ludwig, Tony Low, Alexey Chernikov, Xu Cui, Ghidewon Arefe, Young Duck Kim, Arend M Van Der Zande, Albert Rigosi, Heather M Hill*et al.* *Valley splitting and polarization by the Zeeman effect in monolayer MoSe 2*. Physical review letters, vol. 113, no. 26, page 266804, 2014. (Cited on page 66.)

[Liu 2013] Gui-Bin Liu, Wen-Yu Shan, Yugui Yao, Wang Yao and Di Xiao. *Three-band tight-binding model for monolayers of group-VIB transition metal dichalcogenides*. Physical Review B, vol. 88, no. 8, page 085433, 2013. (Cited on pages 7, 20 and 96.)

[Liu 2017] Bilu Liu, Ahmad Abbas and Chongwu Zhou. *Two-dimensional semiconductors: from materials preparation to electronic applications*. Advanced Electronic Materials, vol. 3, no. 7, page 1700045, 2017. (Cited on page 2.)

[LNCMP-team 2004] The LNCMP-team. *The LNCMP: a pulsed-field user-facility in Toulouse*. Physica B: Condensed Matter, vol. 346-347, pages 668–672, 2004. Proceedings of the 7th International Symposium on Research in High Magnetic Fields. (Cited on page 78.)

[Mahatha 2012] SK Mahatha, KD Patel and Krishnakumar SR Menon. *Electronic structure investigation of MoS2 and MoSe2 using angle-resolved photoemission spectroscopy and ab initio band structure studies*. Journal of Physics: Condensed Matter, vol. 24, no. 47, page 475504, 2012. (Cited on page 7.)

[Mak 2010] Kin Fai Mak, Changgu Lee, James Hone, Jie Shan and Tony F Heinz. *Atomically thin MoS 2: a new direct-gap semiconductor*. Physical review letters, vol. 105, no. 13, page 136805, 2010. (Cited on pages 2, 6, 27 and 90.)

[Mak 2022] Kin Fai Mak and Jie Shan. *Semiconductor moiré materials*. Nature Nanotechnology, vol. 17, no. 7, pages 686–695, 2022. (Cited on page 17.)

[Manzeli 2017] Sajedeh Manzeli, Dmitry Ovchinnikov, Diego Pasquier, Oleg V Yazyev and Andras Kis. *2D transition metal dichalcogenides*. Nature Reviews Materials, vol. 2, no. 8, pages 1–15, 2017. (Cited on page 2.)

[Mouri 2017] Shinichiro Mouri, Wenjing Zhang, Daichi Kozawa, Yuhei Miyauchi, Goki Eda and Kazunari Matsuda. *Thermal dissociation of inter-layer excitons in MoS 2/MoSe 2 hetero-bilayers*. Nanoscale, vol. 9, no. 20, pages 6674–6679, 2017. (Cited on page 53.)

[Niu 2018] Yue Niu, Sergio Gonzalez-Abad, Riccardo Frisenda, Philipp Marauhn, Matthias Drüppel, Patricia Gant, Robert Schmidt, Najme S Taghavi, David

Barcons, Aday J Molina-Mendoza*et al. Thickness-dependent differential reflectance spectra of monolayer and few-layer MoS2, MoSe2, WS2 and WSe2.* Nanomaterials, vol. 8, no. 9, page 725, 2018. (Cited on pages 26, 27 and 28.)

[Novoselov 2005] Kostya S Novoselov, Da Jiang, F Schedin, TJ Booth, VV Khotkevich, SV Morozov and Andre K Geim. *Two-dimensional atomic crystals.* Proceedings of the National Academy of Sciences, vol. 102, no. 30, pages 10451–10453, 2005. (Cited on page 1.)

[Novoselov 2012] Konstantin S Novoselov, Luca Colombo, PR Gellert, MG Schwab, KAJN Kim*et al. A roadmap for graphene.* nature, vol. 490, no. 7419, pages 192–200, 2012. (Cited on page 1.)

[Palai 2023] Swaroop Kumar Palai, Mateusz Dyksik, Nikodem Sokolowski, Mariusz Ciorga, Estrella Sánchez Viso, Yong Xie, Alina Schubert, Takashi Taniguchi, Kenji Watanabe, Duncan K Maude*et al. Approaching the Intrinsic Properties of Moiré Structures Using Atomic Force Microscopy Ironing.* Nano Letters, vol. 23, no. 11, pages 4749–4755, 2023. (Cited on page 54.)

[Park 2018] Soohyung Park, N. Mutz, T. Schultz, S. Blumstengel, A. Han, A. Aljarb, Lain-Jong Li, E. List-Kratochvil, P. Amsalem and N. Koch. *Direct determination of monolayer MoS2 and WSe2 exciton binding energies on insulating and metallic substrates.* 2D Materials, vol. 5, 2018. (Cited on page 12.)

[Pelant 2012] Ivan Pelant and Jan Valenta. Luminescence Spectroscopy of Semiconductors. Oxford University Press, 02 2012. (Cited on page 9.)

[Prada 2015] Elsa Prada, JV Alvarez, KL Narasimha-Acharya, FJ Bailen and JJ Palacios. *Effective-mass theory for the anisotropic exciton in two-dimensional crystals: Application to phosphorene.* Physical Review B, vol. 91, no. 24, page 245421, 2015. (Cited on page 13.)

[Radisavljevic 2011] Branimir Radisavljevic, Aleksandra Radenovic, Jacopo Brivio, Valentina Giacometti and Andras Kis. *Single-layer MoS2 transistors.* Nature nanotechnology, vol. 6, no. 3, pages 147–150, 2011. (Cited on page 3.)

[Raja 2018] Archana Raja, Malte Selig, Gunnar Berghauser, Jaeeun Yu, Heather M Hill, Albert F Rigosi, Louis E Brus, Andreas Knorr, Tony F Heinz, Ermin Malic*et al. Enhancement of exciton–phonon scattering from monolayer to bilayer WS2.* Nano letters, vol. 18, no. 10, pages 6135–6143, 2018. (Cited on pages 20 and 96.)

[Ramasubramaniam 2012] Ashwin Ramasubramaniam. *Large excitonic effects in monolayers of molybdenum and tungsten dichalcogenides.* Physical Review B, vol. 86, no. 11, page 115409, 2012. (Cited on page 9.)

[Rebollo 2021] IG Rebollo, FC Rodrigues-Machado, W Wright, GJ Melin and AR Champagne. *Thin-suspended 2D materials: facile, versatile, and deterministic transfer assembly.* 2D Materials, vol. 8, no. 3, page 035028, 2021. (Cited on page 28.)

[Ribeiro-Palau 2018] Rebeca Ribeiro-Palau, Changjian Zhang, Kenji Watanabe, Takashi Taniguchi, James Hone and Cory R Dean. *Twistable electronics with dynamically rotatable heterostructures.* Science, vol. 361, no. 6403, pages 690–693, 2018. (Cited on page 17.)

[Rivera 2015] Pasqual Rivera, John R Schaibley, Aaron M Jones, Jason S Ross, Sanfeng Wu, Grant Aivazian, Philip Klement, Kyle Seyler, Genevieve Clark, Nirmal J Ghimire*et al. Observation of long-lived interlayer excitons in monolayer MoSe2–WSe2 heterostructures.* Nature communications, vol. 6, no. 1, page 6242, 2015. (Cited on pages 16, 92 and 94.)

[Rosenberger 2018] Matthew R Rosenberger, Hsun-Jen Chuang, Kathleen M McCreary, Aubrey T Hanbicki, Saujan V Sivaram and Berend T Jonker. *Nano-"squeegee" for the creation of clean 2D material interfaces.* ACS applied materials & interfaces, vol. 10, no. 12, pages 10379–10387, 2018. (Cited on pages 34, 35 and 47.)

[Ross 2013] Jason S Ross, Sanfeng Wu, Hongyi Yu, Nirmal J Ghimire, Aaron M Jones, Grant Aivazian, Jiaqiang Yan, David G Mandrus, Di Xiao, Wang Yao*et al. Electrical control of neutral and charged excitons in a monolayer semiconductor.* Nature communications, vol. 4, no. 1, page 1474, 2013. (Cited on pages 37 and 53.)

[Ross 2017] Jason S Ross, Pasqual Rivera, John Schaibley, Eric Lee-Wong, Hongyi Yu, Takashi Taniguchi, Kenji Watanabe, Jiaqiang Yan, David Mandrus, David Cobden*et al. Interlayer exciton optoelectronics in a 2D heterostructure p–n junction.* Nano letters, vol. 17, no. 2, pages 638–643, 2017. (Cited on pages 16 and 93.)

[Rytova 2018] Natalia S Rytova. *Screened potential of a point charge in a thin film.* arXiv preprint arXiv:1806.00976, 2018. (Cited on page 12.)

[Sader 1999] John E Sader, James WM Chon and Paul Mulvaney. *Calibration of rectangular atomic force microscope cantilevers.* Review of scientific instruments, vol. 70, no. 10, pages 3967–3969, 1999. (Cited on page 35.)

[Shree 2018] S. Shree, M. A. Semina, C. Robert, B. Han, T. Amand, A. Balocchi, M. Manca, E. Courtade, X. Marie, T. Taniguchi, K. Watanabe, M. Glazov and B. Urbaszek. *Observation of exciton-phonon coupling in MoSe2 monolayers.* Physical Review B, 2018. (Cited on page 53.)

[Singh 2007] Jasprit Singh. Electronic and optoelectronic properties of semiconductor structures. Cambridge University Press, 2007. (Cited on page 10.)

[Sokołowski 2023] Nikodem Sokołowski, Swaroop Palai, Mateusz Dyksik, Katarzyna Posmyk, Michał Baranowskki, Alessandro Surrente, Duncan K Maude, Felix Carrascoso, Onur Cakiroglu, Estrella Sánchez-Viso*et al.* *Twist-angle dependent dehybridization of momentum-indirect excitons in MoSe2/MoS2 heterostructures.* 2D Materials, 2023. (Cited on pages 17, 32 and 61.)

[Splendiani 2010] Andrea Splendiani, Liang Sun, Yuanbo Zhang, Tianshu Li, Jonghwan Kim, Chi-Yung Chim, Giulia Galli and Feng Wang. *Emerging photoluminescence in monolayer MoS2.* Nano letters, vol. 10, no. 4, pages 1271–1275, 2010. (Cited on pages 2, 6, 7, 20, 27, 89, 90, 91 and 96.)

[Stier 2016] Andreas V Stier, Nathan P Wilson, Genevieve Clark, Xiaodong Xu and Scott A Crooker. *Probing the influence of dielectric environment on excitons in monolayer WSe2: insight from high magnetic fields.* Nano letters, vol. 16, no. 11, pages 7054–7060, 2016. (Cited on pages 66 and 67.)

[Su 2016] Xiangying Su, Weiwei Ju, Ruizhi Zhang, Chongfeng Guo, Jiming Zheng, Yongliang Yong and Xiaohong Li. *Bandgap engineering of MoS 2/MX 2 (MX 2= WS 2, MoSe 2 and WSe 2) heterobilayers subjected to biaxial strain and normal compressive strain.* RSC advances, vol. 6, no. 22, pages 18319–18325, 2016. (Cited on pages 20, 61 and 96.)

[Surrente 2018] Alessandro Surrente, Łukasz Kłopotowski, Nan Zhang, Michal Baranowski, Anatolie A Mitioglu, Mariana V Ballottin, Peter CM Christianen, Dumitru Dumcenco, Yen-Cheng Kung, Duncan K Maude*et al.* *Intervalley scattering of interlayer excitons in a mos2/mose2/mos2 heterostructure in high magnetic field.* Nano letters, vol. 18, no. 6, pages 3994–4000, 2018. (Cited on page 53.)

[Terrones 2013] Humberto Terrones, Florentino López-Urías and Mauricio Terrones. *Novel hetero-layered materials with tunable direct band gaps by sandwiching different metal disulfides and diselenides.* Scientific reports, vol. 3, no. 1, page 1549, 2013. (Cited on page 14.)

[Timoshenko 1959] Stephen Timoshenko, Sergius Woinowsky-Krieger*et al.* Theory of plates and shells, volume 2. McGraw-hill New York, 1959. (Cited on page 40.)

[Tongay 2013] Sefaattin Tongay, Jian Zhou, Can Ataca, Jonathan Liu, Jeong Seuk Kang, Tyler S Matthews, Long You, Jingbo Li, Jeffrey C Grossman and Junqiao Wu. *Broad-range modulation of light emission in two-dimensional semiconductors by molecular physisorption gating.* Nano letters, vol. 13, no. 6, pages 2831–2836, 2013. (Cited on page 23.)

[Tongay 2014] Sefaattin Tongay, Wen Fan, Jun Kang, Joonsuk Park, Unsal Koldemir, Joonki Suh, Deepa S Narang, Kai Liu, Jie Ji, Jingbo Li*et al.*

Tuning interlayer coupling in large-area heterostructures with CVD-grown MoS2 and WS2 monolayers. Nano letters, vol. 14, no. 6, pages 3185–3190, 2014. (Cited on pages 20, 21 and 96.)

[Tran 2014] Vy Tran, Ryan Soklaski, Yufeng Liang and Li Yang. *Layer-controlled band gap and anisotropic excitons in few-layer black phosphorus.* Physical Review B, vol. 89, no. 23, page 235319, 2014. (Cited on page 1.)

[Tran 2019] Kha Tran, Galan Moody, Fengcheng Wu, Xiaobo Lu, Junho Choi, Kyounghwan Kim, Amritesh Rai, Daniel A Sanchez, Jiamin Quan, Akshay Singh*et al. Evidence for moiré excitons in van der Waals heterostructures.* Nature, vol. 567, no. 7746, pages 71–75, 2019. (Cited on pages 18, 19, 61, 63 and 95.)

[Wang 2012] Qing Hua Wang, Kourosh Kalantar-Zadeh, Andras Kis, Jonathan N Coleman and Michael S Strano. *Electronics and optoelectronics of two-dimensional transition metal dichalcogenides.* Nature nanotechnology, vol. 7, no. 11, pages 699–712, 2012. (Cited on pages 2, 89 and 92.)

[Wang 2021] Lude Wang, Duo Xu, Lianfu Jiang, Jie Gao, Zhongmin Tang, Yunjie Xu, Xiang Chen and Han Zhang. *Transition metal dichalcogenides for sensing and oncotherapy: status, challenges, and perspective.* Advanced Functional Materials, vol. 31, no. 5, page 2004408, 2021. (Cited on page 2.)

[Wilson 2017] Neil R Wilson, Paul V Nguyen, Kyle Seyler, Pasqual Rivera, Alexander J Marsden, Zachary PL Laker, Gabriel C Constantinescu, Viktor Kandyba, Alexei Barinov, Nicholas DM Hine*et al. Determination of band offsets, hybridization, and exciton binding in 2D semiconductor heterostructures.* Science advances, vol. 3, no. 2, page e1601832, 2017. (Cited on pages 14, 16, 21, 94 and 96.)

[Withers 2015] Freddie Withers, Osvaldo Del Pozo-Zamudio, Artem Mishchenko, Aiden P Rooney, Ali Gholinia, K Watanabe, Takashi Taniguchi, Sarah J Haigh, AK Geim, AI Tartakovskii*et al. Light-emitting diodes by band-structure engineering in van der Waals heterostructures.* Nature materials, vol. 14, no. 3, pages 301–306, 2015. (Cited on page 14.)

[Wu 2018] Fengcheng Wu, Timothy Lovorn and AH MacDonald. *Theory of optical absorption by interlayer excitons in transition metal dichalcogenide heterobilayers.* Physical Review B, vol. 97, no. 3, page 035306, 2018. (Cited on pages 17, 61 and 63.)

[Xia 2014] Fengnian Xia, Han Wang, Di Xiao, Madan Dubey and Ashwin Ramasubramaniam. *Two-dimensional material nanophotonics.* Nature photonics, vol. 8, no. 12, pages 899–907, 2014. (Cited on page 2.)

[Xiao 2012] Di Xiao, Gui-Bin Liu, Wanxiang Feng, Xiaodong Xu and Wang Yao. *Coupled spin and valley physics in monolayers of MoS 2 and other group-VI*

dichalcogenides. Physical review letters, vol. 108, no. 19, page 196802, 2012. (Cited on page 8.)

[Ye 2014] Ziliang Ye, Ting Cao, Kevin O'brien, Hanyu Zhu, Xiaobo Yin, Yuan Wang, Steven G Louie and Xiang Zhang. *Probing excitonic dark states in single-layer tungsten disulphide*. Nature, vol. 513, no. 7517, pages 214–218, 2014. (Cited on page 12.)

[Yu 2015] Hongyi Yu, Yong Wang, Qingjun Tong, Xiaodong Xu and Wang Yao. *Anomalous light cones and valley optical selection rules of interlayer excitons in twisted heterobilayers*. Physical review letters, vol. 115, no. 18, page 187002, 2015. (Cited on page 18.)

[Yu 2017a] Hongyi Yu, Gui-Bin Liu, Jianju Tang, Xiaodong Xu and Wang Yao. *Moiré excitons: From programmable quantum emitter arrays to spin-orbit–coupled artificial lattices*. Science advances, vol. 3, no. 11, page e1701696, 2017. (Cited on pages 18, 19 and 61.)

[Yu 2017b] Zhihao Yu, Zhun-Yong Ong, Songlin Li, Jian-Bin Xu, Gang Zhang, Yong-Wei Zhang, Yi Shi and Xinran Wang. *Analyzing the carrier mobility in transition-metal dichalcogenide MoS2 field-effect transistors*. Advanced Functional Materials, vol. 27, no. 19, page 1604093, 2017. (Cited on page 34.)

[Zaslow 1967] B Zaslow and Melvin E Zandler. *Two-dimensional analog to the hydrogen atom*. American Journal of Physics, vol. 35, no. 12, pages 1118–1119, 1967. (Cited on page 11.)

[Zhang 2017a] Chendong Zhang, Chih-Piao Chuu, Xibiao Ren, Ming-Yang Li, Lain-Jong Li, Chuanhong Jin, Mei-Yin Chou and Chih-Kang Shih. *Interlayer couplings, Moiré patterns, and 2D electronic superlattices in MoS2/WSe2 hetero-bilayers*. Science advances, vol. 3, no. 1, page e1601459, 2017. (Cited on pages 17, 18, 94 and 95.)

[Zhang 2017b] Xiao-Xiao Zhang, Ting Cao, Zhengguang Lu, Yu-Chuan Lin, Fan Zhang, Ying Wang, Zhiqiang Li, James C Hone, Joshua A Robinson, Dmitry Smirnov*et al.* *Magnetic brightening and control of dark excitons in monolayer WSe2*. Nature nanotechnology, vol. 12, no. 9, pages 883–888, 2017. (Cited on pages 66 and 67.)

[Zhang 2018] Nan Zhang, Alessandro Surrente, Michał Baranowski, Duncan K Maude, Patricia Gant, Andres Castellanos-Gomez and Paulina Plochocka. *Moiré intralayer excitons in a MoSe2/MoS2 heterostructure*. Nano letters, vol. 18, no. 12, pages 7651–7657, 2018. (Cited on page 53.)

[Zhao 2013] Weijie Zhao, Zohreh Ghorannevis, Leiqiang Chu, Minglin Toh, Christian Kloc, Ping-Heng Tan and Goki Eda. *Evolution of electronic structure in atomically thin sheets of WS2 and WSe2*. ACS nano, vol. 7, no. 1, pages 791–797, 2013. (Cited on page 27.)

[Zhu 2011] Zhiyong Y Zhu, Yingchun C Cheng and Udo Schwingenschlögl. *Giant spin-orbit-induced spin splitting in two-dimensional transition-metal dichalcogenide semiconductors.* Physical Review B, vol. 84, no. 15, page 153402, 2011. (Cited on page 7.)

[Zhu 2014] Bairen Zhu, Xi Chen and X. Cui. *Exciton Binding Energy of Monolayer WS2.* Scientific Reports, vol. 5, 2014. (Cited on page 12.)

RÉPUBLIQUE FRANÇAISE
Liberté Égalité Fraternité

Université de Toulouse

Titre : Étude des propriétés structurelles et optiques des hétérostructures de TMDC en utilisant le 'ironing' par microscopie à force atomique.

Mots clés : hétérostructures, intercalaires excitons, AFM Ironing,

Résumé : Les progrès récents dans l'étude des matériaux bidimensionnels (2D), en particulier les dichalcogénures de métaux de transition (TMDCs), ont révélé des propriétés remarquables et des applications potentielles. Les TMDCs, tels que le MoS_2 et le $MoSe_2$, sont connus pour leurs caractéristiques électroniques et optiques uniques, qui peuvent être finement ajustées par exfoliation mécanique et empilement précis en hétérostructures. Des analyses expérimentales et théoriques ont démontré que ces matériaux à gap indirect acquièrent un gap direct au point K de la zone de Brillouin lorsqu'ils sont exfoliés en leur forme de monocouche. Dans cette thèse, nous discutons du développement et de l'optimisation d'une technique de fabrication novatrice utilisant du vernis à ongles, comprenant les processus d'exfoliation, de caractérisation et d'assemblage en hétérostructures de TMDCs encapsulés par du nitrure de bore hexagonal (hBN) en utilisant un tampon de vernis à ongles.

Une grande partie de cette recherche est dédiée à la technique post-fabrication connue sous le nom de repassage par microscopie à force atomique (AFM). Dans le Chapitre 3, nous explorons l'application de cette méthode pour améliorer l'état de surface et l'uniformité des monocouches de TMDC et de leurs hétérostructures. Le processus de repassage AFM réduit efficacement la rugosité de la surface et atténue l'hétérogénéité inter-couche, améliorant ainsi les propriétés optiques des matériaux. Dans notre étude, nous investiguons la physique des excitons dans ces matériaux 2D, en utilisant la spectroscopie de photoluminescence (PL) en régime stationnaire. Les résultats démontrent que le repassage AFM non seulement améliore la qualité structurelle des hétérostructures mais influence également de manière significative les transitions excitoniques, la largeur des raies et les intensités, conduisant à des caractéristiques de photoluminescence améliorées.

Dans le Chapitre 4, cette thèse présente le développement et l'utilisation d'une sonde de magnéto-transmission dédiée à l'étude des flocons. Cet appareil expérimental novateur, synchronisé avec une bobine résistive et un système cryogénique, permet l'étude précise des propriétés électroniques des hétérostructures TMDC sous différents champs magnétiques. Ces mesures fournissent des informations cruciales sur le comportement optique des matériaux 2D en réalisant une preuve de concept sur le plomb iodure de phénéthylammonium 2D (PEPI).

Grâce à une combinaison de techniques expérimentales, incluant la caractérisation AFM et la spectroscopie optique, cette étude offre des aperçus complets sur les propriétés fondamentales et les applications potentielles des hétérostructures TMDC. Les résultats permettent une meilleure compréhension des matériaux 2D et ouvrent la voie à leur utilisation dans des dispositifs nanoélectroniques et optoélectroniques avancés.

Title: Exploring Structural and Optical Properties of TMDC Heterostructures Using Atomic Force Microscopy Ironing.

Key words: Interlayer excitons, hétérostructures, AFM Ironing,

Abstract: Recent progress in the study of two-dimensional (2D) materials, particularly transition metal dichalcogenides (TMDCs), has unveiled remarkable properties and potential applications. TMDCs, such as MoS2 and MoSe2, are noted for their unique electronic and optical characteristics, which can be finely tuned by mechanical exfoliation and precise stacking into heterostructures. Experimental and theoretical analyses have demonstrated that these indirect gap materials, when exfoliated into their monolayer form, acquire a direct gap at the K point of the Brillouin zone. In this thesis, we discuss the development and optimization of a novel fabrication technique using nail polish, which includes the processes of exfoliation, characterization, and assembly into heterostructures of TMDCs encapsulated by hexagonal boron nitride (hBN) using a nail polish stamp. A major part of this research is dedicated to the post-fabrication technique known as atomic force microscopy (AFM) ironing. In Chapter 3, we explore the application of this method to improve the flatness and uniformity of TMDC monolayers and their heterostructures. The AFM ironing process effectively reduces surface roughness and mitigates interlayer inhomogeneity, thereby improving the optical properties of the materials. In our study, we investigate the excitonic physics in these 2D materials, employing steady-state photoluminescence (PL) spectroscopy. The results demonstrate that AFM ironing not only enhances the structural quality of the heterostructures but also significantly influences the excitonic transitions, linewidth, and intensities, leading to improved photoluminescence characteristics.
In Chapter 4, the thesis introduces the development and utilization of a flake probe for magneto-transmission measurements. This novel experimental setup, synchronized with resistive coils and cryostat systems, enables the precise study of the electronic properties of the TMDC heterostructures under varying magnetic fields. These measurements provide critical insights into the optical behavior of 2D materials by doing a proof of concept on 2D phenethylammonium lead iodide (PEPI).
Through a combination of experimental techniques, including AFM characterization and optical spectroscopy, this research provides comprehensive insights into the fundamental properties and potential applications of TMDC heterostructures. The findings contribute to the broader understanding of 2D materials and pave the way for their use in advanced nanoelectronic and optoelectronic devices.